

INVESTIGATIONS OF THE SPREADING AND CLOSURE
MECHANISMS OF PHAGOCYTOSIS IN J774A.1 MACROPHAGES

A Thesis
Presented to
The Academic Faculty

by

Daniel T. Kovari

In Partial Fulfillment
of the Requirements for the Degree
Doctor of Philosophy in the
School of Physics

Georgia Institute of Technology
May 2015

Copyright © 2015 by Daniel T. Kovari

**INVESTIGATIONS OF THE SPREADING AND CLOSURE
MECHANISMS OF PHAGOCYTOSIS IN J774A.1 MACROPHAGES**

Approved by:

Professor Jennifer E. Curtis, Advisor
School of Physics
Georgia Institute of Technology

Professor Alberto Fernandez-Nieves
School of Physics
Georgia Institute of Technology

Professor Paul M. Goldbart
School of Physics
Georgia Institute of Technology

Professor Todd Sulchek
School of Mechanical Engineering
Georgia Institute of Technology

Professor Kurt A. Wiesenfeld
School of Physics
Georgia Institute of Technology

Date Approved: 25 March 2015

ACKNOWLEDGEMENTS

I would like to thank my advisor, Dr. Jennifer Curtis. Without her support, patience, and guidance this would never have become a reality. I would also like to extend sincere gratitude to Ruth Fogg, Felis Koo, Karen Porter, and Wenbin Wei. Each of them were instrumental in developing and executing the techniques presented throughout this thesis.

I have been very fortunate to have received financial support from a number of sources. My work was supported by the National Science Foundation (NSF) in the form of both a grant awarded to my advisor to carry out our research, as well as financial support from the NSF-funded Physics of Living Systems (PoLS) research node at Georgia Tech. My work was also supported by the Georgia Tech Materials Research Science and Engineering Center (GT-MRSEC). Additionally I would like to acknowledge support from Georgia Tech's Summer Teacher Experience Program - Utilizing Physics (STEP-UP). STEP-UP enabled Karen Porter to work in the Curtis Lab over the Summer of 2014. Karen's outstanding work ultimately lead to the development of some of the experiments presented in this document.

I wholeheartedly thank my family for their unwavering support. The completion of this thesis is a testament to how fortunate I am to have had such caring people in my life. Without the persistence and dedication of my parents, Kristine Kovari and Tibor Kovari, I might never have learned to read, let alone grow to become the scientist I am today.

Finally, I would like to thank my wife, Ruth Link-Gelles. It is hard to express how grateful I am to have felt her love and support through injury, sickness, and self-doubt. Her presence in my life is a blessing for which I am truly thankful.

TABLE OF CONTENTS

| | |
|---|-------------|
| ACKNOWLEDGEMENTS | v |
| LIST OF TABLES | xiii |
| LIST OF FIGURES | xv |
| LIST OF SYMBOLS OR ABBREVIATIONS | xvii |
| SUMMARY | xix |
| I INTRODUCTION | 1 |
| II BACKGROUND | 5 |
| 2.1 A crash course in cell biology | 6 |
| 2.1.1 The cell body | 6 |
| 2.1.2 The cytoskeleton | 7 |
| 2.1.3 Plasma membrane and cortex | 7 |
| 2.1.4 Behavior of the actomyosin cytoskeleton | 8 |
| 2.1.5 Myosin molecular motors apply force to actin networks | 8 |
| 2.2 Cell migration, spreading and phagocytosis | 9 |
| 2.2.1 Cell migration is driven by actin polymerization | 10 |
| 2.2.2 Actin treadmill | 10 |
| 2.2.3 ARP2/3 mediated polymerization supports lamellipodial extension | 11 |
| 2.2.4 Myosin tension maintains cell shape during migration | 12 |
| 2.2.5 Universal cell spreading: a symmetric precursor to migration | 13 |
| 2.3 The role of actin in phagocytosis | 14 |
| 2.3.1 Contractile activity closes phagosomes | 15 |
| 2.3.2 Impact of contractile belt model | 15 |
| 2.4 Biomolecular signaling of phagocytosis and other actomyosin processes | 16 |
| 2.4.1 Phosphorylation: a prevalent signaling event cell biology | 17 |
| 2.4.2 Phagocytosis signal pathway | 17 |
| 2.4.3 Phosphatidylinositol Phosphates (PIP) | 18 |
| 2.4.4 PIP signaling in phagocytosis | 18 |
| 2.4.5 Myosin is stimulated by parallel pathways | 19 |

| | | |
|------------|--|-----------|
| 2.5 | Remarks | 20 |
| 2.5.1 | Summary of work | 21 |
| III | MATERIALS AND METHODS | 25 |
| 3.1 | Frustrated Phagocytosis | 25 |
| 3.1.1 | FP surface preparation | 25 |
| 3.1.2 | Frustrate phagocytosis assay | 27 |
| 3.2 | Cell culture | 28 |
| 3.3 | Reflection Interference Correlation Microscopy (RICM) | 28 |
| 3.4 | Image analysis | 30 |
| 3.4.1 | RICM background correction | 30 |
| 3.5 | Morphological profiling of cells | 33 |
| 3.5.1 | Level-set method for interpolating changes in cell shape | 33 |
| 3.5.2 | Activity maps | 37 |
| 3.6 | Structured Illumination Microscopy (SIM) | 37 |
| 3.7 | Traction Force Microscopy (TFM) | 40 |
| IV | CHARACTERIZATION OF FRUSTRATED PHAGOCYTOSIS | 41 |
| 4.1 | Overview | 41 |
| 4.2 | Experimental Methods | 43 |
| 4.2.1 | Frustrated phagocytosis assay | 43 |
| 4.2.2 | Opsonin density calibration | 43 |
| 4.2.3 | Statistical and Numerical Analysis | 46 |
| 4.3 | Characteristics of Frustrated Phagocytosis | 47 |
| 4.3.1 | Frustrated phagocytosis spreading behavior | 47 |
| 4.3.2 | Characterization of spreading fronts during frustrated phagocytosis . | 49 |
| 4.3.3 | Opsonion density response | 55 |
| 4.3.4 | Comparison of frustate phagocytosis with “universal” cell spreading . | 57 |
| 4.4 | Conclusion | 59 |
| V | CONTRACTION FORCE AND ACTIN CYTOSKELETAL STRUCTURE DURING FRUSTRATED PHAGOCYTOSIS | 61 |
| 5.1 | Introduction | 61 |
| 5.2 | Experimental Methods | 62 |

| | | |
|-----------|---|-----------|
| 5.2.1 | Traction Force Microscopy | 62 |
| 5.2.2 | Structured Illumination imaging of actin structure | 63 |
| 5.3 | Results | 65 |
| 5.3.1 | Cells exert contractile traction force during late stage contraction . . | 65 |
| 5.3.2 | Simultaneous fixation and permeabilization is necessary to preserve actin structure | 69 |
| 5.3.3 | Actin network undergoes structural changes during spreading, contraction and migration phases | 70 |
| 5.4 | Discussion | 83 |
| 5.4.1 | Late-stage frustrated phagocytic contraction is an active process . . . | 83 |
| 5.4.2 | F-actin architecture during P1-spreading is consistent lamellipodial extension | 83 |
| 5.4.3 | Last-stage contraction includes actin bundling | 83 |
| 5.4.4 | Mechanisms for filament reorganization | 84 |
| 5.4.5 | Dynamic contraction model of phagocytosis | 85 |
| VI | MYOSIN ACTIVITY REGULATES SPREADING SYMMETRY AND CYTOSKELETAL BUNDLING DURING LATE STAGE FRUSTRATED PHAGOCYTOSIS | 87 |
| 6.1 | Introduction | 87 |
| 6.2 | Background | 87 |
| 6.2.1 | Review of biochemical regulation of myosin | 87 |
| 6.2.2 | Myosin Inhibitors | 88 |
| 6.2.3 | Myosin activity during migration, spreading, and phagocytosis . . . | 89 |
| 6.3 | Experimental Methods | 90 |
| 6.3.1 | Myosin inhibitor dosages and effects | 90 |
| 6.3.2 | Myosin inhibition protocols | 90 |
| 6.4 | Effects of myosin inhibition on frustrate phagocytosis | 91 |
| 6.4.1 | Wortmannin resulted in little to no spreading | 91 |
| 6.4.2 | ML-7 treatment induces early cell polarization and migration but does not block late stage contraction | 93 |
| 6.4.3 | Blebbistatin treatment blocks late-stage contraction, leads to larger contact areas, and induces cell fragmentation | 94 |
| 6.5 | Cell spreading dynamics under myosin inhibition | 97 |

| | | |
|---|--|-----|
| 6.5.1 | Protrusion speed under myosin inhibition | 97 |
| 6.6 | Conclusion | 101 |
| VII HYDRODYNAMIC MODEL OF CELL SPREADING | 103 | |
| 7.1 | Overview | 103 |
| 7.2 | Motivation | 103 |
| 7.3 | Cell spreading as a hydrodynamic wetting process | 104 |
| 7.3.1 | Physics of wetting | 105 |
| 7.3.2 | Incorporation of cellular mechanical properties | 108 |
| 7.4 | Estimating mechanical parameters | 109 |
| 7.4.1 | Initial cell surface area | 110 |
| 7.4.2 | Membrane cortical tension | 110 |
| 7.4.3 | Cell body behaves as a viscous fluid | 110 |
| 7.4.4 | Estimate protrusion force using migration stall force | 112 |
| 7.4.5 | Adhesion energy small compared to work done by protrusion force . . | 112 |
| 7.5 | Characteristics of the model | 113 |
| 7.5.1 | Model exhibits tanh-like spreading, similar to experiments | 113 |
| 7.5.2 | Model captures range of observed behavior | 113 |
| 7.5.3 | Non-spreading cells suggest approximate value of adhesion energy . . | 115 |
| 7.6 | Discussion | 116 |
| 7.6.1 | Model predicts relationship between cell spreading and mechanical parameters | 116 |
| 7.6.2 | Proposed experimental validation of model predictions | 116 |
| 7.6.3 | Limitations and possible modifications | 118 |
| VIII CONCLUSION | 119 | |
| 8.1 | Summary of results | 119 |
| 8.2 | Future work | 121 |
| APPENDIX A — TRACTION FORCE MICROSCOPY TECHNIQUES AND ANALYSIS | 125 | |
| APPENDIX B — MEMBRANE TETHER FORCE | 135 | |
| APPENDIX C — TABLE OF SIGNALLING PROTEINS | 137 | |

| | |
|------------|-----|
| REFERENCES | 141 |
| VITA | 153 |

LIST OF TABLES

| | | |
|-----|---|-----|
| 4.1 | UV-Vis absorption parameters | 46 |
| 4.2 | Calibrated opsonin density | 55 |
| 6.1 | Myosin inhibitors and dosages | 91 |
| 7.1 | Hydrodynamic model parameters. | 113 |
| A.1 | Acrylamide gel recipe. | 128 |

LIST OF FIGURES

| | | |
|-----|--|----|
| 2.1 | Schematic of phagocytosis | 6 |
| 2.2 | <i>In vitro</i> F-actin network contraction in the presence of myosin II | 9 |
| 2.3 | The actin treadmill | 11 |
| 2.4 | Migrating fish keratocyte cyo-em and fluorescence images | 12 |
| 2.5 | Phagocytic “contractile actin belt” | 16 |
| 2.6 | Phosphatidylinositol 3,4,5-triphosphate | 18 |
| 2.7 | Cartoon schematic of myosin II | 19 |
| 2.8 | Phagocytosis Signal Cascade | 23 |
| 3.1 | Frustrated Phagocytosis | 26 |
| 3.2 | Cell imaged using RICM | 29 |
| 3.3 | Schematic of RICM | 31 |
| 3.4 | Background subtraction | 32 |
| 3.5 | Edge marker propagation | 34 |
| 3.6 | Protrusion/retraction activity map during frustrated phagocytosis | 36 |
| 3.7 | Structured Illumination Microscopy calculation | 39 |
| 3.8 | Traction Force Microscopy schematic | 40 |
| 4.1 | Opsonin density calibration | 45 |
| 4.2 | J774A.1 spreading on opsonized surfaces | 48 |
| 4.3 | Protrusion growth rate. | 50 |
| 4.4 | Protrusion growth rate statistics | 52 |
| 4.5 | Activity map of contracting cell | 53 |
| 4.6 | Activity map of non-contracting cell | 54 |
| 4.7 | Response to opsonin density | 56 |
| 5.1 | Strain energy during frustrated phagocytosis | 67 |
| 5.2 | Traction force microscopy with traction force moments | 68 |
| 5.3 | Phalloidin staining protocol comparison | 69 |
| 5.4 | Macrophage undergoing frustrated phagocytosis | 73 |
| 5.5 | F-actin structure during P1 frustrated phagocytosis | 75 |
| 5.6 | F-actin structure during P1-P2 transition | 77 |

| | | |
|------|---|-----|
| 5.7 | F-actin structure during contraction phase | 79 |
| 5.8 | F-actin structure during macrophage migration | 81 |
| 5.9 | Dynamic contraction model | 84 |
| 5.10 | Dynamic contraction model for phagocytosis | 86 |
| 6.1 | Wortmannin treated macrophages | 92 |
| 6.2 | Spreading Area under myosin inhibition | 95 |
| 6.3 | Behavior changes after myosin inhibition | 96 |
| 6.4 | Migrating blebbistatin inhibited cell with activity map | 99 |
| 6.5 | Blebbistatin induce cell fragmentation with activity map | 100 |
| 7.1 | Dynamic Sessile drop and Poiseuille flow | 105 |
| 7.2 | Aspirated red blood cell. | 108 |
| 7.3 | Viscoelastic behavior of macrophages | 111 |
| 7.4 | Hydrodynamic model with average parameters | 114 |
| 7.5 | Hydrodynamic model fit to data | 115 |
| 7.6 | Hydrodynamic model results for passive spreading | 116 |
| 7.7 | Variation of hydrodynamic model parameters | 117 |
| 8.1 | Dynamic contraction model of phagocytosis | 122 |
| A.1 | Polyacrylamide stiffness versus acrylamide : bis-acrylamide ratio | 127 |
| A.2 | TFM substrate preparation | 130 |
| A.3 | TFM Sample Holder | 131 |
| A.4 | TFM Sample Holder Schematic | 134 |
| B.1 | Membrane tether schematic | 135 |

LIST OF SYMBOLS OR ABBREVIATIONS

| | |
|----------------|--|
| APTES | (3-Aminopropyl)triethoxysilane. |
| BSA | Bovine Serum Albumin. |
| DAPI | 4',6-diamidino-2-phenylindole. |
| DCM | Dynamic Contraction Model. |
| DMEM | Dulbecco's Modified Eagle Medium. |
| DMSO | Dimethyl sulfoxide. |
| EGTA | Ethylene glycol-bis(2-aminoethylether)-N,N,N',N'-tetraacetic acid. |
| F-actin | Filamentous actin. |
| FP | Frustrated Phagocytosis. |
| FTTC | Fourier Transform Traction Cytometry. |
| G-actin | Globular actin. |
| HBSS | Hank's Balanced Salts Solution. |
| HEPES | 4-(2-hydroxyethyl)-1-piperazineethanesulfonic acid. |
| MaPTES | 3-(Trimethoxysilyl)propyl methacrylate. |
| PEM | Cytoskeletal stabilization buffer containing: PIPES, EGTA, and MgCl ₂ . |
| PIPES | 1,4-Piperazinediethanesulfonic acid. |
| PIV | Particle Image Velocimetry. |
| PTV | Particle Tracking Velocimetry. |
| SIM | Structured Illumination Microscopy. |
| TFM | Traction Force Microscopy. |

SUMMARY

Phagocytosis is the process by which cells engulf foreign bodies. It is the hallmark behavior of white blood cells, being the process through which those cells ingest and degrade pathogens and debris. To date a large amount of research has focused on documenting the existence and role of biochemical components involved with phagocytosis. Scores of signaling molecules have been implicated in the complex signal cascade which drives the process. These molecules are small (typically no larger than 5 nanometers) and operate in a crowded, chemically “noisy,” environment, yet they coordinate the cell’s activity over comparatively expansive distances (as large as 20 micrometers). How these molecular processes scale-up to coordinate the activities of the cell over such massive distances is largely unknown.

Using a planar analog of phagocytosis termed “frustrated phagocytosis,” we experimentally demonstrate that phagocytosis occurs in three distinct phases: initial cell-antigen binding, symmetric spreading, and late-stage contraction. Initial binding and symmetric spreading appears to be both mechanically and chemically similar to the quasi-universal cellular behaviors of adhesion and migration. Adhesion and migration have received extensive attention from the biophysics community in recent years. Leveraging these similarities, we adapt the biomechanical frameworks used in models of migration to phagocytosis.

We show that macroscopic properties such as a cell’s effective viscosity and membrane cortical tension can be used to model cell behavior during phagocytosis. Our experiments reveal that late-stage contraction distinguishes frustrated phagocytosis from other spreading behaviors. This contraction is myosin dependent. Additionally we demonstrate, for the first time, that late-stage contraction corresponds with formation of a contractile F-actin belt. Based on the dynamic contraction model (DC) developed to explain actin structure during cell migration we propose a DC model of phagocytosis which posits that contractile belt formation is the result of a late-stage myosin activity coupled with F-actin.

CHAPTER I

INTRODUCTION

Phagocytosis is the process by which individual cells engulf foreign bodies. It is the hallmark behavior of macrophages and neutrophils (white blood cells); phagocytosis is the process through which those cell types ingest and degrade pathogens and debris throughout the body. Phagocytosis has evolved to be an essential process for maintaining the health of an animal. It is integral to wound repair, inflammation responses, and infection control. Understanding the complexities of phagocytosis not only holds the promise of answering basic scientific questions about how and why the process works, but could also provide insight into how pathogens like *Listeria monocytogenes* and *Yersinia pestis* co-opt this process and ways in which bio-technologies like implants and drug delivery mechanisms can be improved to either suppress or enhance immune responses [47, 46, 64]. Furthermore, many of the biochemical machines which drive phagocytes are present and play similar roles in numerous other cell types [91, 16]. Consequently, studying phagocytosis is not only essential to complete our understanding of the mechanisms of disease but also provides insight into related processes like cell migration, wound healing, and tissue growth.

To date a large amount of research has focused on documenting the existence and role of biochemical components involved with phagocytosis. Scores of signaling molecules have been implicated in the complex signal cascade which drives the process. These molecules are small (typically no larger than 5 nm), yet they coordinate the cell's activity over comparatively expansive distances [131]. Phagocytosis enables cells to internalize extremely large particles ranging from 200 nm for a typical virus up to a few micrometers for bacteria and extracellular debris. How these molecular processes scale-up to coordinate the activities of the cell over such massive distances is unknown.

In recent years, inroads have been made in the development of a framework explaining how biomolecular components coupled to the mechanical properties of the cell coordinate cell

adhesion, spreading, and migration, processes thought to be closely related to phagocytosis [16]. Experiments have thoroughly documented that these processes are driven by structural changes in the architecture of the actin cytoskeleton, forces generated by myosin motor proteins, and tension established by the cell membrane [90, 40, 66]. In this work we assess the degree to which the frameworks developed to explain migration and spreading compare to phagocytosis, as measured by various experiments. We develop a series of assays which interrogate the dynamics of phagocytosis in a planar geometry termed “frustrated phagocytosis”. These assays capture many of the characteristics of traditional (particle) phagocytosis yet afford the direct comparison with predictions and experiments made in the contexts of cell spreading and migration.

Phagocytic particle engulfment occurs in three phases: initial contact, spreading, and internalization. The experiments discussed here allow for detailed analysis of cell behavior during each of these phases. This reveals that the first two phases are functionally similar to “universal” spreading behaviors observed in various cells as they adhere to biologically relevant substrates. Second phase spreading is dominated by the expansion of the actin cytoskeleton in a thin but dense sheet called the lamellipodium. The third phase is notably distinct for that of other cell types. It is characterized by a hallmark cellular contraction not observed in other cellular systems. Immunobiologists have long theorized that this contraction enables phagocytes to form sealed compartments around target particles, finalizing internalization [134].

Our frustrated phagocytosis assays facilitate the use of advanced microscopy techniques incompatible with traditional phagocytosis assays. Traction Force Microscopy (TFM) reveals that late-stage contraction produces forces consistent with those measured in migrating cells. Using super-resolution Structured Illumination Microscopy (SIM) we show that contraction is associated with cytoskeletal structural motifs observed in migrating cells. This suggests that although late-stage contraction distinguishes phagocytosis from other spreading behaviors it is nonetheless reliant on mechanical paradigms universal to many cell types. Furthermore, we show that late-stage contraction is dependent on myosin motor activity.

At high levels of myosin inhibition, contraction is suppressed and spreading proceeds unchecked until the cell pulls itself into fragments. Partial inhibition of these molecular motors enables phagocytes to polarize and undergo directed migration morphologically similar to highly-motile fibroblast and epithelial cells which have served as the prototypical cell types for the majority of physics based motility models. We posit that myosin motor activity regulates tension within the cytoskeleton and the degree of this activity, in part, dictates cell phenotype. In other words, cells operate within a continuum of cytoskeletal tension under which biochemical signals unique to phagocytosis tune the mechanics of the system to facilitate late-stage contraction.

CHAPTER II

BACKGROUND

Phagocytosis is a complex process orchestrated by a myriad of biological signals. In the context of the immune system there are a number of chemical cues which trigger white blood cells to attempt to phagocytose a particle. Although these early signaling events may differ, late stage activities converge into a single generic behavior. Among the various phagocytic pathways the best studied is the Fc-Receptor mediated pathway. It is the pathway by which the adaptive immune system labels pathogenic particles and signals “professional phagocytes” (macrophages and neutrophils) to degrade those particles.

The process begins with target particles being coated with antigen specific immunoglobulin G (IgG) proteins (a process called opsonization). IgG are large Y-shaped globular proteins secreted by B-cells into the blood. The upper branch of the Y is composed of proteins (termed “fragments A and B” or Fab) which specifically bind to its target antigen. The lower branch, termed “fragment C” (Fc), is universal to all IgGs and binds to Fc- γ receptors (Fc- γ R’s) on the surface of phagocytes, stimulating phagocytosis.

Phagocytosis is often characterized in four stages: initial binding, particle engulfment, internalization, and degradation. In the first stage, Fc-Receptors, diffusing along plasma membrane, bind to the opsonized particle. Second, after a threshold of bound receptors is achieved the cell forms membrane protrusions around the surface of the particle, a structure termed the phagocytic cup. Third, once the particle has been sufficiently engulfed, the cell attempts to internalize the particle by sealing the newly formed phagocytic cup into an intracellular vesicle called a phagosome. Finally, after successful internalization the phagosome is shuttled toward the center of the cell where degradation of the particle occurs.

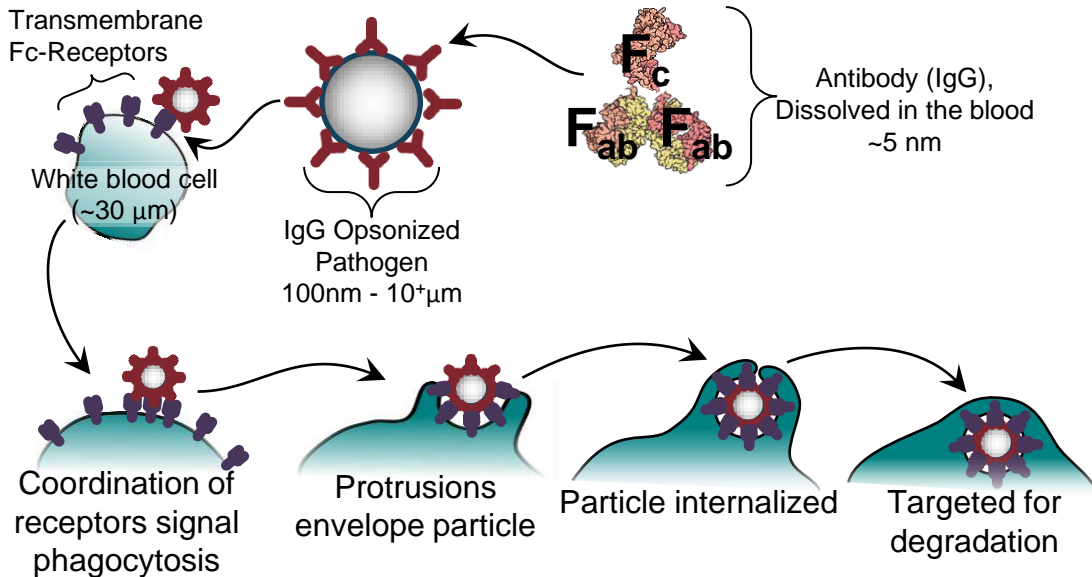


Figure 2.1: Schematic of phagocytosis. IgG antibodies opsonize pathogens. Fc-Receptors bind with Fc-fragment of pathogen-bound IgG. Coordination of multiple binding events triggers cellular protrusions, followed by internalization and finally phagosome is targeted for degradation.

2.1 A crash course in cell biology

For the uninitiated, one of the steepest hurdles in studying cell biology is familiarizing oneself with extensive vocabulary used to discuss biological concepts. To facilitate our discussion of phagocytosis it is helpful to begin with a brief review of basic cellular anatomy before proceeding with our detailed discussion of what is known about phagocytosis, how it works, and the ways it parallels other cell behaviors. Readers with a basic understanding of cell biology should feel free to move along to Section 2.2 where our substantive discussion begins.

2.1.1 The cell body

The cell body is a diverse mixture of organelles, macro-molecular structure (large proteins, glycoproteins, and nucleic acids), small bio-functional molecules, salts, and of course, water. The fluid phase of the cell body (water, salts, and dissolved proteins) is termed the cytosol or cytoplasm. Interspersed throughout the cytosol are various organelles which perform a multitude of metabolic tasks. The single largest organelle is the cell nucleus, a large spherical vesicle which houses the chromosome and is the site of transcription. For the macrophages discussed throughout this thesis the nucleus is 10-15 μm in diameter, centrally located, and

accounts for the bulk of cell volume. Mechanically, the nucleus is important because it is stiffer than much of the surrounding cell body and therefore affects the cell's physical activities.

2.1.2 The cytoskeleton

Throughout the cell body, networks of polymeric protein filaments impart rigidity and enable cell movement. Microtubules are the largest filaments, roughly 24 nm in diameter, and can span the length of the cell. They are by far the most rigid filamentous structure in the cell, with persistence lengths of 5.2 mm [60]. In addition to providing rigidity, microtubules act as a highway network along which motor proteins (dynein and kinesin) can shuttle cellular cargo. Intermediate filaments (vimentin), which are significantly more elastic than microtubules, provide an additional level of structural support. Finally, actin, which forms a helical filament (F-actin) approximately 10 nm in diameter and has a persistence length of 17.7 μm , forms a highly dynamic structure which is responsible for generating forces necessary for changes in cell shape [60]. Actin monomers (G-actin) asymmetrically assemble into F-actin with a specific orientation. The two ends of an F-actin filament are distinguished as the “barbed end” and “pointed end.” Activity of the actin cytoskeleton and its associated protein machinery is paramount to phagocytosis.

2.1.3 Plasma membrane and cortex

The boundary of the cell is formed by a phospholipid bilayer which not only acts as a mechanical barrier, separating the cell from its surroundings, but is also home to a plethora of bio-functional machinery including intra and extra cellular chemical receptors, ion channels, and membrane-bound signaling molecules. Just beneath the plasma membrane lies an actin-rich layer called the cortex. This cage-like mesh both contributes to the mechanical stability of the cell and plays a role in the regulation of large scale membrane deformations (necessary for phagocytosis).

2.1.4 Behavior of the actomyosin cytoskeleton

Actin networks display a very rich set of behaviors. In muscle cells, for instance, actin filaments bundle into parallel stalks which run the length of the cell. Bundles of counteracting myosin motors pull on parallel actin stalks, creating tension which causes the muscle cell to contract. In non-muscle cells, especially phagocytes, actin networks are less organized. Actin, combined with myosin motor proteins (a system termed the actomyosin cytoskeleton), drives a myriad of cell behaviors. Depending on the signaling environment within the cell, actin can drive highly localized, cylindrical, membrane protrusions (filopodia), broad, flat protrusions (called lamellipodia), or bundle into rigid stalks (stress fibers) which provide cellular rigidity. Cellular protrusions are generated at the cell periphery via the extension of actin filaments (F-actin) through the polymerization of globular actin monomers (G-actin). In the context of phagocytosis, actin polymerization is responsible for driving phagocytic cup formation around target particles; actin has also been implicated in the closure of phagocytic cups and internalization of phagosomes [90].

2.1.5 Myosin molecular motors apply force to actin networks

While polymerization and depolymerization enable actin networks to generate protrusive forces, cells generate tension within actin networks through the activity of myosin motor proteins. Across all kingdoms of life there have been 18 identified classes of myosin motors, 11 of which have been documented in humans [122]. Among these classes, class II myosins are the most omnipresent, being the motor primarily responsible for reshaping actin networks.

Myosin II is a two-headed motor protein capable of “walking” along F-actin. It possesses a long tail region which interacts with other myosin II tails, resulting in the formation of myosin filaments which are capable of binding adjacent F-actin strands and translocating those strands relative to each other. It is important to note that myosin II motion is directed toward the barbed end of F-actin. Consequently a myosin filament straddling two F-actin strands oriented in the same direction will move towards their barbed end, while myosin attached to anti-parallel F-actin strands will create tension between those strands.

In muscle cells, myosin II bundles into thick stalks between the cells’ z-disks. Upon

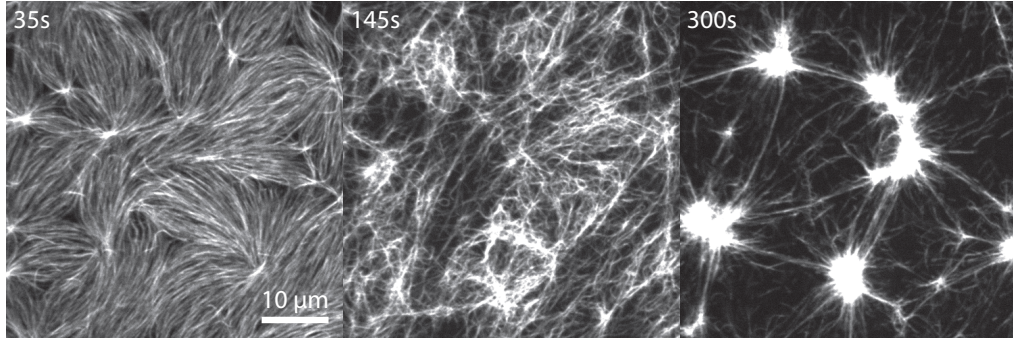


Figure 2.2: *In vitro* F-actin network contraction in the presence of myosin II. F-actin polymerized in the presence of phalloidin and confined to a single plane. At time t=0s myosin II is added to the network. Myosin activity causes the reconstituted actin network to contract into bundles linking highly concentrated points. Images originally published by Murrell and Gardel [96]. Reprinted here under the Creative Commons Attributed-Noncommercial license (CC-BY-NC-SA 3.0).

activation these bundles exert strong forces on anti-aligned actin fibers which also span the cell, ultimately leading to the characteristic whole-cell contraction. Non-muscle myosin II (NMII) motors are ubiquitous throughout all other (non-muscle) cell types. Like muscle myosin, NMII possess long tails which cause motor aggregation; however, NMII motors do not form cell-length contractile units. Instead, NMII form filaments approximately 300 nm long with counter-acting motor head groups, which exert tension on local F-actin fibers[14]. *In vitro* characterizations of mixtures of F-actin and myosin reveal that myosin activation results in overall contraction of the actin network and bundling of distinct actin filaments into dense regions (Figure 2.2) [96].

2.2 Cell migration, spreading and phagocytosis

Although the biochemical cascade responsible for Fc γ R-mediated phagocytosis is increasingly well-understood, very few studies have investigated the connection between those chemical signals and the actin structures ultimately responsible for executing cell behavior. One reason for this shortfall is that imaging phagocytosis is technically challenging. Phagocytosis is an inherently 3-dimensional process. While 3-D microscopy methods exist, the small scale of the structures involved in phagocytosis and optical resolution limits of traditional optical techniques make it difficult, if not impossible, to quantitatively assess the behavior of actomyosin during phagocytosis. For this reason we look to similar, but easier to study,

cell behaviors to provide plausible explanations regarding the physics of phagocytic cup formation and phagosome internalization.

Throughout this thesis we compare and contrast phagocytic behavior with amoeboidal cell migration and “universal” cell spreading. In recent years, a great deal of work has been done to investigate the mechanism responsible for both of these behaviors. This work has revealed actomyosin structural motifs which cells use, universally, to execute physical activities [130, 118].

2.2.1 Cell migration is driven by actin polymerization

Among the two behaviors mentioned above, cell migration has been studied more extensively by the biophysics/cell mechanics community. Broadly speaking, this behavior consists of three major activities. First, the cell generates a broad protrusion at its leading edge called the lamellipodium. Next, it forms protein anchors (focal adhesions) between that protrusion and the underlying substrate. Finally, anchors at the rear of the cell are degraded and molecular motors generate tension within the cell causing it to pull off of the weakened anchors and shift forward. It is well documented that the predominant driver of protrusion formation is the polymerization of actin at the leading edge of the cell [84]. Live-cell fluorescent microscopy experiments have unequivocally shown that actin monomers (G-actin) preferentially polymerize at the leading edge of a migrating cell and are steadily shuttled back towards the cell body where they depolymerize, resulting in an approximately constant length zone of polymerized actin which supports the traveling lamellipodium [105, 71, 37]. This coordination of polymerization and depolymerization is termed the “actin-treadmill.”

2.2.2 Actin treadmill

In the absence of other factors, actin polymerizes into polarized linear helical filaments, having distinct ends termed the barbed and pointed ends. *In vitro* polymerization and depolymerization rates have been shown to depend on the relative concentrations of ATP-bound and ADP-bound G-actin. ATP-bound actin primarily binds to the barbed end, while ADP-actin binds to the pointed end. Depending on the respective monomer availability, actin will grow or shrink at the either barbed or pointed ends; at a critical concentration,

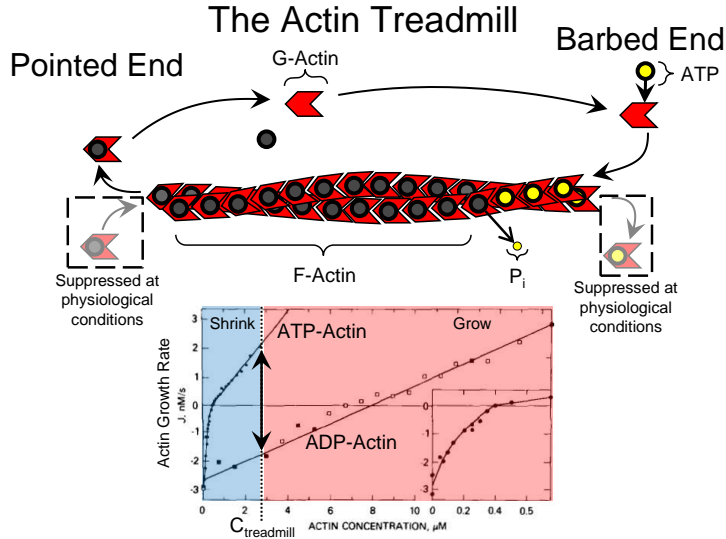


Figure 2.3: The actin treadmill. At physiological conditions ATP-actin polymerizes at the barbed end of F-actin filaments while ADP-actin depolymerizes at the pointed end. At critical concentration of ADP/ATP-actin filament lengths remain constant yet there is continual exchange of actin monomers within the filament, establishing a characteristic treadmill flow. Carlier *et al.* initially demonstrated the actin treadmill *in vitro*. The results of their experiment are shown in the plot. Blue region indicates monomer concentrations which result in filament shrinkage while concentrations above $C_{treadmill}$ correspond to filament growth [28]. Reproduced here under the Creative Commons Non-commercial license (CC BY).

filament length remains constant, with an equal rate of growth at the barbed end and depolymerization at the pointed end [77] (see Figure 2.3). Within the cell, polymerization and depolymerization rates of linear actin filaments (F-actin) are regulated by two additional factors. ADF/cofilin interpenetrates the F-actin helix resulting in an increased rate of depolymerization [9]. Capping proteins (Gelsolins, CapZ and CapG) bind F-actin at the barbed end, preventing polymerization [84].

2.2.3 ARP2/3 mediated polymerization supports lamellipodial extension

Within lamellipodia a third protein complex (ARP2/3) mediates actin growth through the creation of nucleation points. ARP2/3 binds to the sides of existing actin filaments, creating sites from which daughter filaments can assemble [147]. ARP2/3 is incorporated into the actin network primarily at the front of the lamellipodium. This results in the formation of dense, highly-branched, interwoven networks which tend to expand from a central region.

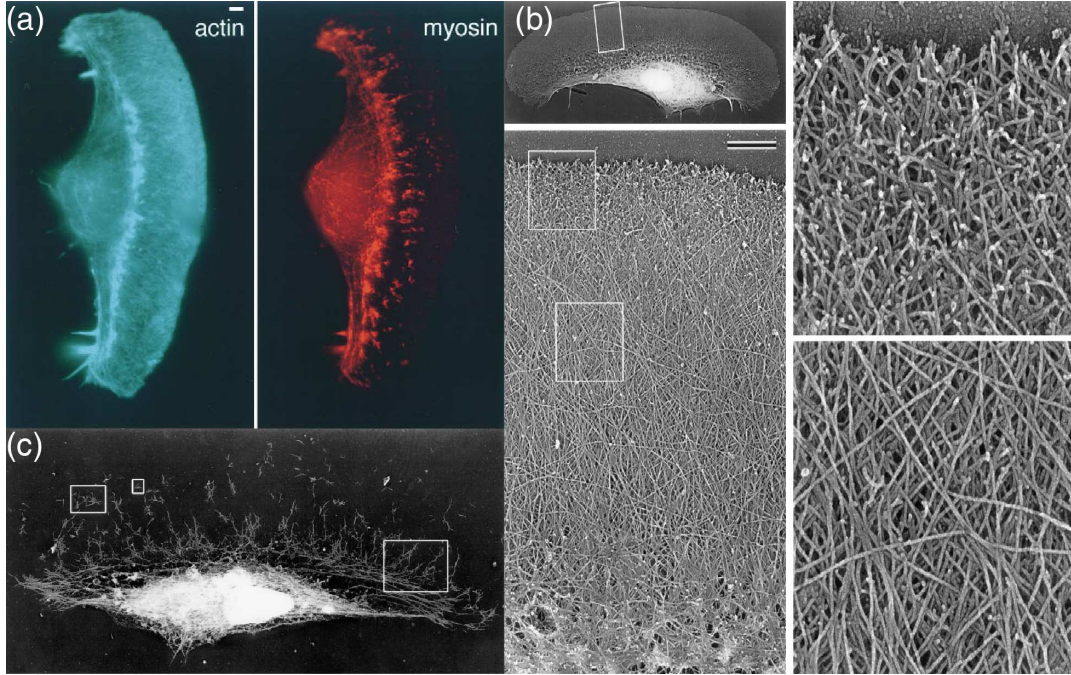


Figure 2.4: Migrating fish keratocyte. (a) Fluorescently stained actin and myosin illuminated by TRITC-phalloidin (cyan) and direct anti-myosin immunofluorescence (red). Scale bar indicates 2 μm (b) EM of detergent-extracted cells. Actin in lamellipodium forms a brush-like zone at the leading edge (top). Filament branching is induced by APR2/3. Actin condenses in transition region (bottom), forming band parallel to edge. Scale bar indicates 1 μm . (c) EM of detergent-extracted and gelsolin-treated cells with myosin immuno-gold labeling. Myosin forms a boundary bundle at rear of lamellipodium and is highly concentrated at rear of cell. All images were originally published in Svitkina *et al.* [130] and are reprinted here under the Creative Commons Attributed-Noncommercial license (CC BY-NC-SA 3.0).

The organization of the actin network is depicted in cryo-electron micrographs produced by Svitkina *et al.* (Figure 2.4) [130]. Branched lamellipodial actin drives the cell perimeter outward via the actin treadmill. F-actin filaments grow preferentially toward the cell edge where the increased network density caused by filament branching resists the inward directed membrane tension which would otherwise cause individual filaments to collapse.

2.2.4 Myosin tension maintains cell shape during migration

In migrating cells, fluorescent and cryo-em imaging reveals that myosin activity is located predominately at the rear. This concentrated myosin activity results in a dense clustering of actin at the very back of the cell and a long stalk of actin and myosin behind the lamellipodium, parallel to the advancing edge (see Figure 2.4) [130]. Studies involving inhibition

of myosin have shown that, although myosin is not strictly necessary for the formation of lamellipodial protrusions, it helps maintain cell shape during periods of rapid growth. Moderate levels of myosin inhibition result in the formation of multiple lamellipodia around the cell perimeter and more frequent changes in migration direction [137]. High levels of myosin inhibition lead to separation of propagating lamellipodia from the cell body, resulting in cell fragmentation [118]. These results suggest that tension within the actomyosin cytoskeleton is essential for maintaining network coherence.

2.2.5 Universal cell spreading: a symmetric precursor to migration

Like cell migration, the process by which cells adhere and spread along substrates also relies heavily on the activity of actin and myosin. When placed in contact with an appropriate substrate many somatic cell types undergo smooth, processive, spreading along that substrate. Starting from the detached state, this spreading is often characterized as occurring within three “universal” behavioral phases. At the onset, immediately following initial surface attachment, spreading is slow. During this period changes in cell shape are thought to be the result of passive deformation of the cell membrane and cortex due to receptor-ligand binding at the cell-substrate interface. As spreading continues, active processes begin to dominate cell behavior. During this second phase, ARP2/3 mediated actin growth drives rapid expansion of the cell-substrate contact area. This behavior is often characterized as a symmetric lamellipodium. In the final stages of spreading, cells reach a characteristic maximum contact area, at which point they typically transition to a migratory behavior.

Three-phase “universal” spreading behavior has been observed in a number of cell types and a variety of biological contexts. For example, spreading behaviors can be seen in T-cells (which spread along the surface of antigen presenting cells during the course of infection response), platelets (which spread along tissue surface to create a barrier to stop bleeding), epithelial cells (which makeup those tissue surfaces), and fibroblasts (which spread over tissue surfaces as they engage in wound repair) [82, 10, 145].

The most detailed and comprehensive studies of cell spreading have been conducted by Sheetz and co-workers. Their experiments have demonstrated clear distinctions between the

phases of spreading [42, 45, 44], identified membrane tension as a probable mediator of cell behavior [55, 110, 56], and demonstrated that myosin activity play a central role in maintaining cell shape regulating spreading behavior [58, 27, 43, 26]. Even more than migration, cell spreading bears a strong resemblance to phagocytic cup formation. Like phagocytosis, cell spreading is initiated by ligand-receptor interactions (IgG-FcR in the case of phagocytosis). In fact, as will be discussed extensively throughout this thesis, when phagocytes engage with excessively large targets (termed frustrated phagocytosis) phagocytic cup formation closely resembles “universal” cell spreading. It should be noted, however, that under such experiments there are subtle differences that distinguish phagocytosis from cell spreading. For instance, while “universal” cell spreading is thought to terminate in a transition from symmetric spreading to polarized migration without substantive changes in cell-substrate contact area, phagocytes undergoing frustrated phagocytosis exhibit a pronounced (and often symmetric) contraction.

2.3 The role of actin in phagocytosis

The involvement of the actin machinery in driving phagocytosis is well established [91]. Experiments as early as 1977 demonstrated that degrading F-actin via the drug cytochalasin inhibited phagosome formation [61]. Since those early studies, a wealth of knowledge has accumulated concerning the biomolecular machinery connecting the activation of Fc γ -receptors to the eventual stimulation of F-actin-mediated shape-change. As in the lamellipodia of migrating and spreading cells, phagosomal protrusions are driven by expansion of ARP2/3-branched F-actin filaments [90].

Although the mechanisms responsible for actin polymerization during phagocytosis are thought to work analogously to their counterparts in cell migration, the precise organization of the actin network has yet to be experimentally verified. To date, few studies have characterized phagocytosis to the extent which migration and spreading have been documented. While the biomachinery responsible for phagosomal formation is built from the same components responsible for migration and spreading, subtle differences between these cell types may predicate gross changes in cell behavior, such as the contraction observed

during frustrated phagocytosis.

2.3.1 Contractile activity closes phagosomes

One of the most distinctive features of phagocytosis is the cell's ability to form a sealed compartment around an object over which it has spread. During late stage phagocytosis, distal margins of the forming phagosomes exert a contractile force on target particles. Fluorescent imaging reveals a dense accumulation of actin at the point of constriction. Additionally, inhibition of myosin prevents distal contraction and final particle internalization [134]. These findings have led to the proposal of a "contractile actin belt" [131]. Under this theory, actin bundles into an azimuthal band which surrounds the target particle. Engagement of myosin motors generates contractile tension which pinches the phagosome shut and drives the particle into the body of the cell. A schematic of this process is illustrated in Figure 2.5b. Figure 2.5a shows the effect contractile force has on soft target particles. The micrograph also shows that actin is highly concentrated in the contractile region.

It is important to note that although fluorescent images like that shown in Figure 2.5a clearly demonstrate that actin is highly concentrated at the contractile margin, resolution limits of traditional fluorescence techniques prevent us from conclusively knowing whether actin is bundled into azimuthal fibers or instead oriented along the direction of edge propagation as would be consistent with ARP2/3 mediated polymerization observed in migrating cells (sketched in Figure 2.5c).

2.3.2 Impact of contractile belt model

The concept of a contractile actin belt predicates a number of significant questions. First, are phagocytic protrusions architecturally similar to lamellipodia? In other words, is actin organized in an outward directed, ARP2/3 branched, network? If so, how does the network switch from having F-actin primarily directed along the contour of protrusion to the azimuthal geometry prescribed by the contractile belt? Alternatively, if F-actin architecture is fundamentally different from lamellipodial architecture, how does the cell generate forces necessary to push the phagocytic cup around the particle?

It is possible the answer to these questions maybe can be gleamed from actomyosin

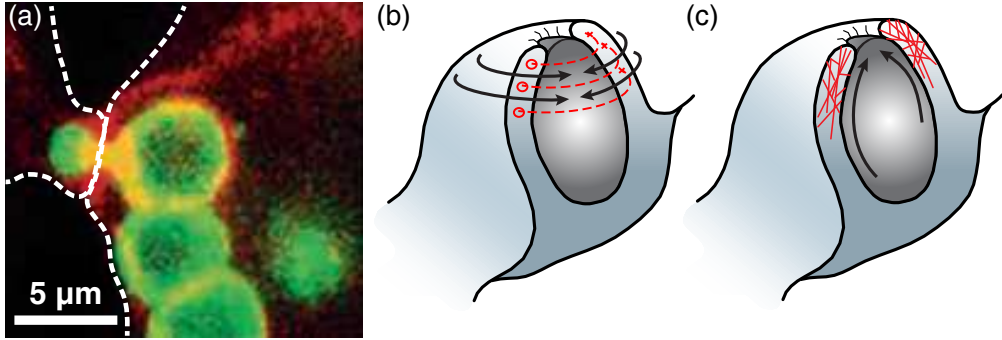


Figure 2.5: Phagocytic “contractile actin belt”. (a)RAW264.7 macrophages phagocytosing a shared, deformable, particle (green). Actin (red) is highly concentrated at contracting distal margins. White lines illustrate cell edges. Both cells exert a contractile activity at their respective distal margins. Contractile force causes particle to deform. (b)Schematic of contractile belt. In proposed “contractile belt” theory, actin bundles into bands around the edge of the phagosome (red dashes). As myosin motors engage with F-actin, the induced tension causes the actin ring to contract like a noose. This activity seals the phagosome and drives the particle into the cell. (c) Schematic of branched actin network oriented along phagosome. Based on cyro-em images of migrating cells, APR2/3 branched F-actin networks align with barbed ends pointing toward advancing edges. Micrograph originally published by Swanson *et al.* Reprinted here with permission. Original artwork (b,c) adapted from Swanson *et al.* [134]

structures present in migrating cells. In Chapter 5 we present evidence which suggests that the actin contractile belt does in fact exists and that it is related to the dense parallel banding of actin and myosin often observed at the base of migrating cells (see Figure 2.4a,c). In Chapter 6 we show that phagocytic contraction is dependent on myosin motor activity and present evidence which suggests that transitions from symmetric spreading to polarized migration depend on the relative activity of myosin within a cell. In combination, these studies demonstrated that phagocytosis is reliant on many of the same biophysical mechanism inherent to spreading and migration and that the physics-based frameworks used to discuss those systems is relevant to our understanding phagocytosis.

2.4 Biomolecular signaling of phagocytosis and other actomyosin processes

The discussions presented in chapters 4, 5 and 6 rely heavily upon what is known concerning phagocytic signal cascade. In the subsequent sections I present an overview of this chemical

cascade. Although this process is complex, and at times easier to conceptualize as a “black-box,” it is important to keep in mind where and how intermediate biochemical signals communicate cellular activity. In Chapter 6 we rely heavily upon the details of the signal cascade as the experiments presented in that chapter attempt to isolate various phagocytosis related behaviors through the inhibition of specific biochemical signals. To assist the reader, a table listing biochemical names, abbreviations, and functions is included in the appendix. Additionally, a diagram of the phagocytosis signal cascade is included at the end of this chapter (Figure 2.8).

2.4.1 Phosphorylation: a prevalent signaling event cell biology

A common signaling motif in molecular biology is the addition/removal of phosphate groups to/from proteins and other organic molecules. The addition of a phosphate group to a substrate is termed phosphorylation, while the removal is termed dephosphorylation. In various biological processes, enzymes are either activated or deactivated by phosphorylation. Phosphorylation of a particular substrate or protein is typically initiated by a second regulatory enzyme. In the context of phagocytosis, phosphorylation is one of the primary mechanisms by which signaling components are regulated.

2.4.2 Phagocytosis signal pathway

Prior to activation, Fc-receptors are believed to be free to diffuse along the cell’s plasma membrane [70]. Upon binding with a conglomeration of Fc-fragments affixed to a particle’s surface the receptors become localized. Localization of an Fc-receptor appears to increase the likelihood that its cytoplasmic signaling region (ITAM) becomes phosphorylated. Evidence suggests that the enzyme Src kinase is responsible for phosphorylating localized Fc-receptors [62]. The addition of phosphate groups to localized receptors kicks-off a cascade of subsequent signals.

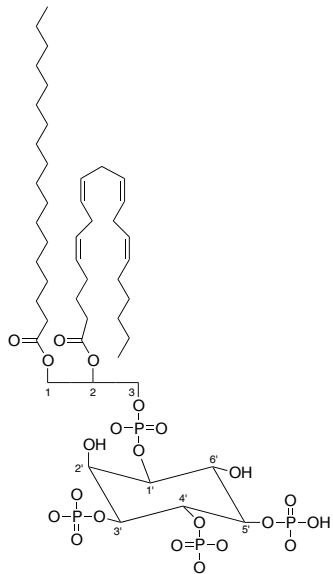


Figure 2.6: PI molecules are identified by which carbon has an additional phosphate group. The molecule pictured above has 3 additional phosphates, bound to carbon 3,4,5.

2.4.3 Phosphatidylinositol Phosphates (PIP)

As this sequence proceeds, lipid signaling molecules, phosphatidylinositol (PI), become phosphorylated. Phosphatidylinositol molecules are extremely important to all actomyosin-related processes, including phagocytosis, spreading, and migration. The inositol head group of phosphatidylinositol can be phosphorylated in up to three locations (yielding a total of 8 permutations). Variations of PI are identified by the location they are phosphorylated and the number of phosphate groups they possess. For example, phosphatidylinositol 3-phosphate, PI(3)P denotes the form where the 3' carbon of the inositol head group has been bound to a phosphate group.

Because they are lipids, PIP molecules are localized to the cell membrane (on the cytosolic side). A number of actomyosin regulatory proteins possess specific domains capable of binding to and distinguishing the various forms of PI. Because these signals are membrane bound they inherently remain at the cell perimeter.

2.4.4 PIP signaling in phagocytosis

One of the earliest signaling events in phagocytosis is the transformation of phosphatidylinositol 4-phosphate into phosphatidylinositol-4,5-bisphosphate [133]. PI(4,5)P₂, in turn,

Myosin II

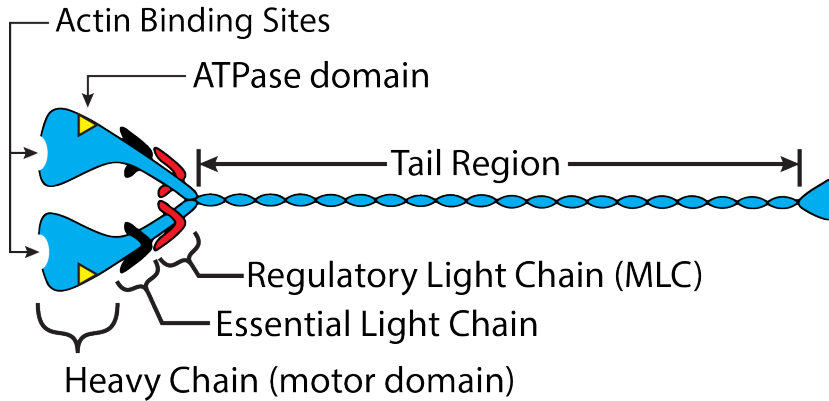


Figure 2.7: Cartoon schematic of myosin II. Myosin II is formed by 6 protein sections: Two motor heavy-chain head groups which exert forces on F-actin, two essential light chains, and two regulatory light chains (MLCs). Myosin activity is enabled or disabled by phosphorylation of the regulatory light chains. Motors aggregates into small fragments through interactions in their tail regions.

signals the deactivation of enzymes which suppress polymerization of F-actin [16]. This includes removal of proteins (Capz, CapG) which cap the end of F-actin and inactivation of ADF/cofilin, which causes actin filament to dissociate. PIP_2 also stimulates an enzymatic cascade which ultimately enables ARP2/3 induce F-actin branching [67]. Growth of actin filaments and expansion of the network through branching drives large scale cellular deformations around the target particle. Subsequent phosphorylation of PIP_2 , by PI3-kinase, creates $\text{PI}(3,4,5)\text{P}_3$ which signals the activation of the Rho family of GTPases (Rho, Rac, and Cdc42). These GTPases have been implicated in a number of down-stream processes including: further stimulation ARP2/3 mediated actin growth, bundling of actin into stress-fibers, and activation of myosin motor proteins [67].

2.4.5 Myosin is stimulated by parallel pathways

During phagocytosis, as well as spreading and migration, myosin II activity is regulated by two parallel pathways. As discussed in the previous section, one of these pathways is PIP_3 dependent. The other pathway depends on the local concentration of Ca^{2+} . Myosin II is a hexamer composed of two heavy chains, two essential light chains, and two regulatory light chains (illustrated in Figure 2.7). The heavy chains form the motor head unit and contain

actin binding domains and ATPase domains. When activated, myosin hydrolyses ATP into ADP. This energy liberation powers the ratchet mechanism which enables myosin to pull itself along F-actin. Myosin activity is predominantly regulated by conformation-altering phosphorylation sites located in the regulatory light chains, often called myosin light chains or MLCs.

Thus far, three classes of enzymes have been shown to be the primary activators of MLC: myosin light chain kinase (MLCK), Rho-associated kinase (ROCK), and p21-activated kinase (PAK) [17]. Myosin is also deactivated by MLC phosphatase, which counteracts MLCK, ROCK, and PAK by dephosphorylating the MLC [76]. MLCK activity is Ca^{2+} dependent. ROCK and PAK are both dependent on PIP_3 . The activities of ROCK are discussed more frequently in migration and spreading literature, although both ROCK and PAK are implicated in those processes. MLC phosphatase is also regulated by PIP_3 related machinery.

2.5 *Remarks*

As is perhaps apparent from the preceding discussion, the phagocytosis signal cascade is a complex coordination of both chemical and physical cues, a product of both temporal and spatial organization. The signaling proteins involved in this cascade are small (typically no larger than 5 nm), yet they coordinate the cell's activity over comparatively expansive distances. Due to the physical limitation of traditional microscopy techniques there have been few studies which investigate the connection between those chemical signals and the actin structures ultimately responsible for executing cell behavior. Because they are confined to a plane, “universal” cell spreading and migration are well suited to traditional microscopy. In recent years an extensive framework concerning the physics of both of these behaviors has emerged. This framework is based on experimental evidence and quantitative modeling. These experiments and models shed light on a number of cellular behaviors closely related to phagocytosis, including: an explanation of how cells drive membrane protrusions and ways the underlying cytoskeletal network can undergo changes facilitating the transition between cell behaviors.

2.5.1 Summary of work

In the subsequent chapters, I leverage the fact that there is prominent overlap between phagocytosis, “universal” spreading, and migration.

2.5.1.1 Chapter 3 - Materials and methods

Chapter 3 details the experimental methods used throughout this document. I introduce and explain the concept of “frustrated” phagocytosis; I describe the microscopy techniques used in the experiment; finally, I discuss the motivation and development of the techniques used to quantitatively analyze the results of our experiments.

2.5.1.2 Chapter 4 - Frustrated phagocytosis characterization

In Chapter 4 I develop an experimental assay for interrogating planar “frustrated” phagocytosis (FP). This geometry enables the direct comparison between phagocytosis and the other two behaviors. These experiments confirm that despite the change in geometry, FP reproduces traditional phagocytic behaviors.

2.5.1.3 Chapter 5 - Late-stage frustrated phagocytosis

In Chapter 5 I discuss our investigations of actin network architecture during FP. Our results demonstrate that late-stage phagocytic contraction involves the formation of a “contractile actin belt.” The belt appears morphologically similar to the actomyosin midline present in migrating cells. Measurements of the contractile forces generated by this structure reveal that phagocytosis involves the exertion of cellular forces comparable to those observed during cell migration.

2.5.1.4 Chapter 6 - Myosin’s role during frustrated phagocytosis

In Chapter 6 I investigate the role of myosin in late-stage phagocytosis. Our experiments demonstrate that late-stage contraction is myosin dependent and that the level of myosin activity within the cell determines how a cell progresses through the three phases of “universal” spreading.

2.5.1.5 Chapter 7 - Hydrodynamic model of cell spreading

In Chapter 7 I present a generic model of cell spreading. The model conceptualizes cell spreading as a wetting process. It is built on top of the mathematical framework of hydrodynamic wetting theory, which is traditionally used to describe how viscous fluids spread on dry substrates. Unlike many models of cell behavior, which are built around molecular scale processes, this model integrates experimentally measured macroscopic characteristics of the cells. It generates spreading rates during P0 and P1 spreading similar to those observed during experiments and predicts how physical properties of the cell such as viscosity and membrane tension affect spreading behavior.

2.5.1.6 Outlook

Combining the results presented throughout this thesis, I posit that the governing mechanics of phagocytosis, spreading, and migration share a common underpinning. Compared to the other two behaviors, unique features of the phagocytic biochemical signal cascade tune phagocytes to engage in late-stage contraction. The techniques developed during the course of this research facilitate quantitative methods for analyzing cellular activity and enable high-resolution imaging of biomolecular activity. This development constitutes the groundwork necessary to quantitatively interrogate the connection between processes within the phagocytic signal cascade and the biophysical machinery responsible for carrying out cellular behaviors.

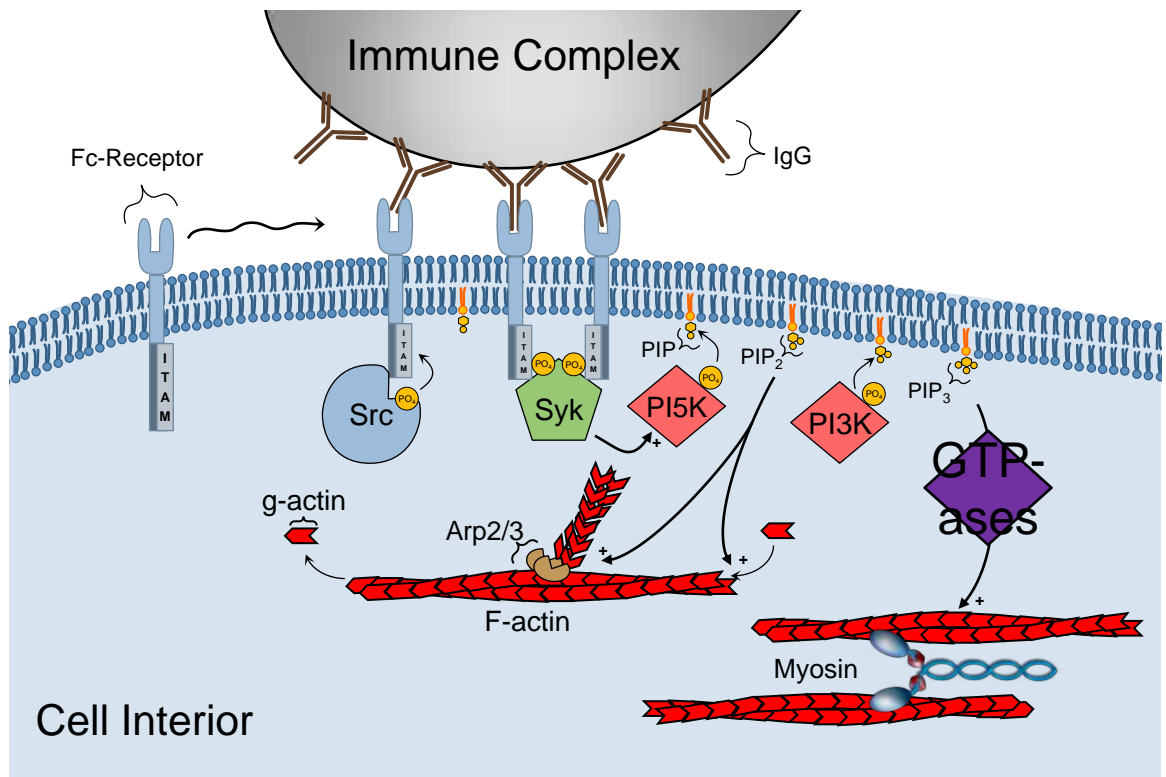


Figure 2.8: Phagocytosis Signal Cascade. Read from left to right. Upon binding of IgG, Fc-receptors otherwise free to diffuse become localized. Once localized, ITAM domain of bound Fc-Receptor is phosphorylated (yellow circle) by Src kinases. Phosphorylated ITAMs bind to tandem sites on Syk which activates various components of the phagocytosis biomachinery, including phosphatidylinositol kinase (PI-K). PI-K transforms local signaling phospholipids (PIP_x) into their active state. PIP₂ upregulates the actin polymerization machinery driving lamellipodia-like protrusion around the target. Later, PIP₃ engages the acto-myosin machinery which has been shown to further stimulate cellular protrusion and is thought to be responsible for particle internalization.

CHAPTER III

MATERIALS AND METHODS

3.1 Frustrated Phagocytosis

To sidestep the technical challenges associated with imaging live cells undergoing phagocytosis, we resort to observing cell behavior as they interact with opsonized planar surfaces, termed *frustrated phagocytosis*. Under this configuration, microscope coverslips are functionalized with phagocytosis-stimulating IgG antibody. The slide is then mounted on an inverted microscope and cultured cells are deposited onto the surface. As the cells settle to the surface, their real-time behavior can be recorded. By isolating the majority of the phagocytosis-related processes to a single plane we are able to take advantage of a multitude of standard imaging techniques. For example, reflection interference correlation microscopy (RICM) allows us to image the exact positions a cell makes contact with the surface. Total internal reflection fluorescence (TIRF) allows us to image fluorescently tagged structures close to the surface with high precision. Video-microscopy allows us to record cell behavior in real-time. Finally, the planar geometry is compatible with well-established lithography techniques, allowing precise spatial control of surface bound ligands.

3.1.1 FP surface preparation

It is important that coverslips be uniformly opsonized with a controllable density and that IgG antibodies remain affixed to the surface throughout the course of an experiment. To accomplish this, surfaces were prepared using a four-step process.

3.1.1.1 Initial Cleaning

To eliminate surface bound debris which could affect phagocytic behavior and cause imaging artifacts, surfaces were washed using a multistep protocol. First, No. 1.5 coverslips (VWR: 48366-227) were rinsed using DI-H₂O. Next, coverslips were degreased by sonication in baths of reagent grade acetone, reagent grade ethanol, and DI-H₂O. Finally, coverslips

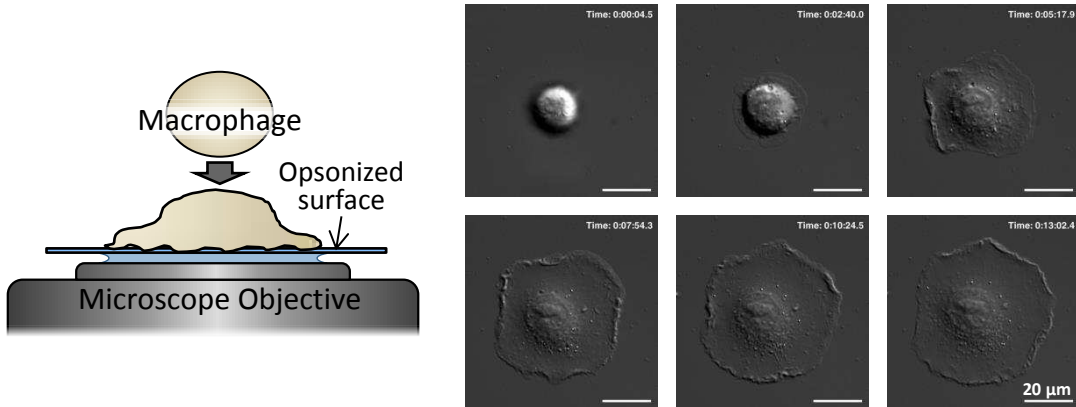


Figure 3.1: Frustrated Phagocytosis. Cultured macrophages are deposited onto opsonized coverslips mounted on an inverted microscope. Upon contact with the surface, cells exhibit a phagocytic response. Over the course of 10-15 min cells rapidly spread, reaching contact areas 3-5 times their initial size.

were dried under N₂.

3.1.1.2 Amino-silanization of coverslips

Bovine Serum Albumin (BSA) was covalently cross-linked to the coverslip surface via amine crosslinking. This method requires that the surface contain primary amines to which the protein can be coupled. Amine-groups were added to the silica glass surface using amino-silanization. First, coverslips were etched by sonication in 1 N NaOH. Etching exposes OH-groups on the glass surface to which silane can be coupled. Next, coverslips were gently rinsed with DI-H₂O, dried under N₂, and then baked at 100 °C for 1 hour to remove excess water. The glass surface was silanized with (3-Aminopropyl)triethoxysilane (APTES) via physical vapor deposition. Etched coverslips were placed in a glass desiccator along with 100 μL of APTES (Sigma: 440140-100ML). Desiccator was evacuated with a vacuum pump to a pressure of approximately -25 inHg. Next, desiccator was heated to 95 °C for 40 minutes. This vaporized the APTES. Finally, the desiccator was allowed to cool for 20 minutes before coverslips were removed. Coverslips were stored under vacuum for up to 2 weeks before use.

3.1.1.3 BSA functionalization

BSA (Sigma: A2153) was covalently coupled to the amino-silanized surface using gluteraldehyde. Silanized coverslips were incubated in 1% volume/volume gluteraldehyde in DI-H₂O at room temperature for 40 minutes. Coverslips were rinsed with water and then incubated in 1 mg/mL BSA in PBS for 40 minutes. Finally, coverslips were rinsed again, dried under N₂, and stored under vacuum for up to 2 weeks.

3.1.1.4 Opsonization

Surfaces were opsonized using anti-BSA serum protein. Anti-BSA (Rockland: 101-4101) was diluted to 10 mg/mL in PBS. (Note: experiments presented in Chapter 4 were conducted with concentrations listed in that chapter.) To conserve anti-BSA solution, 200 μL droplets were pipetted onto a piece of parafilm and coverslip were gently placed on top, ensuring bubbles were not formed in the glass-solution sandwich. Coverslips were incubated with the anti-BSA solution for 1 hour at room temperature. They were then rinsed, dried, and stored under vacuum for up to 2 weeks.

3.1.2 Frustate phagocytosis assay

Live-cell experiments were conducted using cultured macrophages at physiological conditions. (Cell culture protocols are listed below.) One day prior to experiments, J774A.1 macrophages (ATCC: TIB-67) were split into 25 cm polystyrene petri dishes at a density of 100,000 cells/dish. 30 minutes prior to the start of an experiment culture media was exchanged with DMEM supplemented with HEPES (Corning cellgro 15-018-CV) and cells were scrapped from the surface and re-suspend by repeated pipetting. Cells were then allowed to recover in suspension by tumbling in a sealed test-tube at 37°C for 30 minutes.

At the start of an experiment, opsonized coverslips were mounted to a custom Teflon culture ring. Samples were then mounted on an inverted microscope (Nikon TE-2000) equipped with a temperature and humidity controller (LiveCell brand). For each experiment, 100 μL of suspended cells were pipetted onto a mounted coverslip and then covered with 2.5 mL of pre-warmed DMEM+HEPES. Cells were imaged and tracked using reflection

interference correlation microscopy and custom written software (see below).

3.2 Cell culture

The experiments conducted throughout this thesis examine the behavior and mechanics of phagocytosis. These experiments were conducted using live cultured macrophage cells. All of the original experiments discussed throughout this thesis were performed using the immortalized J774A.1 mouse monocyte-macrophage cell line.

The J774A.1 cell line was chosen for this work for two reasons. First, this cell line has been used in numerous immunological assays and its biological characteristics are well characterized [104, 120, 47, 46]. This cell line is known to express Fc γ -receptors and undergoes phagocytosis when presented with opsonized IgG targets [109]. Second, baseline mechanical characteristics of the J774A.1 cell line were previously documented by Lam *et al.* [81]. In the work presented in Chapter 7 we use these characteristics to model and interpret the results of some of the experiments presented throughout this thesis.

J774A.1 cells were obtained from ATCC.org. Following established protocols [50], J774A.1 macrophages were cultured in Dulbecco's Modified Eagle's Medium (DMEM) supplemented with 10% FBS (fetal bovine serum, Corning CellGro: 35-010-CV). One day prior to experiments, the cells were split into 25 cm polystyrene culture dishes at a density of 100,000 cells/dish. A half-hour before the start of an experiment culture media was exchanged with DMEM supplemented with HEPES (Corning CellGro: 15-018-CV) and cells were scrapped from the surface and re-suspend by repeated pipetting. Cells were then allowed to recover in suspension by tumbling in a sealed test-tube at 37°C for 30 minutes.

3.3 Reflection Interference Correlation Microscopy (RICM)

Real-time spreading behavior was monitored using Reflection Interference Correlation Microscopy (RICM) microscopy. Under RICM, cells are imaged under polarized light through epi-illumination. Constructive and destructive interference between light reflecting off the bottom of a cell and the underlying coverslip results in the appearance of light and dark fringes. The shade of these fringes depends on the distance between the cell and coverslip [85].

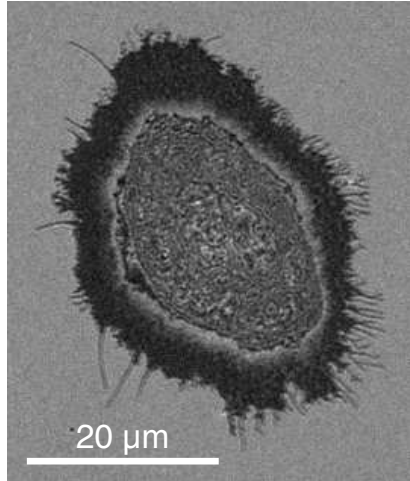


Figure 3.2: Cell imaged using RICM. Dark patches on perimeter of cell indicate close attachment of membrane and substrate. Region in center shows complicated fringes due to presence of ruffles in the membrane near the surface, and additional reflections caused by structures within the cell body. Sample was illuminated with incoherent light.

As illustrated in Figure 3.2, under epi-illumination (illumination through the lens of an inverted microscope) light imposed on a sample undergoes a reflection at each interface the wave front encounters. Upon reflection these wavefronts constructively and destructively interfere. For light traveling from a material with a high index of refraction (n), into a material with a lower n , and again into a high n material, two reflections will occur. In the case where the incident light is coherent, the intensity of the reflected light is given by

$$I = \left| \sum \vec{E} \right|^2 = \left| \vec{E}_{1,2} + \vec{E}_{2,3} \right|^2 = I_{1,2} + I_{2,3} + 2\sqrt{I_{1,2}I_{2,3}} \cos(2k\delta + \pi), \quad (3.1)$$

where k is the wavenumber of the incident beam, δ is the distance the light travels within the low n material, and $I_{i,j}$ are the intensities of each reflection. Notice that for $\delta \rightarrow 0$ (i.e. the third medium is close to the first) the total reflected intensity is at a minimum.

When RICM is used to image cells, the equation listed in eq 3.1 is complicated by the presence of additional interfaces and the use of incoherent light; however, the qualitative trends remain the same. Under RICM, locations where a cell makes direct contact with the underlying surface appear as dark patches on an otherwise gray background. An example is included in Figure 3.2

In addition to a research-grade inverted microscope, RICM requires four major components: an epi-illumination light source, a semi-reflective mirror, and two linear polarizers. A

schematic of our RICM setup is shown in Figure 3.3. Under this setup, the epi-illumination source (in our case a fiber-coupled mercury lamp) is aligned for Koehler illumination with the objective used to image the sample. Within the illumination beam path a wavelength band-pass filter selects the color of illumination, followed by the aperture stop (which is adjusted to increase/decrease the coherence length over which interference occurs), the field stop (which selects the size of the field of view), a linear polarizer, and a semi-reflective mirror (which directs light into the objective). The objective focuses light onto the sample. Reflected light is imaged through the objective, passes through the semi-reflective mirror in the beam path, travels through a second linear polarizer and is imaged through the optics of the microscope.

The polarizers in the illumination and reflected path are orientated to select s-polarized light (light parallel with the surface of the semi-reflective mirror. In principle, by matching the polarizers, only light which is reflected from the sample surface will be image at the camera. In application, reflections from lens-elements within the objective cause stray illumination artifacts. One method of eliminating these artifacts is to use a specially designed “anti-flex” objective which includes a quarter-wave plate as the last optical element in the objective, which ensured that only light reflected from the sample passes through the second polarizer [85]. Due to added cost, an “anti-flex” objective was not used in the work related to this thesis. Instead, artifacts caused by in-objective reflections were eliminated using software background correction methods (see below).

3.4 Image analysis

3.4.1 RICM background correction

Under RICM, cell-substrate contract regions appear as dark patches interrupted by bright fringes. As shown in Figure 3.2, these patches are distinct from the cell surrounding (which appear gray). Using these intensity differences, cell shape can be identified using simple image intensity digital filters. However, before such methods can be applied, artifacts due to in-objective reflections must be eliminated.

Reflection artifacts can be removed using a straightforward image subtraction technique.

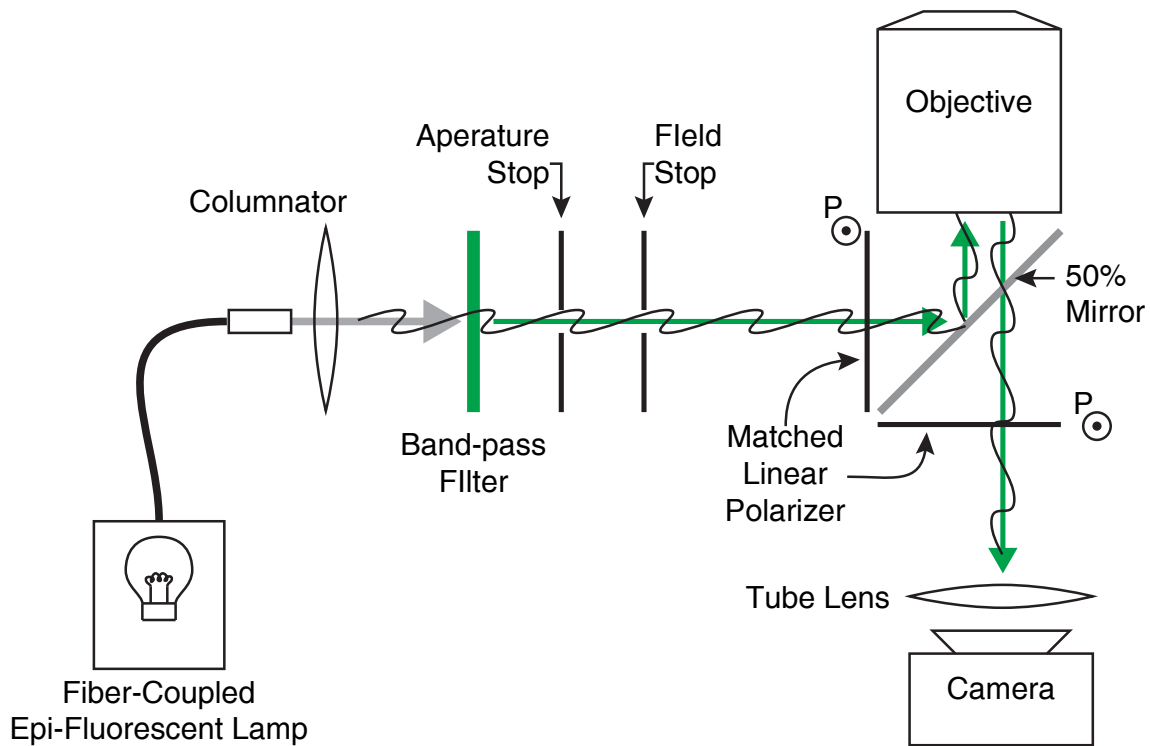


Figure 3.3: Schematic of RICM. A fiber-coupled Hg lamp serves as the illumination source. Using the optics of the microscope, the epi-illumination beam is aligned for Koehler illumination. Along the illumination path, a band-pass filter selects the color of illumination, the aperture stop is used to adjust the beam coherence, and the field stop selects size of the field-of view. Light is reflected into the objective using a 50% mirror. Reflections from the sample are imaged by the objective and pass through 50% mirror in the optics of the microscope (tube lens, camera). Matched linear polarizers are placed before and after the 50% mirror to ensure only sample reflections are imaged. The orientation of these polarizers is set parallel to the 50% mirror (into/out-of the page).

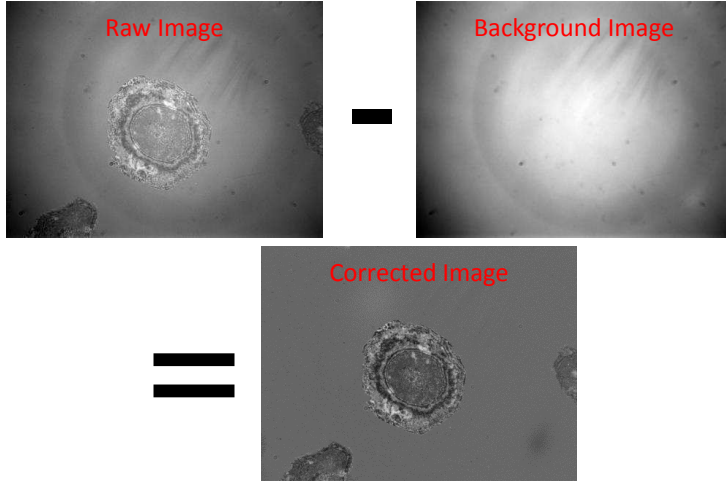


Figure 3.4: Background subtraction. Artifacts due to dust on camera and reflections within the objective can be removed by subtracting a background image captured before the start of an experiment from each frame in a video sequence.

Prior to the start on an experiment, a sample (without cells) is mounted on the microscope, and brought into focus. Using the same illumination setting used during the course of experiments, a background image is captured. After an experiment is conducted, the pixel-per-pixel values of this background image are subtracted from the frames captured during the experiment. The resulting video sequence is artifact-free and has a flat illumination pattern. This process is illustrated graphically in Figure 3.4.

Once the background has been subtracted, cell contact area is identified by applying a simple intensity filter to the corrected images. Intensity thresholds are selected by a user to match the intensity values corresponding to dark patches and bright fringes within a typical cell. Pixels below the dark-value and above the light value are designated as “true” in a binary mask; pixel values within that range are designated as “false”. Holes in the binary mask are filled using standard image processing fill routines. Next, pixel-clusters below a minimum area threshold (typically 10-50 pixels) are eliminated, resulting in a binary mask identifying the cell. Using this mask, morphological image analysis operations can be performed to identify the cell perimeter, contact-area and centroid. Centroids can be used to track cell motion through a time-series. The cell perimeter and area can be used to calculate rates at which cells spread over the substrate.

3.5 Morphological profiling of cells

A common metric used to characterize cell spreading processes is to measure the velocity ($\mu\text{m}/\text{s}$) at which cellular protrusions move. This velocity is usually defined relative to vectors normal to a cell's perimeter. Measurements of protrusion speed have been used to identify shifts in cell behavior over the course of spreading and migration processes [44, 45] and to compare behaviors of different cell types [88].

3.5.1 Level-set method for interpolating changes in cell shape

Central to calculating the local edge velocity is tracking edge locations from one frame to the next. In the cases where the local curvature remains roughly the same between two consecutive frames the location of an edge marker in the first frame can be projected onto the second by finding the intersection of the normal-line at that point with the edge-contour of the next frame. Once edge markers have been propagated, the velocity is simply calculated as the change in marker displacement divided by the time between each frame. As illustrated in Figure 3.5a, this simple definition fails for situations where local curvature changes quickly. In these situations, projecting edge-markers along normal-lines yield non-physical displacements. Given video-sequences of high enough frame rates this would not be an issue as local curvature would not change rapidly enough to produce significant errors.

Limitations of our automated imaging system prevent capturing frame-rates much higher than one image per 10-15 seconds. At this reduced frame rate, rapid changes in local curvature are not uncommon. We bypass this issue by interpolating a series of contour lines which evolve the first frame into the second frame [88]. Interpolated contours are calculated using an algorithm based on level set methods. Level set methods provide a robust framework for describing the evolution of contours and interfaces. These methods have been employed in a number of contexts including fluid flow, droplet formation, heat transfer, path optimization and even adaptive image processing. The texts by Sethian, Osher, and Fedkiw thoroughly develop the methods and provide a number of example applications [124, 99].

At their core, level set methods define the geometry of an N-dimensional interface as a level set of an $N+1$ -dimensional implicit function defined as the signed distance of a point

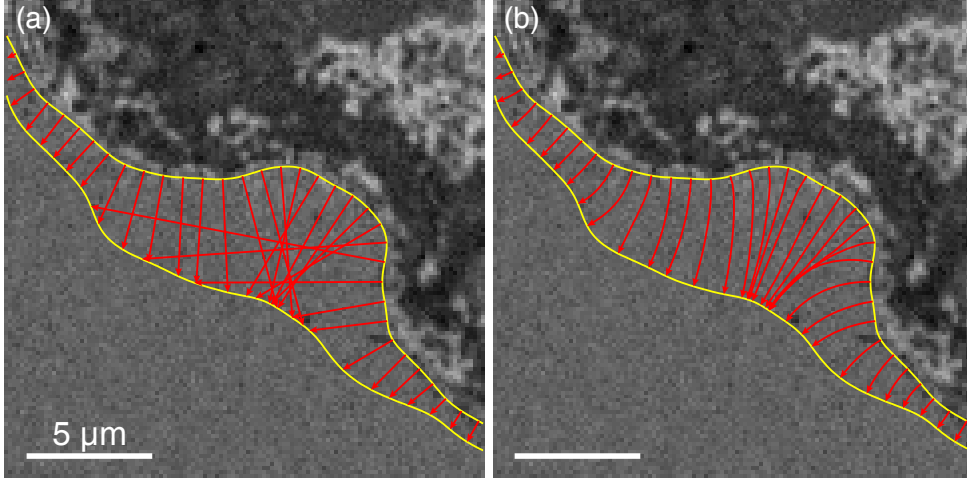


Figure 3.5: Edge marker propagation. (a) Projecting local normal-lines from contours of negative curvature results in non-physical estimates of marker displacement. (b) Intermediate frames, interpolated using level-set algorithm enables propagation of markers following physically reasonable trajectories. Displacement of edge markers can be used for calculation of local protrusion/retraction activity.

from the interface. For example, under LSM, a circular contour line $\vec{x}(s)$ of radius $r = 1$ could simply be described as the zeroth level set of the cone $\phi(x, y, t) = 1 - \sqrt{x^2 + y^2 + 2}$. By defining contour lines this way the surface can be evolved using the simple convection equation

$$\frac{\partial \phi}{\partial t} + (\vec{V}(x, y, t) \cdot \nabla \phi) = 0. \quad (3.2)$$

For our purposes it is only necessary to evolve the contour in the normal direction. This simplifies the convection equation to

$$\frac{\partial \phi}{\partial t} + F(\phi) |\nabla \phi| = 0, \quad (3.3)$$

where $F(\phi)$ is a function which dictates the local edge velocity.

Under our interpolation scheme, the cell edge is identified in each frame of a video sequence. Using this contour, we construct a video sequence where pixel values correspond to the signed distance from the cell perimeter. Methods for efficiently calculating signed distance functions are outlined in Sethian's text [citeSethian1999](#). For each pair of consecutive frames denoted by T_1 and T_2 the goal is to calculate a series of implicit functions

$\phi(T_1), \phi(T_1 + \delta t), \phi(T_1 + 2\delta t), \dots, \phi(T_2)$ which approximate a smooth evolution. Intermediate steps are calculated by iteratively integrating eq 3.3 for periods δt . Central to this calculation is determining a speed function $F(\phi)$ which progressively causes the level set to converge to the final function. One of the simplest choices is to define

$$F = \phi(t) - \phi(T_2). \quad (3.4)$$

Notice when the current function is equal to the target, F becomes uniformly zero and eq 3.3 no longer changes the values of ϕ . A number of convergence schemes and their performance are outlined in Machacek *et al.* citeMackacek2006. Experimentation with our implementation of the level set algorithm revealed

$$F = \tanh(\phi(t) - \phi(T_2)) \quad (3.5)$$

is well suited for interpolating intermediate frames. For small deviations from the target shape $\tanh()$ performs similar to the simple difference scheme; however, for large deviations F is clamped to a fixed value meaning the contour line is only moved a set distance during each iteration.

The interpolation algorithm is outlined in Figure 3.5. Numerical integration was implemented in MATLAB using the “Levelset Toolbox” developed by Ian Mitchel and available at <http://www.cs.ubc.ca/~mitchell/ToolboxLS/> [93]. Interpolating frames were computed until the residual function

$$R = \frac{\sqrt{\sum_{x,y} (\phi_t - \phi_{T_2})^2}}{Width(\phi_t) \cdot Height(\phi_t)}, \quad (3.6)$$

which essentially measures the per-pixel error, converged to a target value (typically 10^{-5}). Once the interpolated functions were obtained the zeroth level sets were fit with piece-wise smooth periodic spline curves. As shown in Figure 3.5b, edge markers were propagated along the normal-lines for each interpolated level-set. The distance traveled by an edge-marker was assumed to be the path-length of its associated normal-line and the local edge velocity was simply calculated as that distance divided by the time between the initial and target frames.

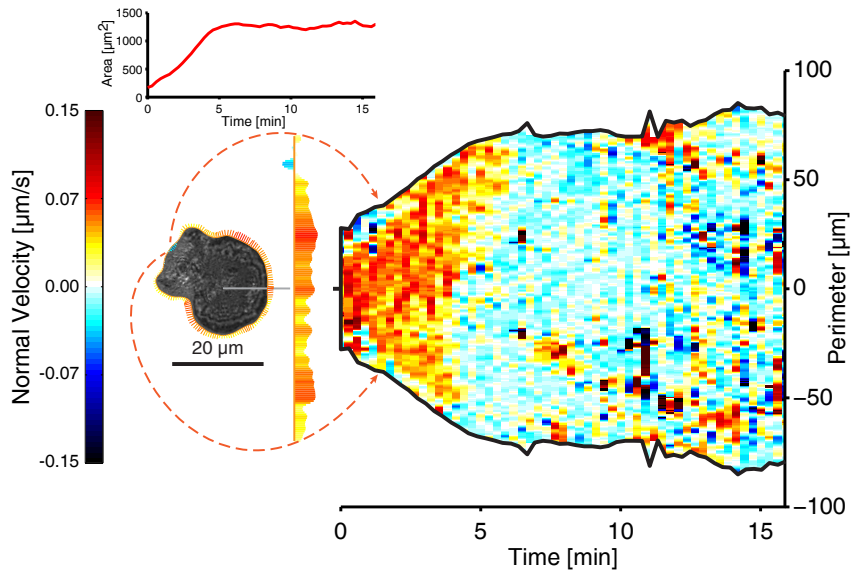


Figure 3.6: Protrusion/retraction activity map of untreated macrophage during frustrated phagocytosis. Edge velocity rates are aligned to a user selected center line, denoted by 0th position. Edge activity is concatenated into a time-ordered array and plotted as a heat-map. This particular cell spreads roughly symmetrically for the first 3 minutes of contact with the opsonized surface. From 3-7 minutes the cell undergoes slight polarization as growth activity (red-yellow) concentrates towards the top half of the cell. After 7 minutes the cell undergoes slow contraction (light blue). In later stages of contraction (10-15 min) retraction tethers prevent accurate measurement of edge activity resulting in numerous isolate dark patches and rapidly changing perimeter length.

3.5.2 Activity maps

Using the algorithm discusses above it is possible to visualize correlations in protrusion and retraction rates along the perimeter of a cell during spreading and migration. A common way of visualizing protrusion and retraction rates is by assembling time-series data into time-ordered activity maps. As depicted in Figure 3.6, edge velocity activity maps are created by “unwrapping” protrusion/retraction calculated along the cell perimeter and ordering that data into a 2-d heat-map of cell activity. Under our implementation, a center line is chosen by a user to denote the 0th position. Center lines are typically chosen such that they are centered in regions of high cell activity, placing that region at the center of the activity map. It should be noted that as cells contract during late stages of FP they form retraction tethers. Retraction tethers are difficult for our image processing algorithms to segment properly, resulting in errors in both contact area measurements as well as protrusion/retraction rate calculations. In activity maps these errors appear as very dark isolated patches in regions where the perimeter appears to fluctuate rapidly.

3.6 Structured Illumination Microscopy (SIM)

In the experiments presented in Chapter 5, actin structure is visualized by fluorescence microscopy. Fluorescent microscopy is a common technique used to identify and locate protein structures and biochemical signals within cells. The principles of fluorescence microscopy are relatively simple. First, a molecule or structure of interest is chemically labeled with a fluorescent dye molecule. Next, the labeled sample is imaged under a microscope while being illuminated with a light of a wavelength that excites the fluorescent dye. Dye molecules absorb photons of the exciting light dissipate a fraction of the energy associated with those photons and then emit photons with energies equal to the difference between the excitation energy and dissipated energy. Because they have less energy, emitted photons are red-shifted compared to absorbed photons. Within the optics of the microscope, colored filters only allow light within the emission range of a chosen dye to pass on to the imaging system (i.e. camera, photo-detector, or ocular).

The resolution of any optical system is limited by the Abbe diffraction limit. Because

photons are quantum mechanical waves, the resolution of a lens-based imaging system is limited to only being able to distinguish structures separated by at least a distance

$$d = \frac{\lambda}{2 \cdot \text{NA}}, \quad (3.7)$$

where λ is the wavelength of light being imaged and NA is the numerical aperture of the lens system being used to image the structures. For a typical research-grade microscope imaging green fluorescent structures, this equates to a resolution limit of approximately 200–300 nm.

Within a cell, 200 nm is too coarse to resolve structural features of the actin cytoskeleton. For instance, previously published fluorescent images of actin in active phagocytes have lacked the clarity necessary to accurately assess whether F-actin bundles into a ring-like structure during phagosome closure (as predicted by the contractile-belt model, see Chapter 2.3.1) or simply remains in an interwoven network consistent with ARP2/3 induced branching.

The experiments of Chapter 5 overcome this issue through the use of sub-diffraction limited Structured Illumination Microscopy (SIM). SIM was pioneered by Gustafsson, Heintzmann and Cramer [63, 65]. The technique provides a 2x enhancement of lateral resolution over the Abbe diffraction limit of traditional microscopy techniques. Resolution enhancement is achieved by spatially modulating the illumination pattern imposed on a fluorescent sample. This modulation creates a Moiré pattern with the underlying structure of the fluorescently labeled objects, revealing detail obscured by blurring which results from the diffraction limit.

The conceptual underpinning of SIM can be understood by recognizing that the diffraction limit confines the encoded image information to a circle of radius $k_{\text{limit}} \approx \frac{\pi}{d}$, where d is the diffraction limit defined in eq 3.7 (see Figure 3.7f). By illuminating images with a periodic Moiré pattern, spectral information is shifted laterally in Fourier-space. If the imposed pattern has periodicity $k = \frac{\pi}{d}$, the Fourier-space information lies within circles centered round $k = \pm \frac{\pi}{d}$. Rotating the imposed pattern over the angles $\theta = [0, 2\pi]$ generates a complete image sampled at a resolution limit defined by $k_{\text{limit}} = 2\frac{\pi}{d}$ (Figure 3.7a,g) [126].

For the experiments presented in Chapter 5, fluorescent SIM images were captured using

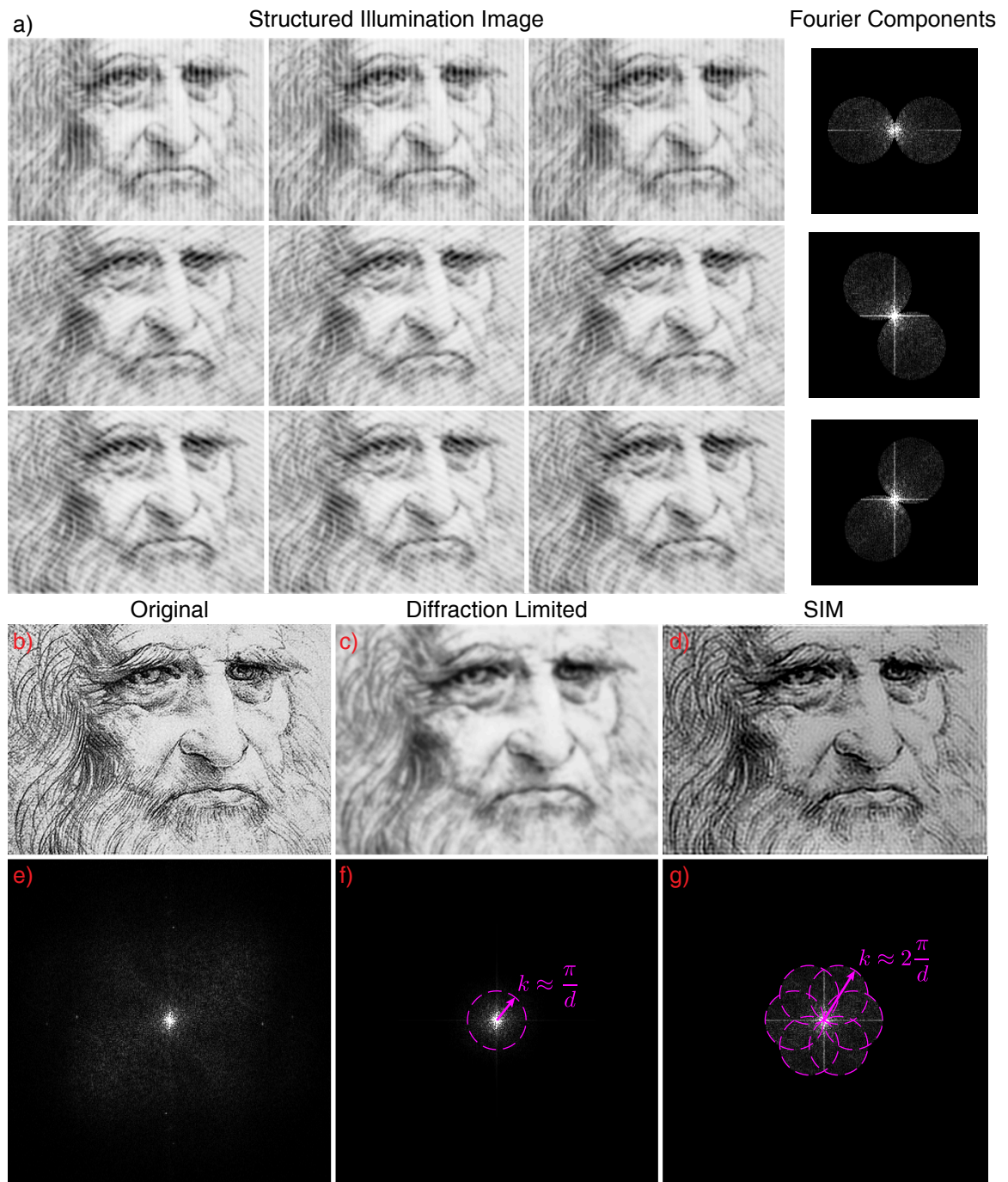


Figure 3.7: Structured Illumination Microscopy calculation. (a) Fluorescent images are captured under Moiré patterned illumination. For each rotation, the periodic pattern is phase shifted to $\phi = \{0, 2\pi/3, 4\pi/3\}$. Resulting images are used to compute extended Fourier-space images. (b) Original image, before diffraction limited blurring. (c) Image with diffraction limit imposed. (d) Reconstructed image based on SI data in (a). (e-f) Fourier-transforms of images (b-d). Combined SI data yields 2 \times increase in the resolution limit.

a pre-built *Zeiss Elyra Structured Illumination System*. The microscope consisted of a Zeiss 780 microscope chassis, a PS.1 confocal unit, and an Elyra super-resolution SIM unit configured for illumination with 405, 488, and 546 nm lasers using a 63x NA=1.4 objective. SIM reconstruction was computed using the included Zeiss *Zen Black Image Analysis* software.

3.7 Traction Force Microscopy (TFM)

Traction force microscopy is quickly becoming a staple technique in many cell mechanics labs. Recent years have seen the development of straightforward protocols and improvements in force analysis algorithms [103, 6]. The principles behind TFM are relatively straightforward. Cells are deposited on to elastic surfaces which contain fluorescent tracker particles. As cells exert forces the underlying surface becomes deformed. These deformations can be tracked using the fluorescent tracker particles. Based on observed particle displacement, the stress-field generated by the cell can be computed by solving the inverse-Boussinesq problem [25]. An overview of TFM is depicted in Figure 3.8. A complete protocol for creating elastic substrates and performing live-cell TFM experiments is included in Appendix A.

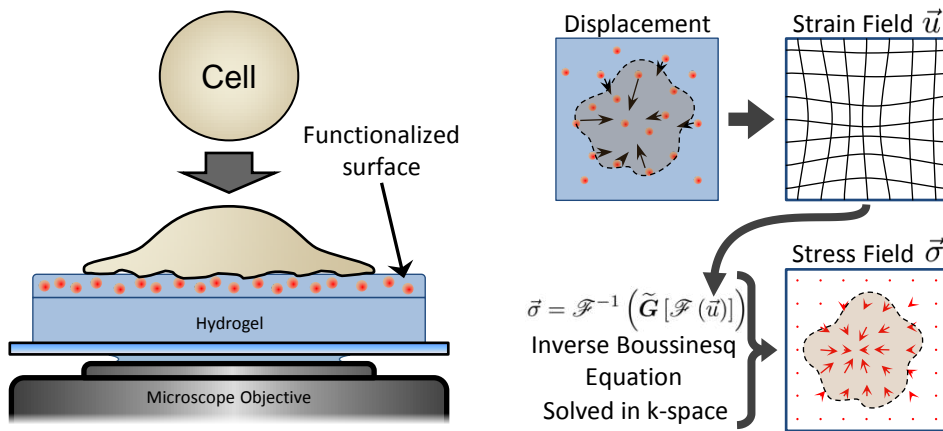


Figure 3.8: Traction Force Microscopy schematic. Cells are deposited onto elastic hydrogel substrate mounted on a microscope. Substrates contain fluorescent tracker particles which are used to track deformation caused by forces generated by the cells. Deformations can be used to calculate the stress-field generated by the cell using the Boussinesq potentials [25].

CHAPTER IV

CHARACTERIZATION OF FRUSTRATED PHAGOCYTOSIS

4.1 *Overview*

Phagocytosis is a highly dynamic behavior, the result of a complex interplay between biochemical and biomechanical processes. A significant amount of research has been put forth to identify key components of the biochemical signal cascade [62, 112]. Although this research has successfully identified key signaling interactions, open questions still loom as to the precise role, location, and timing of those signals and how they affect the cell's mechanical properties [113]. The most straight forward methods for answering questions about signal location and timing involve live-cell microscopy. The inherent 3-dimensionality and small feature size of phagocytosis make accurate microscopic imaging difficult.

Frustrated phagocytosis (FP) is a 2-D alternative to traditional phagocytosis assays. Under FP instead of presenting phagocytes with opsonized particles, as in traditional assays, cells are deposited onto microscope coverslips which have been functionalized to induce a phagocytic response. Upon contact, cells spread-out as if trying to phagocytose the surface. By confining phagocytosis to a single plane, standard wide-field microscopy techniques can be used to image cell behavior. Compared to traditional assays, frustrated phagocytosis experiments are relatively easy to conduct, are compatible with comparably inexpensive epi-fluorescent and TIRF (total internal reflection fluorescence) microscopes, and are compatible with standard lithography techniques allowing for investigation of cell response to complex patterns of phagocytosis stimulating ligands.

Concerted efforts by the biophysics and cell mechanics communities has led to development of a general framework explaining how the biomolecular machinery related to the actin cytoskeleton orchestrates cell behaviors such as spreading and migration [94, 145]. It has also been established that phagocytosis is dependent on many of these same mechanism [91]. By isolating phagocytic behavior to a single plane, cell behaviors during frustrated

phagocytosis can be directly compared with experimentally observed spreading and migration behaviors. Furthermore, the planar geometry of FP makes it easier to adapt physics based models of spreading and migration to phagocytosis.

The purpose of the work presented in this chapter is threefold.

First

Our primary objective was to determine the conditions necessary to reliably induce frustrated phagocytic spreading. During the initial development of the FP protocol presented in Chapter 3, we found that macrophage FP response was highly variable. This preliminary work revealed that FP response was particularly sensitive to opsonization conditions. In this chapter we present experiments which quantitatively assess the effect IgG opsonization density has on determining FP response.

Second

This work also sought to quantitatively characterize dynamic cell behavior over the course of FP. Although FP has been used as a proxy for traditional phagocytosis [150, 129, 135], typical reports only characterize cells which have been fixed. Consequently, little has been published regarding the dynamical behavior of cells during FP. We use the automated cell-tracking algorithms presented in Chapter 3.4 to measure contact area, spreading rate, and protrusion speed statistics.

Third

We compared frustrated phagocytosis with the spreading behaviors of other cell types. By confining phagocytic activity to a plane, methods used to analyze other forms of cell spreading can be applied to phagocytosis. In particular, we compared dynamic contact area and protrusion activity during FP with the behavior reported for non-phagocytic cell types. Using these metrics we assessed the similarities and differences between the phases of FP and the reported “universal” phases of non-phagocytic spreading.

4.2 Experimental Methods

4.2.1 Frustrated phagocytosis assay

The experiments presented in this chapter constitute our initial analysis and validation of the frustrated phagocytosis protocol presented in Chapter 3. In these experiments, J774A.1 macrophages were deposited onto BSA-functionalized coverslips opsonized with varying densities of anti-BSA IgG.

4.2.1.1 Microscopy methods

Real-time spreading behavior was monitored using Reflection Interference Correlation Microscopy (RICM) microscopy. Under RICM, cells are imaged under polarized light through epi-illumination. Constructive and destructive interference between light reflecting off the bottom of a cell and the underlying coverslip results in the appearance of light and dark fringes. The shade of these fringes depends on the distance between the cell and coverslip [85]. When viewed using RICM, locations where a cell makes direct contact with the underlying surface appear as dark patches on an otherwise gray background. An extended discussion of the fundamental principles of RICM, and its implementation, is included in Chapter 3.

4.2.1.2 Image analysis

Cell-substrate contact area was recorded using custom written cell-tracking software. An overview of this software is included in Chapter 3.4. Through the course of each experiment, RICM video micrographs of cells undergoing FP were captured. Our cell-tracking software provides a frame-by-frame binary contact map specifying regions of cell attachment. Subsequent analyses use these contact-maps were used to parametrize cell behavior yielding metrics such as contact-area, average spreading velocity, and edge protrusion activity.

4.2.2 Opsonin density calibration

A major goal of the experiments presented in this chapter was to characterize the effect of opsonizaton density on phagocytosis. Frustrated phagocytic response to opsonization density was measured by tracking spreading behavior on surfaces prepared using different

anti-serum bath concentrations. Because of the non-linear nature of surface adsorption, it was necessary to determine a calibration curve relating bath concentration to relative opsonization density. The relationship between bath concentration and surface density was determined by fluorescence.

4.2.2.1 Fluorescent labeling of IgG protein and characterization with UV-Vis absorption

Anti-BSA serum protein (Rockland Immunochemicals: 101-4133) was fluorescently labeled using commercially produced Atto-488 NHS esters (Sigma: 41698) following the manufacturer's protocol. Dried anti-BSA protein was reconstituted in PBS to a final concentration of 2 mg/mL. 1 mL of this solution was reacted with 20 µL of 2 mg/mL NHS-Atto-488 (reconstituted in DMSO). Reaction time was 1 hour and was conducted at room temperature, under mild agitation. After labeling, excess dye was removed from solution using a Zeba Spin Desalting Column, 7K MWCO (Thermo: 89891).

Recovered protein concentration and the approximate dye:protein ratio was measured via UV-Visible absorption spectrometry using a Beckman Coulter DU 800 spectrophotometer¹. The unlabeled protein extinction coefficient (ϵ_{280}) was calculated by measuring the slope of a linear regression of UV absorption plotted against protein concentration (see Figure 4.1a).

$$A_{280} = \epsilon_{280} \cdot C \cdot [d = 1 \text{ cm}] \quad (4.1)$$

Recovered protein concentration and labeling ratio were calculated by measuring the absorption spectra of serial dilutions of the recovered solution. Contributions of the Atto488 dye to the absorption at 280 nm were corrected by subtracting the value of the absorption at the dye's maximum absorption-wavelength (501 nm) multiplied by the manufacturer's specified correction factor ($CF_{280} = 0.10$).

$$A_{prot} \approx A_{280} - A_{\lambda_{max}} \cdot CF_{280} \quad (4.2)$$

A linear regression of the corrected UV absorbance plotted against the dilution factor multiplied by the calculated ϵ_{280} yielded the approximate protein concentration. Finally,

¹ A thorough discussion of absorption spectrometry can be found in [119].

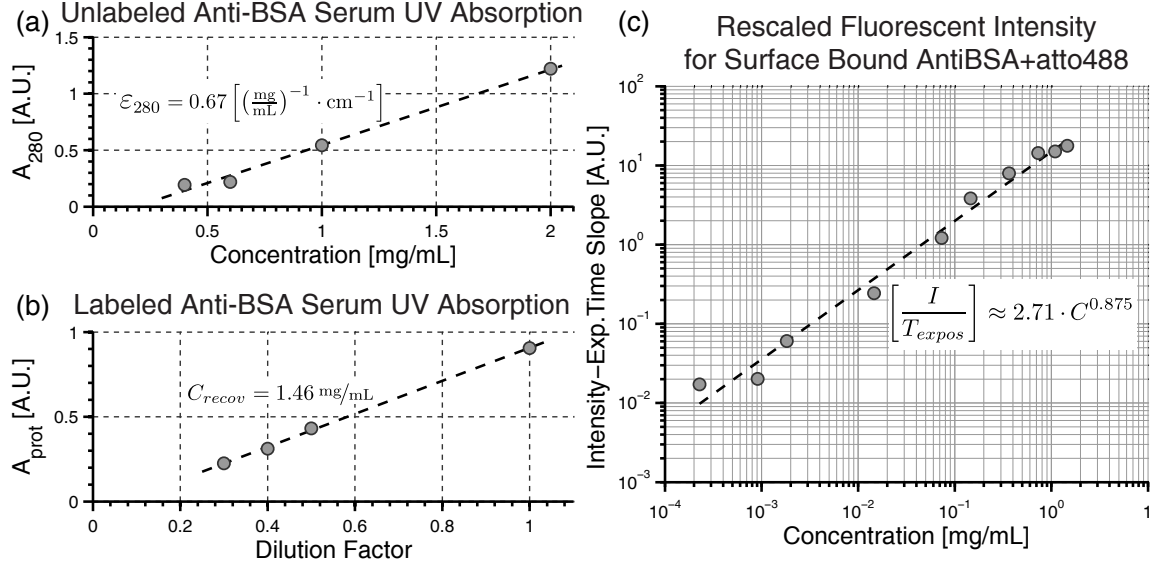


Figure 4.1: Opsonin density calibration. Opsonin density calibration. (a) UV absorption of unlabeled protein, used to calculate extinction coefficient for anti-BSA serum protein. (b) Estimated UV absorption by atto488-labeled serum protein plotted against dilution factor. Slope yields $C_{recov} \cdot \epsilon_{280}$. (c) Log-Log intensity vs solution concentration curve. Curve is roughly linear suggesting opsonin density scales with solution concentration.

using the molecular weight of IgG (MW \approx 150 kDa) as an estimation of the molecular weight of the anti-serum protein, the degree of labeling (dye/protein) was calculated by taking the ratio of dye concentration (measured at 501 nm) to the calculated protein concentration.

$$DOL = \frac{A_{\lambda_{max}}/\epsilon_{280}}{(A_{280} - A_{\lambda_{max}} \cdot CF_{280})/\epsilon_{280}} \quad (4.3)$$

These results are summarized in Table 4.1.

4.2.2.2 Fluorescent intensity of surface bound IgG varies linearly with concentration

Surfaces of varying opsonin density were prepared by soaking BSA-functionalized coverslips in solution of fluorescently labeled anti-BSA serum for 1 hour at room temperature. Solution concentrations ranged from 200 ng/mL to 1.5 mg/mL. The surfaces were mounted to sample holders, covered with water and fluorescently imaged. The objective used was a Nikon Plan Fluor 40x/1.30 oil immersion lens. The sample was illuminated by a Nikon Intensilight C-HGFI illuminator with a FITC compatible filter cube. Images were captured using a Photometrics CoolSnapHQ2 camera, set to 1x gain and 10 Mhz readout. To avoid artifacts

Table 4.1: UV-Vis. absorption parameters.

| | |
|------------------|---|
| λ_{max} | 501 nm |
| ϵ_{max} | $9 \times 10^4 \text{ M}^{-1} \cdot \text{cm}^{-1}$ |
| CF_{280} | 0.01 |
| ϵ_{280} | $0.67 \text{ (mg/mL)}^{-1} \cdot \text{cm}^{-1}$ |
| $C_{recov.}$ | 1.46 mg/mL |
| MW_{IgG} | 150 kDa |
| DOL | 2.13 |

caused by uneven fluorescent illumination, the field stop was narrowed to about half the field of view and recorded intensities were averaged over the illuminated area. The limited dynamic range of the camera meant that direct comparisons of the brightest (highest density) and dimmest (lowest density) samples could not be made using the same exposure times. To overcome this issue, each slide was imaged over a range of exposure times, yielding an average intensity versus exposure time curve for each sample. Maximum exposure times were chosen so that no single pixel value was above the saturation limit of the camera and were short enough that photo-bleaching was not observed. Minimum times were chosen to ensure the average intensity was above 2% of the camera's range (300/16000). The intensity vs. exposure time curves are linear, having slopes which increase roughly linearly with solution concentration (Figure 4.1c).

4.2.2.3 Fluorescence signal of surface bound protein yields relative surface density

The absence of a “standard candle” relating fluorescence intensity to number of molecules on the surface precludes establishing a calibration curve relating solution concentration to a physical surface density. However, the calibration curve presented in Figure 4.1 does permit rescaling measured phagocytic responses to reflect the effect of surface density relative to the maximum density measured (1.5 mg/mL antiserum protein in solution). For the opsonization densities assayed here, the rescaled values are listed in Table 4.2.

4.2.3 Statistical and Numerical Analysis

Unless otherwise stated, all statistical and numerical analyses were performed in Matlab R2014a using the Statistics and Curve Fitting toolboxes.

4.3 Characteristics of Frustrated Phagocytosis

4.3.1 Frustrated phagocytosis spreading behavior

Analysis of the phagocytic spreading behavior of over 250 J774A.1 cells revealed two general populations. The first population consisted of cells which gradually attach to the surface reaching contact areas around $500 \mu m^2$ in a period of about 25 minutes. The second population contained cells which rapidly expand during FP, reaching areas as large as $2000 \mu m^2$ in 5-15 minutes. Plots of cell contact area as a function of time are shown in Figure 4.2. Of the cells which spread, two additional classes were observed. The first class consisted of a small fraction of cells (19% of all spreading cells) which spread to a maximum area and then remained relatively stationary for at least 10 minutes after spreading. In subsequent analyses, this class is termed “spreading, non-contracting” (Figure 4.2b). The second class (81% of all spreading) appear to spread for typically 5-10 minutes reaching areas comparable to those reached by the non-contracting cells; however, immediately after reaching their peak area these cell contract. Final contact areas for this class are typically 60-80% their maximum value (Figure 4.2c).

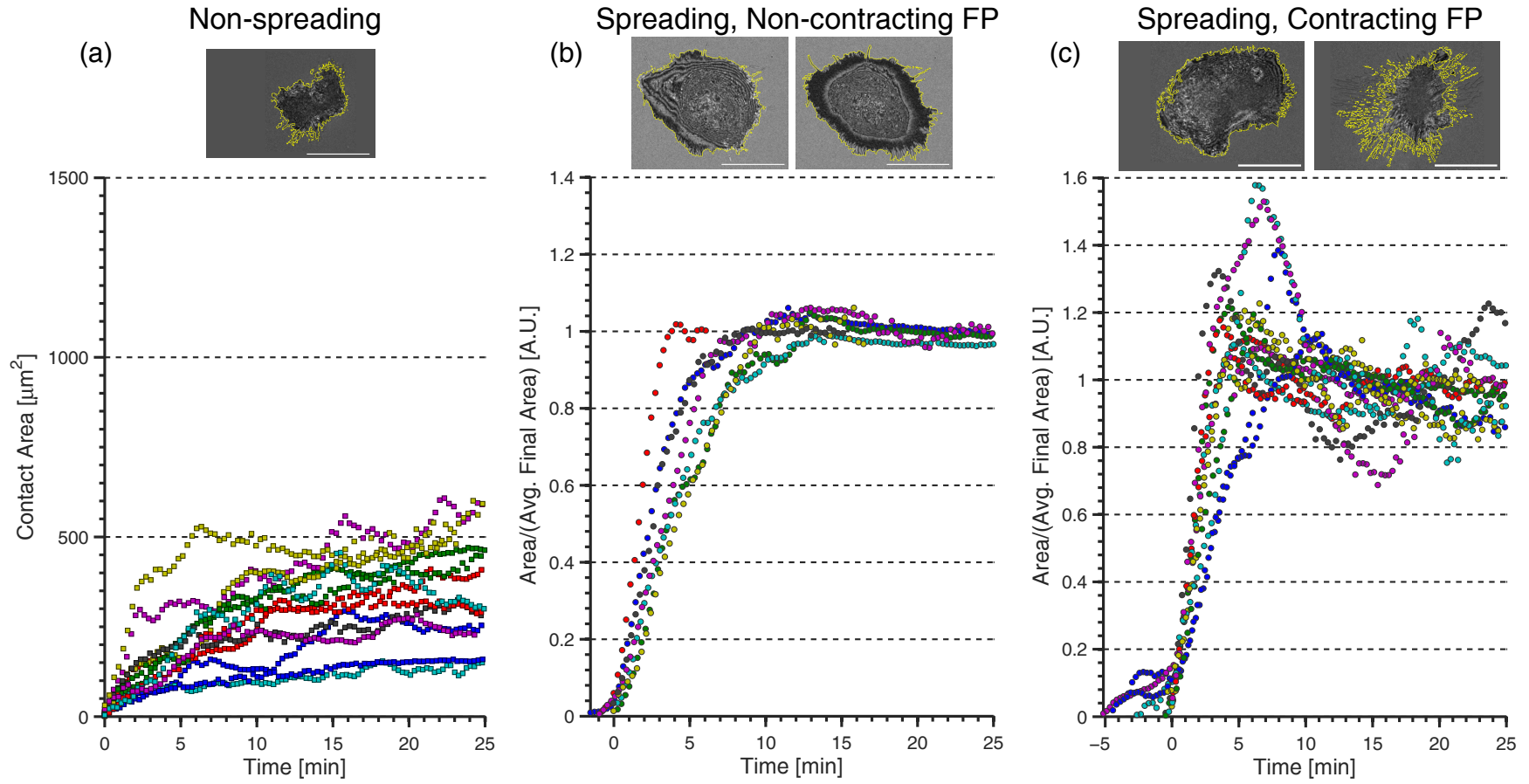


Figure 4.2: J774A.1 spreading on opsonized surfaces. Each colored time-trace depicts the spreading behavior of an individual cell. Center and right plots show time-traces rescaled by the average final contact area. Left: in all experiments a fraction of cells do not spread upon surface contact. Center: 19% of spreading cells plateau at a maximum area. Right: 81% of cells undergo contraction after reaching maximum area. Images show cells typical of each category. Scale bars represent 20 μm . Center and right image pairs show example cells at peak (left) and final (right) area. Yellow line around cell indicates contact area perimeter segmented with custom image processor.

4.3.2 Characterization of spreading fronts during frustrated phagocytosis

To facilitate our comparison of frustrated phagocytosis with spreading and migratory processes we set out to measure frustrated phagocytic protrusion rates using metrics directly comparable to those used by the migration and spreading communities. A common method used to characterize cell spreading/migration is to measure the normal velocity ($\mu\text{m}/\text{s}$) at which a lamellipodial protrusion moves. For broad, flat, lamellipodia like those present in keratocytes, this simply equates to the forward velocity of a cell's edge. For asymmetric, non-uniform, spreading fronts, defining the normal velocity can be ambiguous. In the case where a cell spreads symmetrically, with contact areas corresponding to expanding circles, the protrusion growth rate could simply be defined as the derivative of the square root of the area $v(t) \approx d\sqrt{A(t)}/dt$. Alternatively for asymmetric, but still ovular-shaped, the perimeter could be parametrized in polar coordinates relative to the initial contact point and the growth rate simply defined as the time-derivative of the radii $v(\phi, t) = \dot{R}(\phi, t)$. However, these definitions fail for non-circular cells, where a polar ray (ϕ) can intersect the cell perimeter at multiple locations and the vectors normal to a growing edge deviate significantly from radial vectors.

In light of this ambiguity, we performed our analysis using two metrics of spreading behavior. Under the first metric (which we term “protrusion rate”), growth rate was defined as the time rate of change of the location of a cell edge where it intersects a vector in the center and approximately normal to an expanding protrusion. This definition is illustrated in Figure 4.3.

The second metric (termed “protrusion activity”) employed the morphological profiling algorithm described in Chapter 3.5. Using that algorithm, we tracked local edge displacements along the cell perimeter over the entire sequence of frustrated phagocytosis. Using these displacements we calculated local protrusion and retraction rates. Protrusion rates were then assembled into a 2-D “heat-map”, where one dimension corresponds to perimeter location, the second corresponds to time (see Figure 4.5 for an example).

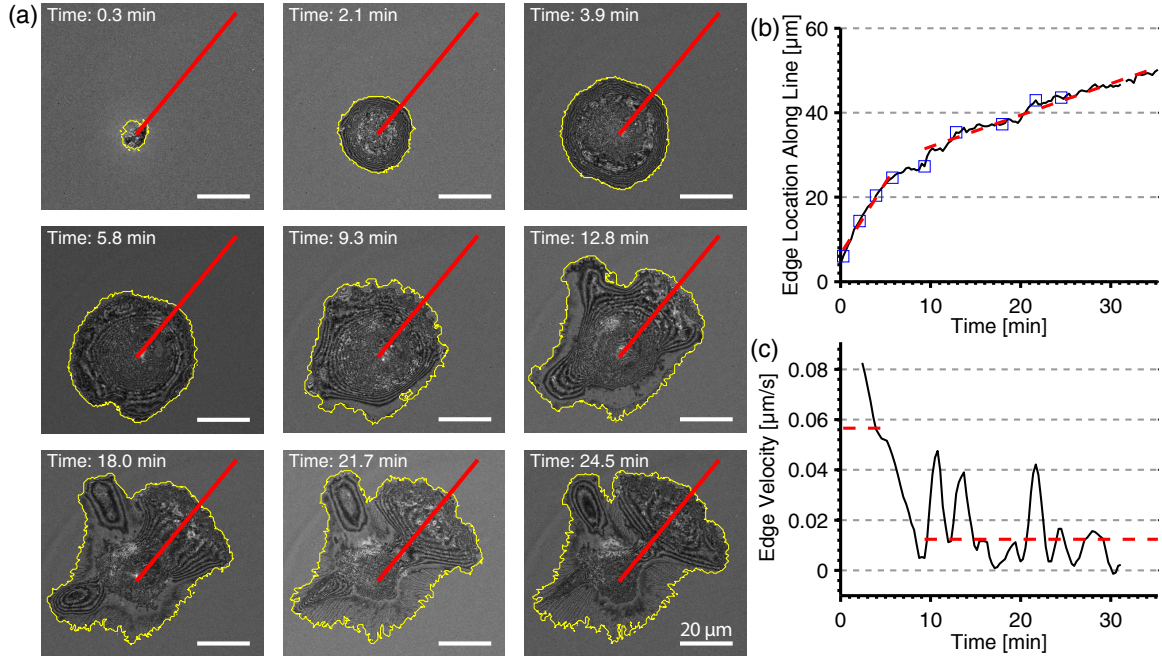


Figure 4.3: Protrusion growth rate. (a) Macrophage undergoing frustrated phagocytosis. Yellow line corresponds to the cell edge determined by our image processor. Red line indicates vector along which growth rate was defined. In early stages cell spreads symmetrically. In late stage, cell preferentially spreads towards top right. Vector was chosen to be normal to the direction of protrusion growth and centered in the middle of the approximate arc defining the expanding cell edge. (b) Intersection of cell edge with vector over time. Time-averaged spreading velocity was computed by fitting early and late stage data with two lines (red-dashed lines). The slopes of those lines correspond to the time-averaged velocity. (c) Instantaneous edge velocity. The edge velocity (black) was calculated by applying a 9-step smoothing differentiator [139]. The dashed red lines indicate the average velocity determined by the piece-wise linear fits shown in the top figure.

4.3.2.1 Protrusion rate during frustrated phagocytosis

As discussed above, protrusion rate was defined as the time rate of change of the intersection of a protruding edge with its normal-line. Through the course of our analysis normal-lines were manually chosen. The edge velocity was computed in two steps. First, the location of the edge—normal-line intersection (in the coordinates of the normal-line) was plotted as a function of time. Next, the average slope of that curve was measured during periods of expansion (Figure 4.3b). That slope as used as an estimate of the protrusion rate.

Protrusion growth rates were measured for 46 *spreading* cells.² During the initial expansion period, when contact area grows rapidly, three edge velocity profiles were measured for each cell. For circularly spreading cells, the lines were chosen to be about 60° apart and directed radially. For non-circular cells the lines were chosen to be perpendicular to, and centered, in the most predominant expanding fronts.

Spreading speeds ranged from 0.035 $\mu\text{m}/\text{s}$ to 0.150 $\mu\text{m}/\text{s}$. For most cells, the three measured speeds were in close agreement. The median difference between the highest and lowest speed measured on any given cell was 0.011 $\mu\text{m}/\text{s}$. There were, however, a few cells where speed differences were as high as 0.1 $\mu\text{m}/\text{s}$. In those cases spreading occurred asymmetrically. The median top-speed was 0.077 $\mu\text{m}/\text{s}$. Speed during the initial spreading phase did not appear to correlate with the maximum contact area. The correlation coefficient between peak area and top-speed was calculated following the methods presented in [154]. Correlation coefficient is defined as

$$r = \frac{\sum A_i \cdot V_i}{\sqrt{\sum A_i^2 \cdot \sum V_i^2}}. \quad (4.4)$$

This yielded a value $r = -0.0117$, meaning there was very little correlation. Statistical significance was tested using the F-test [154], yielding a value of $F(44, 44) = \frac{1+|r|}{1-|r|} = 1.024$ corresponding to $P = 0.47$. Meaning we failed to find a statically significant correlation between the two metrics.

²“*Spreading* cells” includes both “non-contracting” and “contracting” classification. Non-spreading cells were not included in this analysis.

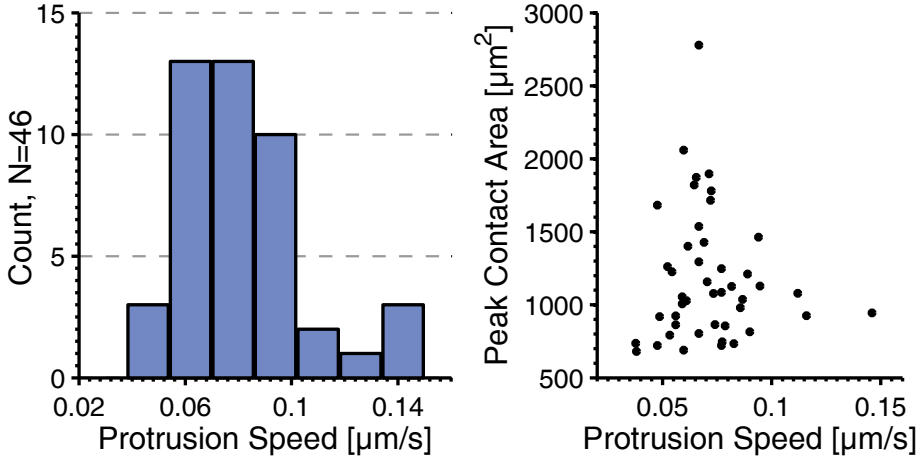


Figure 4.4: Protrusion growth rate statistics. Left: Histogram of maximum spreading speed measured during initial growth period. $N = 46$, Median Speed = $0.077 \mu\text{m}/\text{s}$. Right: Scatter plot of peak contact area vs. protrusion speed. Contact area does not appear to correlate with top-speed. Correlation coefficient $r = -0.0117$.

4.3.2.2 Protrusion and retraction activity during frustrated phagocytosis

Using the algorithm discussed in Chapter 3, we can construct activity maps for frustrated phagocytic spreading. These maps reveal three distinct phases of cell behavior. The early contact phase (P0) is relatively short-lived in FP. For most cells this phase lasts no longer than 2 minutes. During this period the cell forms small, transient contacts with the substrate, which appear as small dark patches in RICM. As the cells continue to engage the surface they undergo a period of rapid spreading (P1). Activity maps during this period reveal that local spreading rates are not constant. Rather, cells appear to spread through local bursts of high and low activity. In many cases, spreading is biased to one side, meaning that although the cells appear circular their activity maps show a propagating band of inactivity (see Figure 4.5). For both contracting and non-contracting cells, spreading (P1) is terminated by an abrupt halt in protrusion. In non-contracting cells, late-stage (P2) frustrated phagocytosis is characterized by small oscillations between spreading and contraction that occur stochastically around the perimeter of the cell.

EG

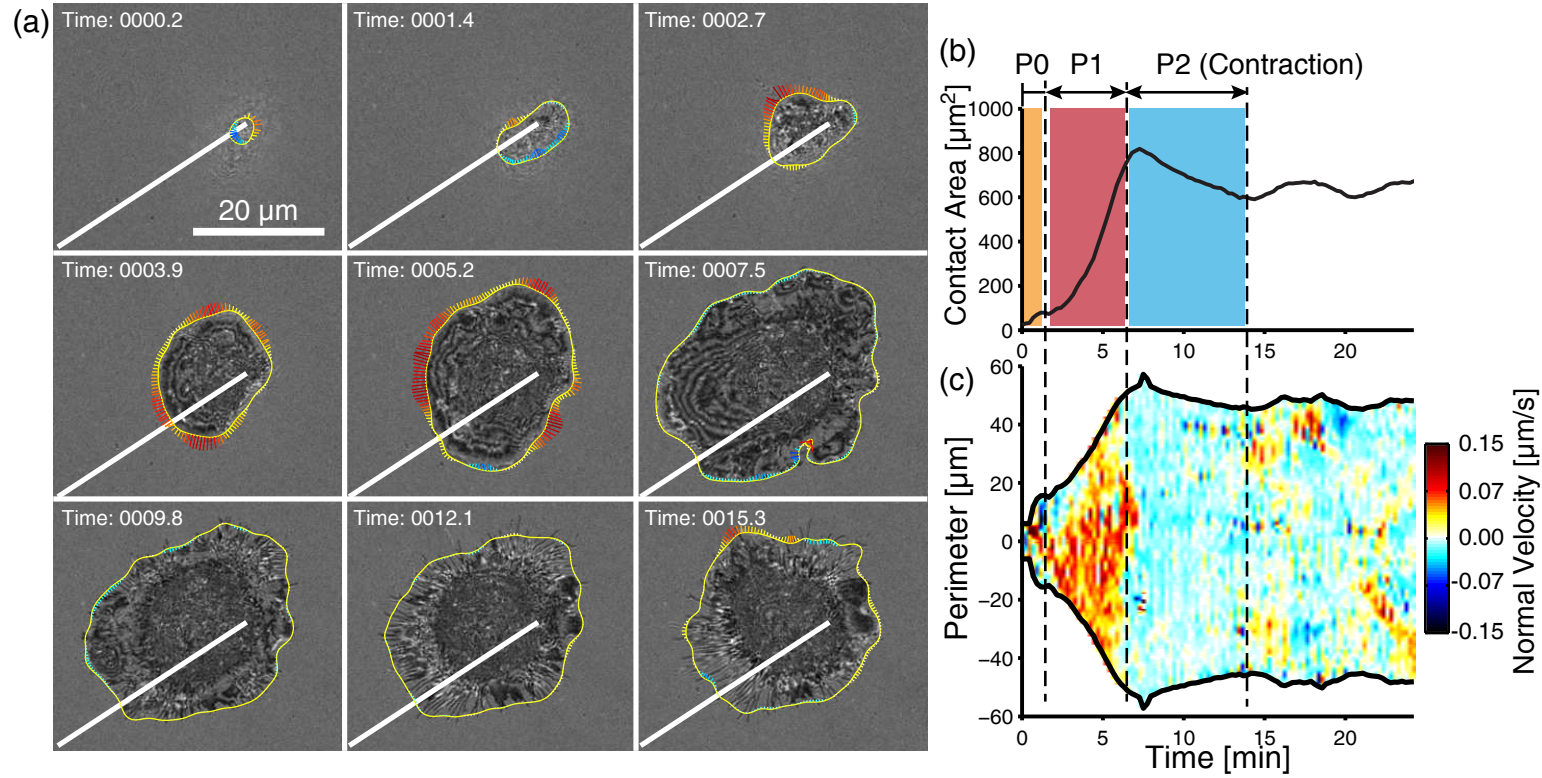


Figure 4.5: Activity map of contracting cell. Edge velocity rates are aligned to a user selected center line (white line in a), denoted by 0th position along the perimeter. Edge activity is concatenated into a time-ordered array and plotted as a heat-map (c). (a) Micrographs of cell during FP. White line indicates user-selected “0th position.” Cell perimeter, calculated by our tracking algorithm, is depicted by the yellow line. Local protrusion velocity is depicted by color-coded vectors at the perimeter. Color corresponds to scale shown in c. (b) Contact area versus time. (c) Activity map. Color indicates protrusion velocity corresponding to scale on the right. Phases of spreading are indicated by vertical lines. Region of white/blue along top edge during P1 corresponds to asymmetric region which did not spread (also seen in at right of micrographs).

μ C

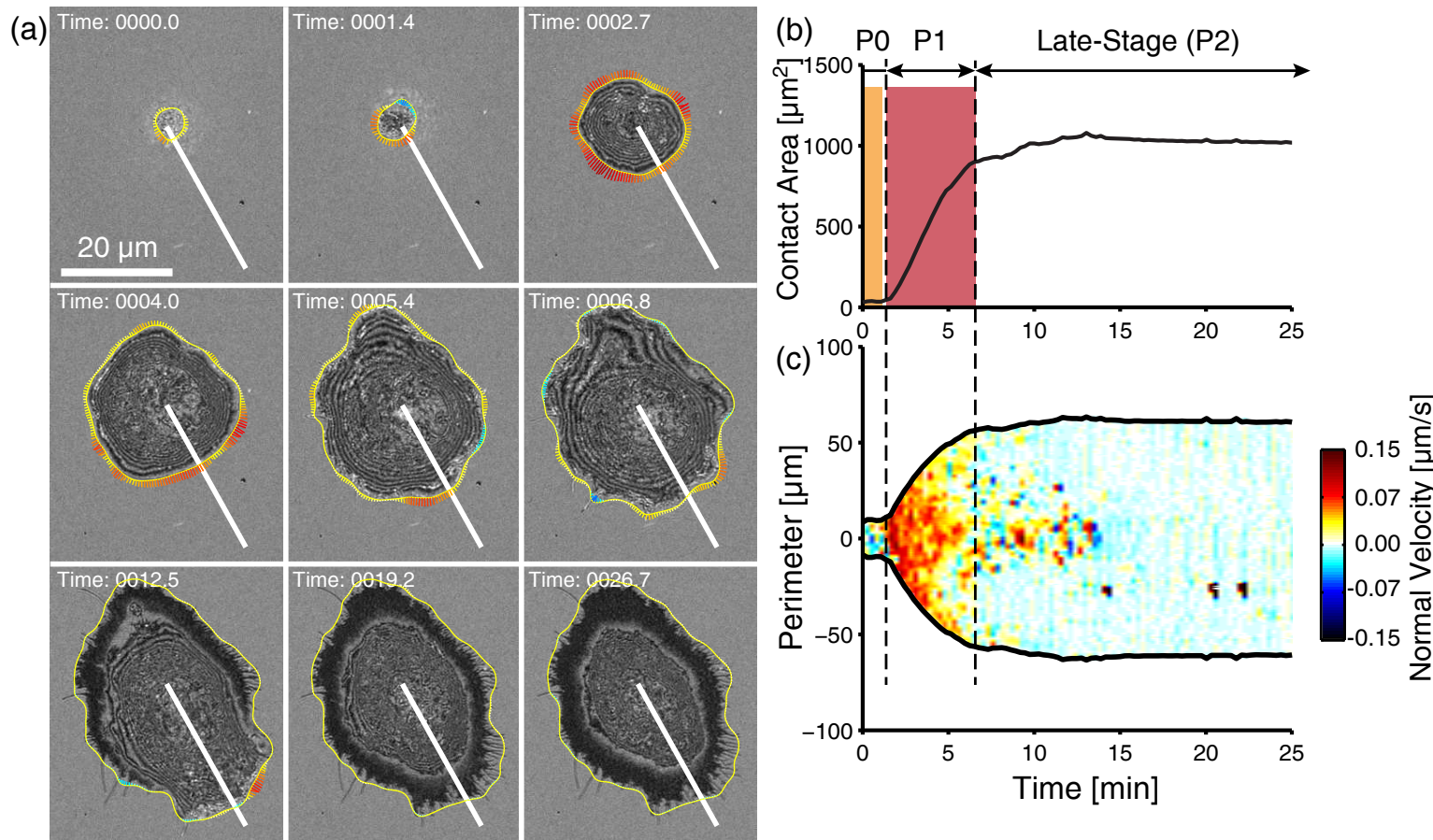


Figure 4.6: Activity map of non-contracting cell. (a) Micrographs of cell during FP. White line indicates user-selected “0th position.” Cell perimeter, calculated by our tracking algorithm, is depicted by the yellow line. Local protrusion velocity is depicted by color-coded vectors at the perimeter. Color corresponds to scale shown in c. (b) Contact area versus time. (c) Activity map. Color indicates protrusion velocity corresponding to scale on the right. Phases of spreading are indicated by vertical lines. This cell does not contract and has minimal activity during P2.

Contracting cells typically show two regimes of late stage behavior. For a period of 5-10 minutes following P1, these cells undergo a sustained contraction. During this period, activity maps typically show a vertical band of similarly shaded retraction. In Figure 4.5, this period corresponds to the blue-white band centered on the 10 minute mark. In many cases, after 20-30 minutes of contact with the substrate, both contracting and non-contracting cells enter a migratory/probing phase. During this phase cells briefly polarize, forming a lamellipodium, which results in directed motion. The life-time of these lamellipodia are relatively short (less than 5 minutes). During this cycle, cells typically do not move more than a body length before changing direction.

4.3.3 Opsonion density response

Frustrated phagocytosis spreading behavior was measured as a function of opsonization density. Surfaces of varying opsonin density were prepared by incubating BSA functionalized coverslips in 150, 15, 1.5 and 0.15 $\mu\text{g/mL}$ anti-BSA serum protein. Controls (BSA alone) were incubated in PBS. The fluorescence calibration curve (Section 4.2.2) was used to relate solution concentration to relative opsonization density. Opsonization densities were rescaled relative to the maximum solution concentration used in our experiments (150 $\mu\text{g/mL}$). Rescaled values are listed in Table 4.2.

4.3.3.1 Antibody density determines probability of spreading

The spreading behavior of a minimum of 30 cells was observed for each opsonin density (Figure 4.7). Cells were classified as “spreading” if they underwent a sustained period of expansion (see Section 4.3.1 for a thorough definition of spreading versus non-spreading). By definition, spreading cells had areas larger than the contact area associated with the cell

Table 4.2: Calibrated opsonin density.

| Solution Concentration [$\mu\text{g/mL}$] | Relative opsonin density (ρ_{IgG}) |
|---|--|
| 150 | 1 |
| 15 | 0.1335 |
| 1.5 | 0.0178 |
| 0.15 | 0.0024 |
| 0 (BSA only) | 0 |

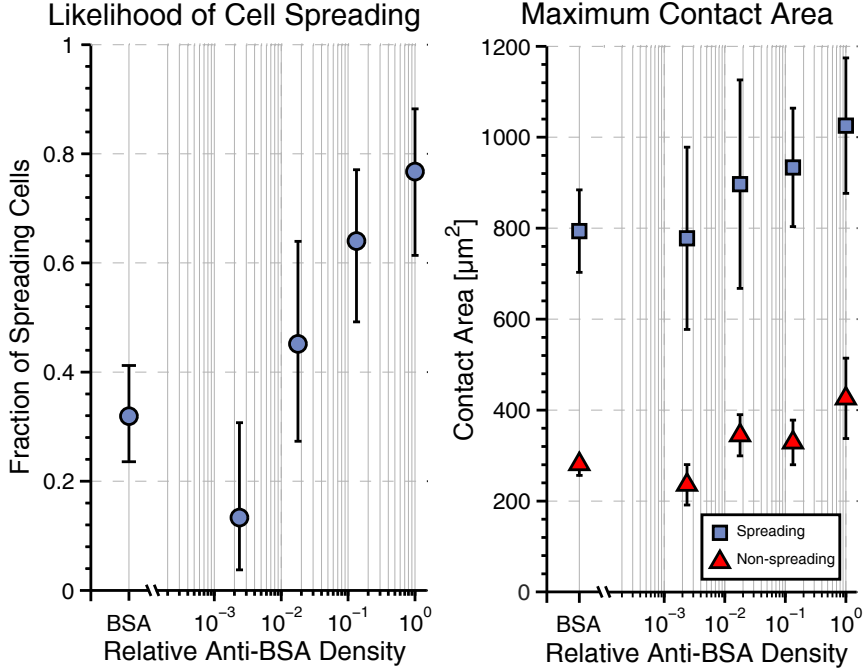


Figure 4.7: Response to opsonin density. Surfaces were opsonized in 0.15, 1.5, 15, 150 $\mu\text{g}/\text{mL}$ anti-BSA serum. Relative surface densities calculated using measured fluorescence calibration curve. In plots, 1 corresponds to 150 $\mu\text{g}/\text{mL}$. Controls (PBS only) are listed as BSA. Numbers of cells measured are listed on the histograms. A) Fraction of cells which rapidly spread. Error bars indicate 95% CI for binomial fit. B) Average peak contact areas. Blue squares correspond to spreading cells, red triangles to non-spreading cells. Error bars indicate 95% CI.

forming a hemispherical cap ($400 \mu\text{m}^2$). At the highest density measured ($\rho_{\text{IgG}} = 1$) roughly 77% of cells rapidly spread upon contact with the surface. This fraction steadily declined as opsonization density was reduced. At the lowest density $\rho_{\text{IgG}} = 0.0024$, the spreading fraction fell to 14%. Slides with only BSA elicited a spreading response in approximately 32% of cells. We hypothesize this response is due to the triggering of scavenger receptors activated by the cross-linking methods we used to functionalize the substrates [49].

4.3.3.2 Maximum contact area and spreading rates are not determined by antibody density

Peak contact area remained relatively consistent for spreading cells on all to the surfaces measured (Figure 4.7b). One-way ANOVA was performed on the maximum contact areas; the test failed to show any significant difference between the spreading populations ($F(4,115)=1.85$, $p=0.125$). The period of spreading was measured as the time between

initial contact and 95% maximum area. The metric was applied to a subset of the cells measured at each opsonization density. Cells were chosen such that their contact areas were contiguous and their Area-Time curves were monotonic during the spreading period. This stricter definition facilitated making clear measurements of the spreading time. Area-Time curves for cells fitting this definition are typified by those plotted in Figure 4.2(b,c). Similar to the contact area results, spreading time did not appear to be affected by surface density. The lowest density surface was excluded because only two of the four spreading cells fit this stricter criteria used in this analysis. ANOVA performed on the highest three densities showed very little variation between the spreading times ($F(2,55)=0.34, p=0.71$).

4.3.4 Comparison of frustrate phagocytosis with “universal” cell spreading

Traditional phagocytosis is characterized as occurring four phase: initial cell-particle contact, phagocytic cup formation, cup closure, and phagosomal internalization. Our analysis of FP reveals that each of these phases equate to identifiable shifts in cell behavior. As discussed in Chapter 2, phagocytic cup formation is powered by the polymerization of actin via a mechanism universal to many spreading and migratory behaviors. Morphologically, frustrated phagocytosis bears a striking resemblance to other cell spreading processes. Neutrophils [123], Jurkat T-Cells [82], embryonic fibroblasts [44], platelets [10], and THP-1 monocytes [102] all have been shown to spread following a characteristic sigmoidal area-time curves when presented with an appropriate ligand coated surface. It is well documented that the late-stage phosphatidylinositol based signals (PIP_2 , PIP_3) engage actin machinery universal to these cell types [16]. Therefore, it is not surprising that frustrated phagocytosis spreading rates are those exhibited by non-phagocytic cells.

4.3.4.1 Universal Spreading Behavior

The most detailed and comprehensive studies of “universal” (non-phagocytic) cell spreading have been conducted by Sheetz and co-workers [42, 45, 44, 55, 110, 56, 58, 27, 43, 26]. Their work focuses on the dynamics of mouse embryonic fibroblast spreading on fibronectin coated substrates. Although their reports specifically document fibroblasts specifically, experiments

using other cell types (HeLa, Neutrophils, T-cells, Epithelial cells, and *Dictyostelium discoideum*) reveal that spreading behaviors exhibited by fibroblasts are common to many eukaryotic cells [36, 123, 82, 30, 145]. This has led some to label this behavior as “universal” spreading [36].

Similar to the phases of phagocytosis, their experiments have demonstrated that “universal” spreading occurs in distinct phases [42, 45, 44]. Like phagocytosis, “universal” spreading begins with an attachment phase (P0) which typically lasts a few minutes. During this phase cell-substrate contact area grows at a slow rate. Following attachment, the cell enters a phase of rapid expansion (P1). During this phase ARP2/3 mediated actin polymerization drive the cell symmetrically outward. As cells expand, contact area grows roughly linearly with time [36, 30, 29].

The final phase (P2) is characterized by a steady “roll-off” in spreading rates [30] and a transition to migratory behavior [42]. Unlike phagocytosis, “universally” spreading cells do not undergo a period of sustained contraction. Instead, “universal” P2-spreading is characterized by bursts of protrusion and retraction [44].

Similar to the methods discussed in Section 4.3.2.2, activity maps have been used to characterize the phases of “universal” spreading. Like the phases of FP, activity maps of “universal” spreading reveal distinct transitions between each phase of behavior. Activity during initial (P0) and spreading (P1) phases are very similar for both FP and “universal” spreading. However, protrusion activity during the final (P2) phase appears to be cell type specific. Not only is P2 activity distinct for phagocytes, non-phagocytic cell types also exhibit diverse protrusion activity.

Four classes of P2 protrusion activity have been reported. In fibroblasts, P2 protrusion activity occurs in local bursts which travel along the perimeter of the cell [45, 88]. In keratocytes, known for their broad lamellipodia and highly directed migration, P2 protrusion activity is constant across the entire leading edge of the cell [88]. In newt lung epithelial (NEL) cells, P2-spreading occurs through coordinated protrusion bursts. Activity maps of this type show periodic bands of protrusion and retraction [88]. The activity of Ptk1 epithelial cells constitutes the forth class. Under this class, multiple protrusive fronts form at

the cell edge. These fronts counter-propagate along the perimeter, yielding activity maps with a cross-hatched pattern.

In light of these reports, FP behaviors (contracting and non-contracting) appear to constitute a two additional classes of late-stage (P2) spreading. Late-stage contraction appears to be unique to frustrated phagocytosis. Contraction has not been reported for other cell types. Similarly, the P2 activity of non-contracting phagocytes is also unique. As illustrated in Figure 4.6, late-stage protrusion activity is minimal and does not appear to be coordinated either spatially or temporally.

4.4 Conclusion

In this chapter we set out to quantitatively characterize the behavior of macrophages undergoing frustrated phagocytosis (FP). Employing the microscopy techniques and automated image processing algorithms discussed in Chapter 3, we assessed the FP behavior of over 250 cells. This large sample size enabled us to produce accurate statistics regarding FP response and morphology. Our analysis revealed that FP is a biphasic process. Cells either undergo rapid spreading, reaching contact areas as large as $2000 \mu m^2$ in as little as 5 minutes, or they remain inactive, passively settling onto the surface over a period of 20-30 minutes.

Using calibrated measurement of IgG opsonization density, we show that the likelihood a cell exhibits a spreading response varies logarithmically with opsonin density. Furthermore, we show that opsonin density does not affect spreading rate or maximum contact area.

Our analysis of dynamic spreading behavior demonstrates that (compared to non-phagocytic spreading) FP includes a unique period of late-stage contraction. Unlike the bursts of protrusion and retraction observed during “universal” spreading, late-stage FP contraction is coordinated across the entire cell and lasts between 5 and 10 minutes. Contrary to reports which claim that phagosomal closure is dependent on particle curvature [31, 32], our results demonstrate that phagocytes have a contractile response while phagocytosing flat surfaces.

CHAPTER V

CONTRACTION FORCE AND ACTIN CYTOSKELETAL STRUCTURE DURING FRUSTRATED PHAGOCYTOSIS

5.1 *Introduction*

It is well established that phagocytic cup formation is dependent on the polymerization of actin at the cell-particle interface [61]. It has also been shown that ARP2/3 is recruited to phagosomes during early stages of phagocytosis [90]. Based on these findings, standard discussions of phagocytic cup formation often describe actin network architecture as a hemispherical analog of the dense, highly branched, actin network associated with lamellipodial protrusions [91, 131]. Unlike lamellipodia, which are confined to a plane and therefore compatible with traditional imaging techniques, phagocytic cups are inherently 3-dimensional¹. Because of this 3-dimensionality and the relatively small size of the cups, technical challenges prevent molecular resolution imaging of actin architecture. Consequently, the network structure within phagocytic cups has yet to be verified. Furthermore, phagosomal closure has been shown to entail a pronounced period of particle directed contraction [134]. Live-cell fluorescent imaging during this period reveals actin accumulates at the constriction point, leading to supposition that actin organizes into a contractile belt during late stage phagocytosis².

These two models of actin architecture are at odds with each other. Under the lamellipodial model actin is directed normal to the propagating edge. In contrast, the contractile belt model dictates that during phagosome closure actin is bundled into an azimuthal band that runs parallel to the cell edge. These models predict F-actin alignment orthogonal to each other. If both are correct, F-actin filaments must rotate during the transition between cup formation and closure. The mechanism responsible for this reorientation remains unknown.

¹See chapter BG.XX for a discussion of lamellipodial architecture and example images

²See Chapter 2.3.1 for an overview of the contractile belt model

In this chapter, we build upon our investigation of frustrated phagocytosis (FP) presented in the previous chapter. Unlike traditional phagocytosis assays, FP confines phagocytic activity to a plane. This geometry facilitates the use of traditional microscopy techniques. In Chapter 4, we showed that FP spreading is divided into three phases (P0: initial contact, P1: symmetric spreading, P2: contraction). The experiments presented here examine phagocytic behavior during the transition from spreading to contraction, P1 to P2. As a preliminary to these experiments we develop fixation and staining protocols which maintain actin filament structure and minimize staining of background proteins and globular actin. This protocol, combined with Structured Illumination Microscopy (SIM), enables us to distinguish differences between branched and bundled actin networks. Using these methods we investigate changes in the actin network as cells progress through the phases of FP. We also use Traction Force Microscopy (TFM) to verify that late stage FP contraction is an active process, consistent with the contractile belt model. We compare the results of these experiments with established models of lamellipodia formation. Our analyses reveal a mechanism which may explain how F-actin reorients during the transition from cup formation to phagosomal closure.

5.2 *Experimental Methods*

The experiments presented here primarily build upon the frustrated phagocytosis assay developed in Chapter 3 and Chapter 4. For a detailed explanation of the protocols used consult Chapter 3.

5.2.1 **Traction Force Microscopy**

For traditional phagocytosis, uptake of soft particles results in particle deformation during late stage contraction (see chapter 2.3.1). In addition to imaging the actin network architecture during FP we also use Traction Force Microscopy (TFM) to measure the contractile stress generated by the cell. As the cell undergoes FP it exerts forces on the underlying substrate. Building the substrate out of an elastic material enables us to observe deformations imposed by cellular forces. Based on these deformations, traction field can be calculated using the methods outline by Butler and del Alamo [25, 38]. (These calculations and their

implementation are discussed in Chapter 3.7)

As discussed in Chapter 3.7, elastic substrates were made using a multilayer process. Elastic substrates with embedded fluorescent fiducial markers were prepared to have a Young's modulus of 3 kPa and a Poisson ratio of 0.3 as detailed in Chapter 3.7. The substrates were functionalized with BSA following the protocols described in Aratyn-Schaus *et al.* [6], and functionalized with anti-BSA as described in Chapter 3.7. Deformation fields were measured using combination of PIV and PTV tracking algorithms (see 3.7). Traction stress fields were calculated using Fourier Transform Traction Cytometry (FTTC) and described in 3.7.

5.2.2 Structured Illumination imaging of actin structure

In the experiments presented here, actin structure is visualized by super-resolution fluorescence microscopy. Previously published fluorescent images of actin in active phagocytes have lacked the clarity necessary to accurately assess whether F-actin bundles into a ring-like structure during phagosome closure or simply remains in an interwoven network consistent with ARP2/3 induced branching. These reports have typically used wide-field and confocal microscopy method to image the cytoskeleton. Both techniques lack the resolution necessary to distinguish subtle differences in these two contrasting structures. In this work we use Structured Illumination Microscopy (SIM) to increase the lateral resolution of our images.

SIM imaging doubles the lateral resolution set by the diffraction limit. The conceptual underpinnings of SIM leverage the fact that fluorescent samples imaged using Moiré illumination carry additional structural information that can be reconstructed using phase-space analysis [63]. A thorough discussion of SIM is presented in Chapter 3.6.

5.2.2.1 Sample Preparation

Microscope coverslips were functionalized with BSA and opsonized with 1mg/mL anti-BSA serum protein in PBS following the protocols developed in Chapter 3.1. Because cells in these experiments were to be imaged at fixed time points (as opposed to the dynamic movies discussed in chapter FP), it was imperative that we had a reference time determining how

long a cell had been in contact with the surface. In order to achieve synchronization, temperature methods were employed [135, 150, 92]. Frustrated phagocytosis was synchronized by first cooling the suspended cells and coverslips to 4 °C. Next, cells were pipetted onto the chilled coverslip and quickly warmed by transferring the coverslip to a dish mounted on a hotplate set to 37 °C. The samples were then covered with pre-warmed DMEM (with HEPES), at which point the cells began to spread. Synchronization was verified by periodic inspection with an inverted bright-field microscope. Once spreading had initiated, a stopwatch was started. Cells were allowed to spread for 5, 10, 15, and 20 minutes. Spreading was halted by gently submerging samples into ice cold HBSS for 1 minutes, after which they were fixed and stained.

5.2.2.2 Fluorescent Staining

The actin cytoskeleton and nucleus were labeled with Alexa-488-phalloidin (Invitrogen: A12379) and DAPI, respectively. Initial attempts to label F-actin following the standard phalloidin protocol yielded samples with inconsistent labeling and very little observable structure (even under SIM imaging). Improved results were achieved by employing a cytoskeletal stabilizing buffer (PEM) [144]. PEM was prepared by dissolving 100 mM PIPES (Sigma: P6757), 5 mM EGTA (Sigma: E3889), and 2 mM MgCl₂ in 500 mL of H₂O. It should be noted that PIPES does not readily dissolve in unbuffered water. Dissolution was achieved by stirring and slowly adding 10 N NaOH to the mixture. After the PIPES dissolved, pH was adjusted to 6.8.

Although phalloidin preferentially binds to F-actin, it has been shown to also bind G-actin, with a lower affinity [144]. To minimize unintended labeling, cells were permeabilized and fixed simultaneously. The fixation/permeabilization buffer consisted of PEM with 4% formaldehyde (methanol free, Thermo: 28906) and 0.2% Triton-X100 (Sigma: T8787). After being chilled in cold HBSS, samples were soaked in the fixation buffer for 10 minutes at room temperature. Samples were then rinsed and soaked in 1mg/mL BSA (in PBS) blocking buffer for 5 minutes. Actin was stained by incubating samples in 0.6 μM phalloidin in 1 mg/mL BSA buffer for 40 minutes at room temperature. After labeling, samples were washed with

DI-H₂O and gently dried with N₂. Coverslips were mounted on glass slides using Prolong Diamond, which included DAPI for labeling the nucleus (Life Technologies: P36971).

5.3 Results

5.3.1 Cells exert contractile traction force during late stage contraction

Although myosin activity has been associated with phagosomal closure [40, 133], it is unclear whether contraction during late-stage FP is the result of an active (myosin motor driven) process, or simply a consequence of F-actin depolymerization [98]. Lamellipodial protrusions are supported by ARP2/3 branched actin (see Chapter 2.2.3). As lamellipodial F-actin depolymerizes, membrane cortical tension is sufficient to cause outstretched protrusions to recess, giving the appearance of contraction, even in the absence of motor activity [75].

During FP, the cell membrane often becomes locally pinned to the substrate. During contraction, this pinning results in the formation of membrane retraction tethers. Fluorescent staining within these tethers reveals F-actin bundles consistent with structures observed in the proximity of focal adhesions (formed in adherent and migratory cells) [86]. If late stage contraction is, in fact, a result of motor activity, cells would impose forces to the underlying substrate via the F-actin filaments within these tethers. However, if contraction is simply the result of cortical tension relaxation, forces imposed on the substrate will only arise due to stress buildup within the membrane. Methods for estimates of membrane tether force are discussed in Appendix B. Experiments using cells similar to the J774A.1 macrophages used here have shown that individual tethers, pulled using optical traps, exert forces on the order of 10-50 pN [41, 55, 69].

5.3.1.1 *Estimation of traction forces in the absence of motor activity*

We measured forces generated during FP using Traction Force Microscopy following the methods outlined in Chapter 3.7. Under the scenario where contraction is not motor driven, the force arising from a single tether can be estimated using

$$f = 2\pi\sqrt{2K_b\gamma}, \quad (5.1)$$

where γ is the cortical tension, which depends on cell surface area (see Chapter 7), and K_b is the membrane bending modulus (see Appendix B). For cells $K_b \approx 10^{-19} \text{ Nm}$ [41]. Using reported cortical tension measurements (see Table 7.1) we can estimate the force from an individual tether to be on the order of $f = 50 \text{ pN}$. The resolution of our TFM system is limited to determining the stress-field down to a grid defined by $\Delta x_{TFM} = 2.15 \mu\text{m}$. At this resolution, we can expect each grid point to sense the force of 1-3 tethers. Dividing the total estimated tether force by the area of each TFM grid point we estimate the strain one would expect to measure

$$\sigma_{tether} \approx \frac{3f}{\Delta x_{TFM}^2} = 30 \text{ Pa.} \quad (5.2)$$

As a point of reference, stress measured during cell migration is on the order of $100 - 400 \text{ Pa}$ [136, 2, 25, 39].

5.3.1.2 Traction force peaks during late-stage FP, magnitudes consistent with motor driven contraction

Live-cell TFM experiments were conducted following the protocols described in Chapter 3.1, and 3.7. Occlusions caused by the fiducial particles prevented the use of automatic cell tracking algorithms. Therefore, contact-area curves were measured manually. The results of one such experiment are presented in Figures 5.1 and 5.2. Traction force activity was parametrized using two metrics: strain-energy and principle traction moments [25, 121, 116, 136]. Strain energy is calculated as

$$U = \frac{1}{2} \int \vec{T}(\vec{r}) \cdot \vec{u}(\vec{r}) dx dy, \quad (5.3)$$

where \vec{T} is the calculated traction stress field, and \vec{u} is the measured displacement field.

As can be seen in Figure 5.1, traction forces remain low during the initial spreading phase, but rapidly increase during the onset of contraction. Near the 14 minute mark, traction activity peaks. A map of traction stress magnitude is shown in Figure 5.2. Traction stress is mostly confined to the cell perimeter. Typical stress magnitudes during the contractile period were measured to be in the $100-200 \text{ Pa}$ range. These values are consistent with stresses measured during migration [136, 2, 25, 39] and almost an order of magnitude greater than those estimated for passive cortical tension driven contraction (see eq 5.1).

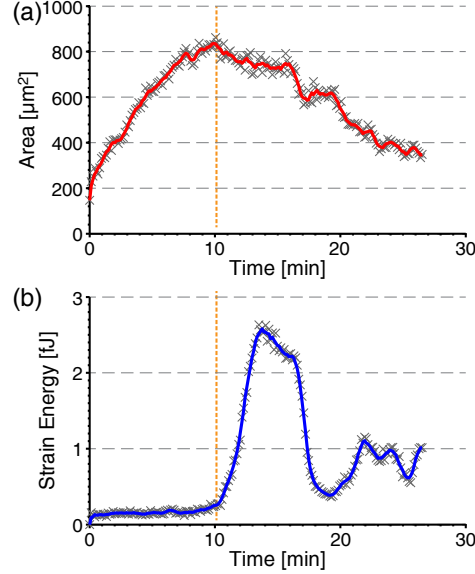


Figure 5.1: Strain Energy. (a) Approximate contact-area versus time. Cell perimeter was identified manually. Red line indicates 5-point moving average. (b) Strain energy, calculated as indicated. Blue line indicates 5-point moving average. Strain energy peaks during contraction stage. Very little stress is imposed during P1 spreading (0-10 min).

First order traction moments were calculated as

$$M_{ij} = \frac{1}{2} \int dx dy [x_i T_j(\vec{r}) + x_j T_i(\vec{r})]. \quad (5.4)$$

The matrix was then diagonalized:

$$\begin{bmatrix} \lambda_{x'} & 0 \\ 0 & \lambda_{y'} \end{bmatrix} = \mathbf{V}^{-1} \mathbf{M} \mathbf{V}, \quad (5.5)$$

yielding eigenvalues $\lambda_{x',y'}$ which indicate the total dilation/contraction along the principle axes defined by the eigenvectors (\mathbf{V}). $\lambda_i > 0$ indicate stress-fields which dilate the substrate; $\lambda_i < 0$ indicate contraction. Traction moments are plotted in Figure 5.2. During the contractile period both moments are negative, meaning the cell is contracting in both principle directions. After 20 minutes, the micrographs show that the cell has begun to polarize. A lamellipodium appeared on the right side of the cell. During this period the dominant contractile moment is aligned perpendicular to the direction of the extending lamellipodium. This is opposite what has been reported for migrating *Dictyostelium discoideum*, which move parallel to the dominant axis[136].

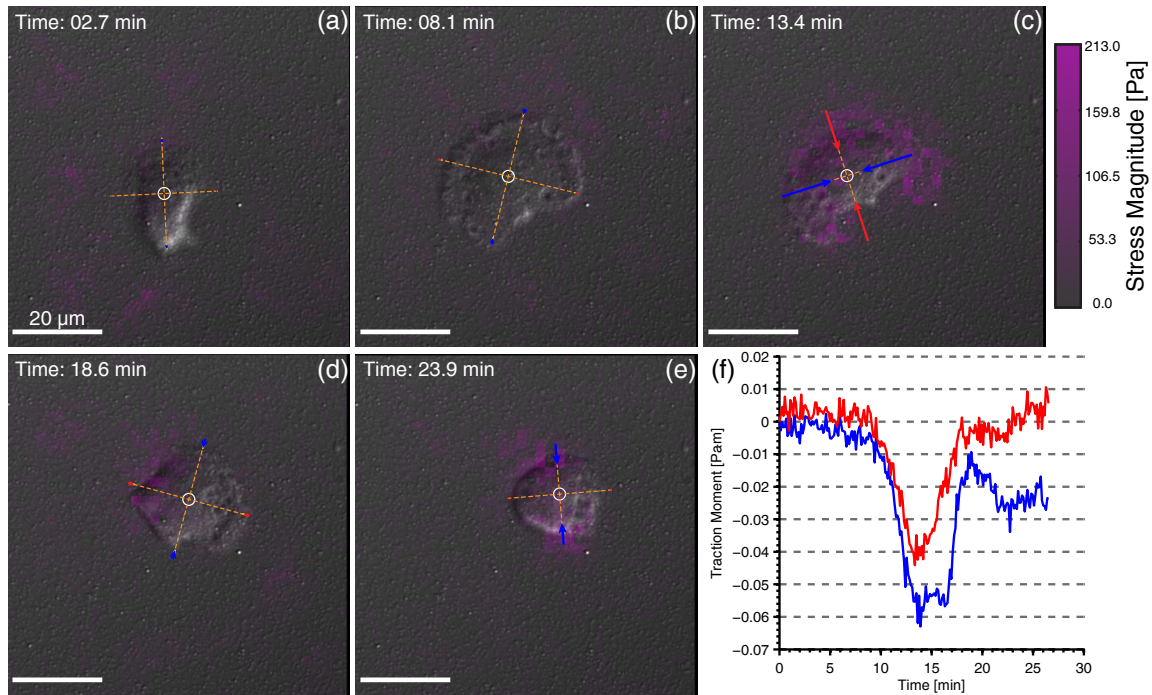


Figure 5.2: Traction force microscopy with traction force moments. J774A.1 macrophage undergoing frustrated phagocytosis on traction force microscopy substrate. Stress magnitudes are indicated by magenta overlay. Magnitudes correspond to the colorscale indicated on the right. Traction force moments are indicated by the red and blue vectors oriented along the principle axes (orange lines). Values of the contractile moments are plotted in the time-trace (lower right). Contractile moments are calculated following eq 5.4. Principle axes correspond to the eigenvectors defined in eq 5.5.

5.3.2 Simultaneous fixation and permeabilization is necessary to preserve actin structure

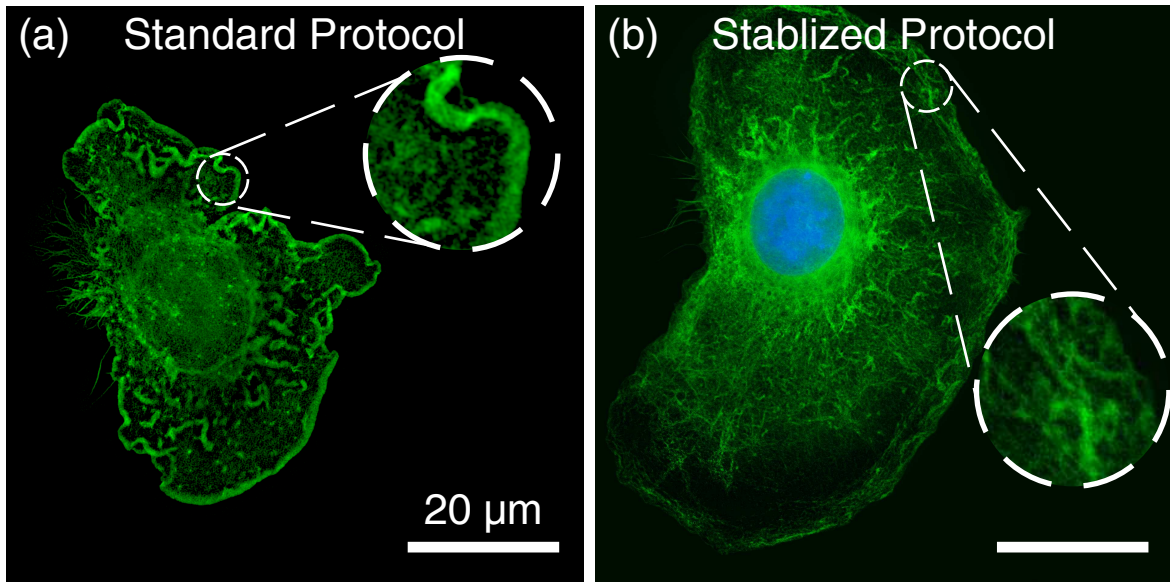


Figure 5.3: Comparison of staining methods. (a) Cell fixed using standard fixation protocol. Phalloidin (green) labels areas of high actin density but does not preserve fibrous appearance of actin network. (b) Cell fixed and permeabilized in cytoskeletal stabilization buffer. Phalloidin (green) appears to preserve network structure, note the fibrous striations throughout the cell. Nucleus labeled in blue via DAPI.

Our initial attempts to label F-actin using the manufacturer prescribed protocol yielded poor results. Standard immunostaining protocols, including those typically published for phalloidin staining, often involve first fixing cells using a cross-linking reagent (usually formaldehyde). After fixation, cell membranes are permeabilized using a detergent; this allows staining compounds to enter cellular compartments and stain structures of interest. Following this general strategy failed to produce cells with distinguishable actin structure. Instead, fluorescent phalloidin typically appeared as bright bands in areas typically associated with high actin densities, like membrane ruffles, but did not clearly label bundled actin filaments. Also, following this generic protocol resulted in the presence of numerous punctate structures scattered throughout the cell bodies. These small globular structures were more consistent with staining protein aggregates than F-actin fibers.

The key to preserving F-actin structure during staining proved to be the simultaneous fixation and permeabilization of the cells in a cytoskeletal stabilization buffer [144]. Under

this revised protocol, cells were fixed and permeabilized at the same time, allowing unbound monomeric actin to diffuse out of the cell before becoming cross-linked to assembled protein structures. The resulting images had remarkable clarity. Following the updated protocol, regions which originally appeared as dark patches instead showed an extensive network of inter-penetrating fibers. There was also a noticeable decrease in the number of bright puncta, suggesting the bright spots observed were indeed artifacts of the standard fixation process.

5.3.3 Actin network undergoes structural changes during spreading, contraction and migration phases

To investigate how F-actin reorganizes during the course of phagocytosis, cells were allowed to undergo frustrated phagocytosis for a pre-determined period of time after which they were placed into a 4 °C ice bath to slow their metabolic activity and halt their motion. Shortly thereafter, they were fixed and stained following the protocol discussed above. Cells were allowed to spread for 5, 10, 15 and 20 minutes. These time points were chosen based on behaviors observed during live-cell experiments (see Chapter 4). As illustrated in normalized spreading curves presented in Figure 4.2c, within the first 10 minutes of FP, cells undergo rapid, isotropic expansion. At around 10 minutes cells exhibit a behavioral shift. Over the subsequent 10 minutes cells typically contract. After contraction (20+ minutes), cells often enter a migratory phase characterized by directed motion and the presence of a lamellipodium polarized in that direction. Representative SIM images of cells from each time point are depicted in Figures 5.5-5.8. These images can be compared with a time-sequence of a single cell undergoing frustrated phagocytosis photographed via bright-field DIC microscopy (Figure 5.4).

5.3.3.1 Actin forms dense zone at leading edges during spreading phase (5 min)

After 5 minutes of FP activity, actin appears as a dense zone surrounding the perimeter of the cell. During early phagocytosis, the actin network appears to be relatively unstructured. Sparse filamentation can be seen throughout the body of the cell but not at the expanding edge. Based on the existing ARP2/3 mediate model of phagocytic cup formation, we hypothesize that the dense region seen at the edge is a fluorescent analog of the highly

branched structure present at the leading edge of migrating cells (cryo-EM images shown in Figure 2.4 illustrate this structure).

5.3.3.2 Transition from spreading to contraction is accompanied by a change in actin structure (10 min)

After 5-10 minutes, phagocytosing cells appear to undergo a shift in behavior. As shown in the 7:21 and 9:52 minute marks of Figure 5.4, the early stage of smooth symmetric spreading is punctuated by ruffling at the cell edge. For the majority of cells this is followed by a period of contraction (see chapter 4 for a full discussion of FP behavior). The fluorescent images also reflect a distinct shift in behavior. As shown in Figure 5.5, the dense zone of actin associated with the expanding edge visible at 5 minutes is markedly absent. In Figure 5.6a, bundled filaments can be seen throughout the cell. These filaments do not strictly align in a single direction but striation generally appears to be radial. The cell in Figure 5.6b is beginning to show signs of contraction. Retraction tethers are present on the upper left side. Notice that, in contrast to cells at 5 minute, banding at the perimeter appears to contain striations which run parallel to the edge.

5.3.3.3 Actin rich tethers indicate direction of contraction (15, 20 min)

As discussed in section 5.3.1, contracting cells leave behind thin membrane retraction tethers. Similar structures are often observed at the trailing edge of migrating cells. As late-stage FP progresses and cells continue to contract these tethers become more apparent. In Figure 5.7, retraction tethers surround the cell. These tethers directly indicate which regions of the perimeter were contracting prior to fixation. Similar tethers can be seen in cell shown in Figure 5.8, although in that case contraction is confined to one side. Based on the characteristic “D” shape, the cell appears to be migrating to the right.

5.3.3.4 Actin bundles parallel to contracting edges (15, 20 min)

The most striking feature of phalloidin-labeled late-stage cells (Figures 5.7,5.8) is the intense, highly striated, banding that runs parallel to contracting edges. This banding indicates that F-actin is bundled into long fibers. The intensity of these fibers appears to correlate with the presence of retraction tethers, suggesting bundling occurs concurrently with contraction.

5.3.3.5 Subtle morphological differences between macrophages and other cell types during migration (20+ min)

After the contraction stage, macrophages typically enter into a migratory phase. This phase is characterized by the polarization of the cell. A new lamellipodium forms at the leading edge and retraction tethers persist at the trailing edge. This morphology is depicted in Figure 5.4 at minute mark 19:50. As discussed above, actin bundles into parallel fibers at the trailing edge (Figure 5.8a). Near the leading edge, where the cell forms a lamellipodial protrusion, F-actin appears to be arranged in two different regions. At the leading edge of the lamellipodium striations are absent, suggesting the F-actin in this region is similar in structure to that observed at the leading edges of P1-stage cells. Behind this zone, F-actin appears to be bundled (similar to what is observed during contraction). Without dynamic live-cell sequences it is impossible to determine whether this structure is the remnant of the previous contraction phase, or inherent to the lamellipodial architecture of migrating macrophages. Studies of migrating keratocytes have revealed similar fibrous bands running parallel to out-stretched lamellipodia; however, in those cells the leading zone is significantly wider, constituting the majority of the cell area (see Figure 2.4).

Note: Figures 5.4, 5.5, 5.6, 5.7, and 5.8 are shown in the high-color prints included in the subsequent pages.

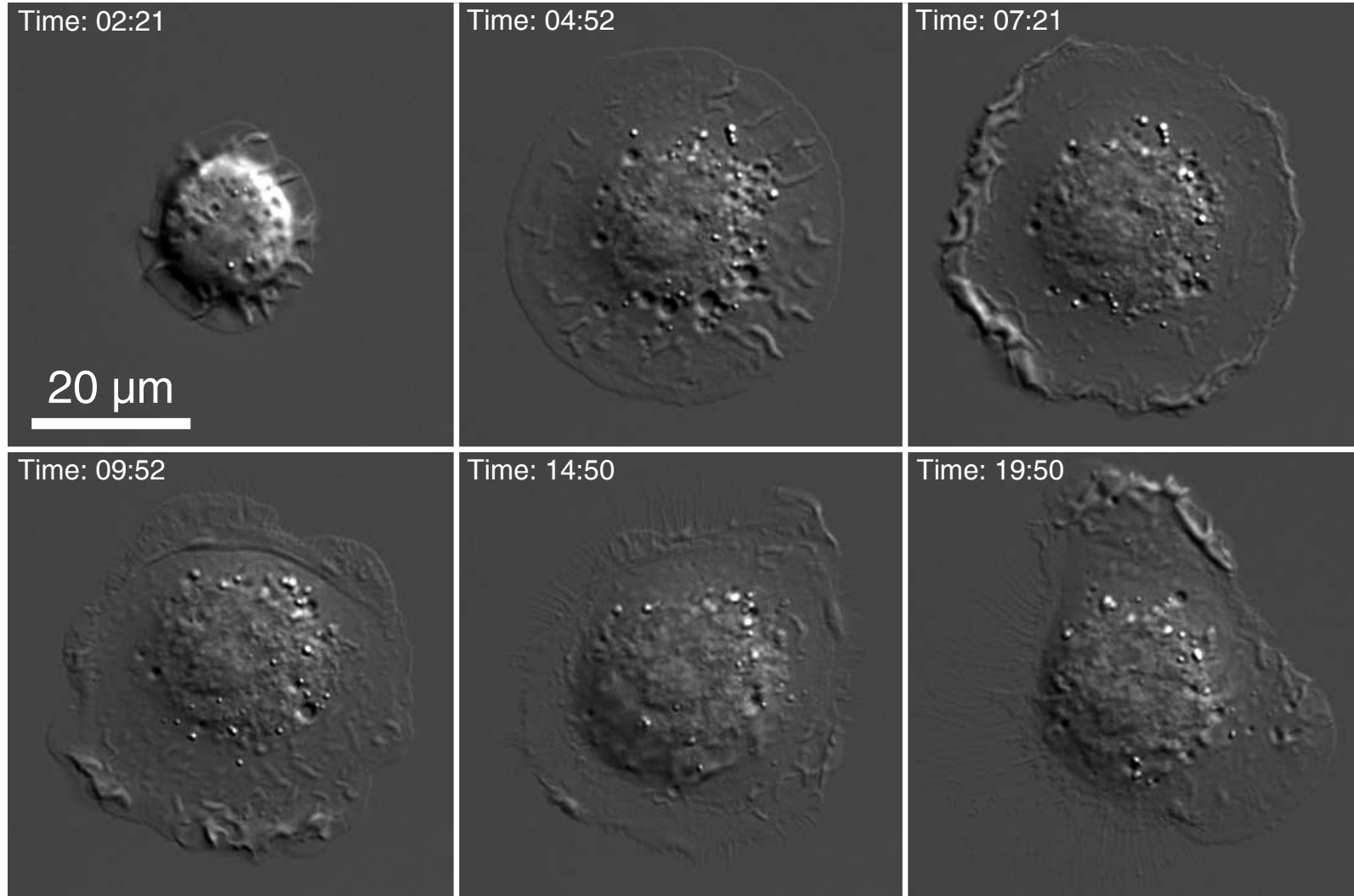


Figure 5.4: J774A.1 Macrophage undergoing frustrated phagocytosis. Time sequence of a typical macrophage undergoing FP. Cell demonstrates all three characteristic behaviors: P1 uniform spreading (2-7 min), P2 contraction (9-14 min), and directed migration (19:50 min).

ε2

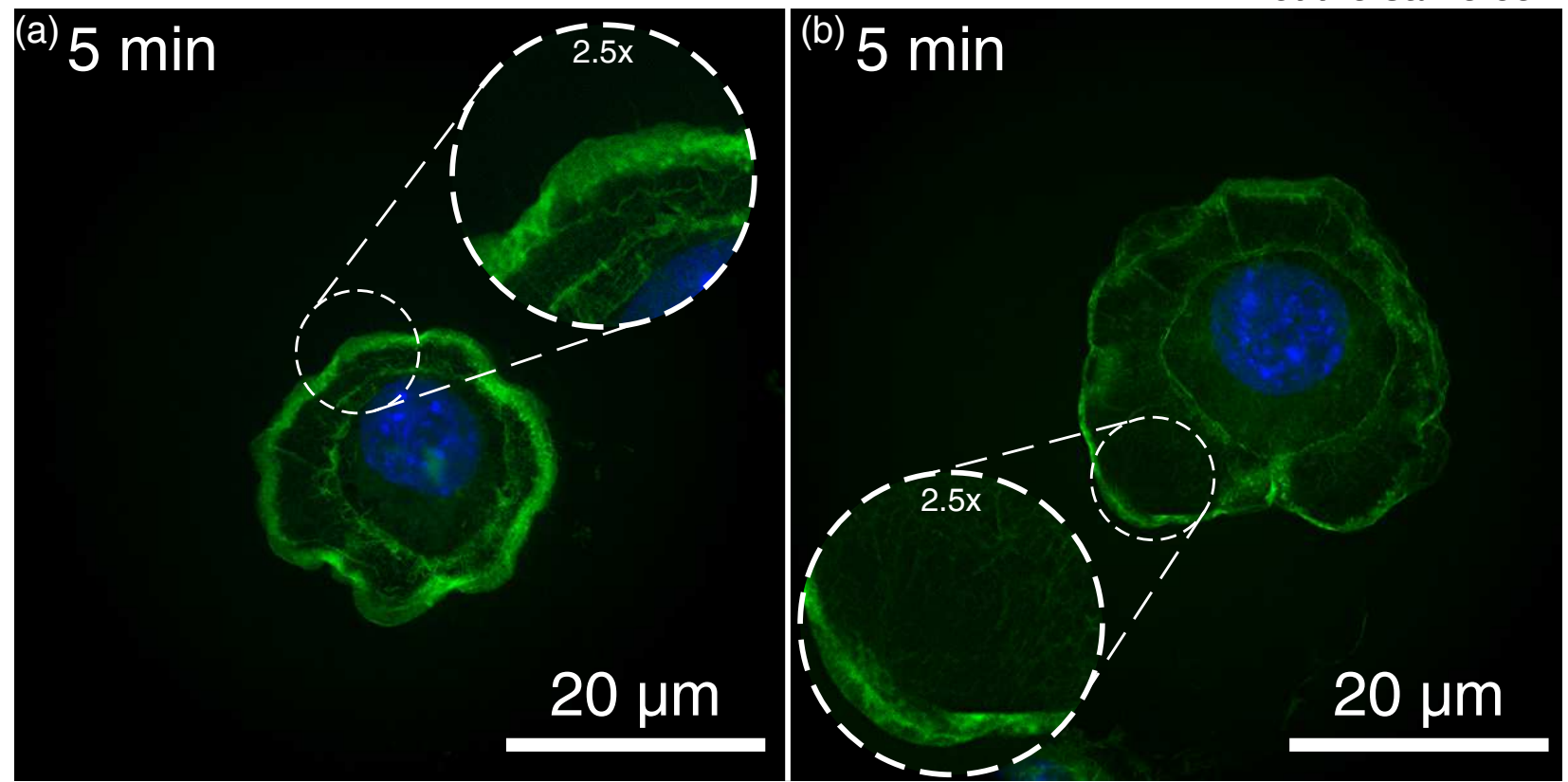


Figure 5.5: F-actin structure during P1 frustrated phagocytosis. Cells were allowed to undergo FP for 5 min after which they were fixed and stained with Phalloidin (green) and DAPI (blue). Cells were imaged using SIM. F-actin (green) forms a dense zone near expanding perimeter. This is suggestive of ARP2/3 filament branching, similar to what is observed at the leading edge of migrating cells.

22

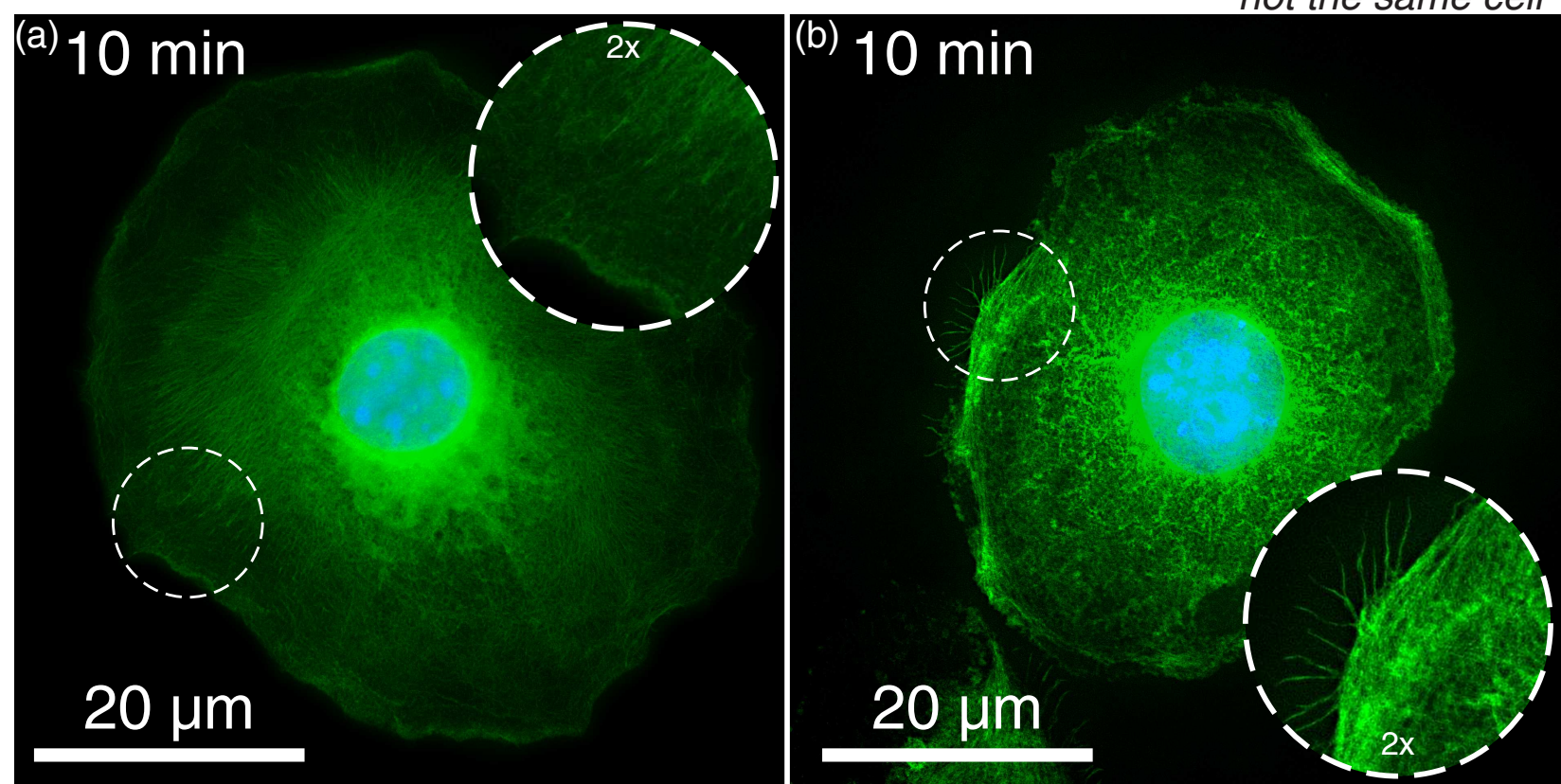


Figure 5.6: F-actin structure during P1-P2 transition. Dense zone of actin associated with the expanding edge during P1 is absent. (a) Bundled filaments can be seen throughout the cell. These filaments do not strictly align in a single direction but striation generally appears to be radial. (b) Beginning to show signs of contraction. Retraction tethers are present on the upper left side. Banding at the perimeter appears to contain striations which run parallel to the edge.

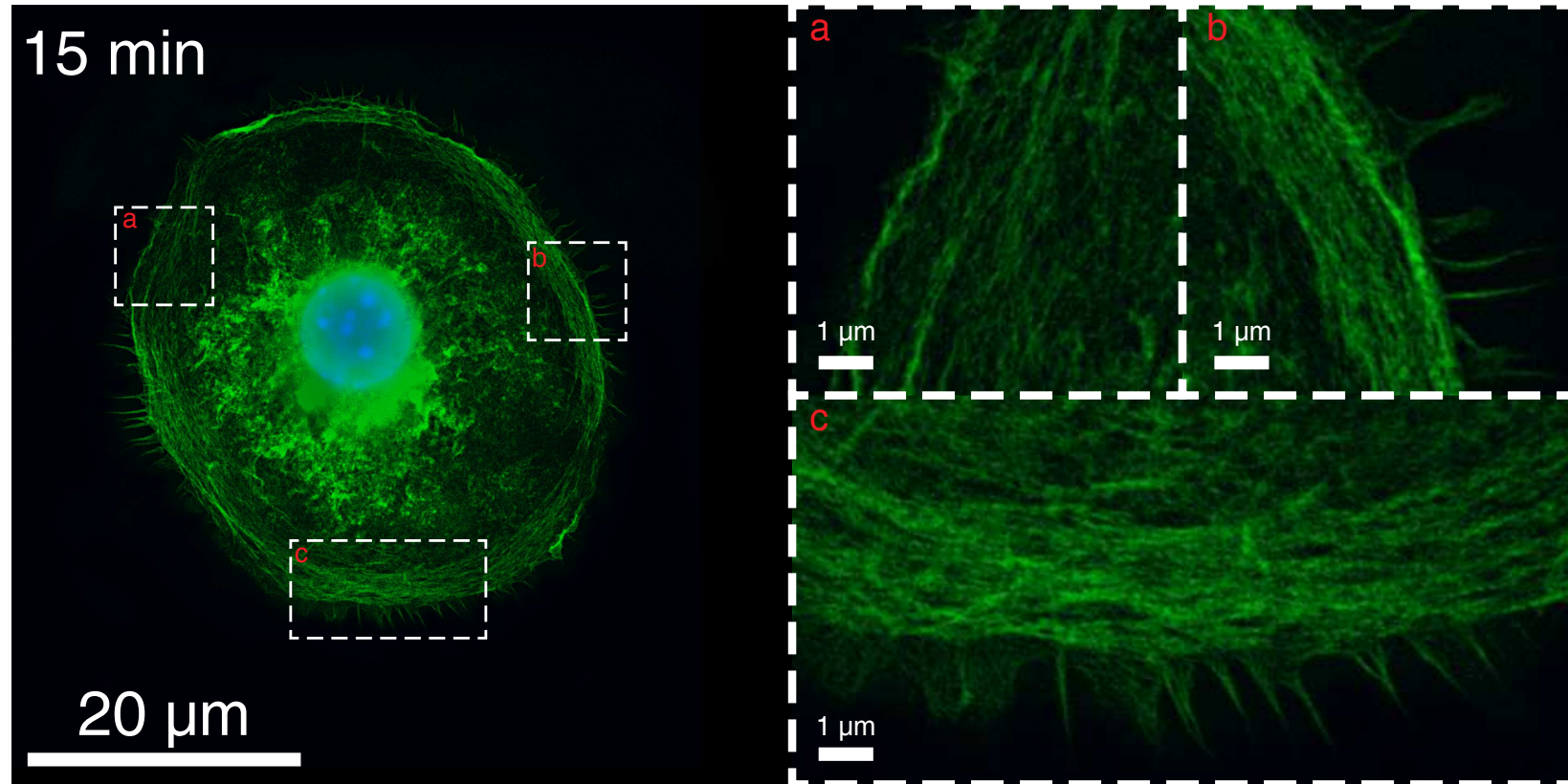


Figure 5.7: F-actin structure during contraction phase. Cells were allowed to undergo FP for 15 min after which they were fixed and stained with Phalloidin (green) and DAPI (blue). Cells were imaged using SIM. Striated banding that run parallel to contracting edge. This banding indicates that F-actin is bundled into long fibers. Fiber intensity correlates with the presence of retraction tethers.

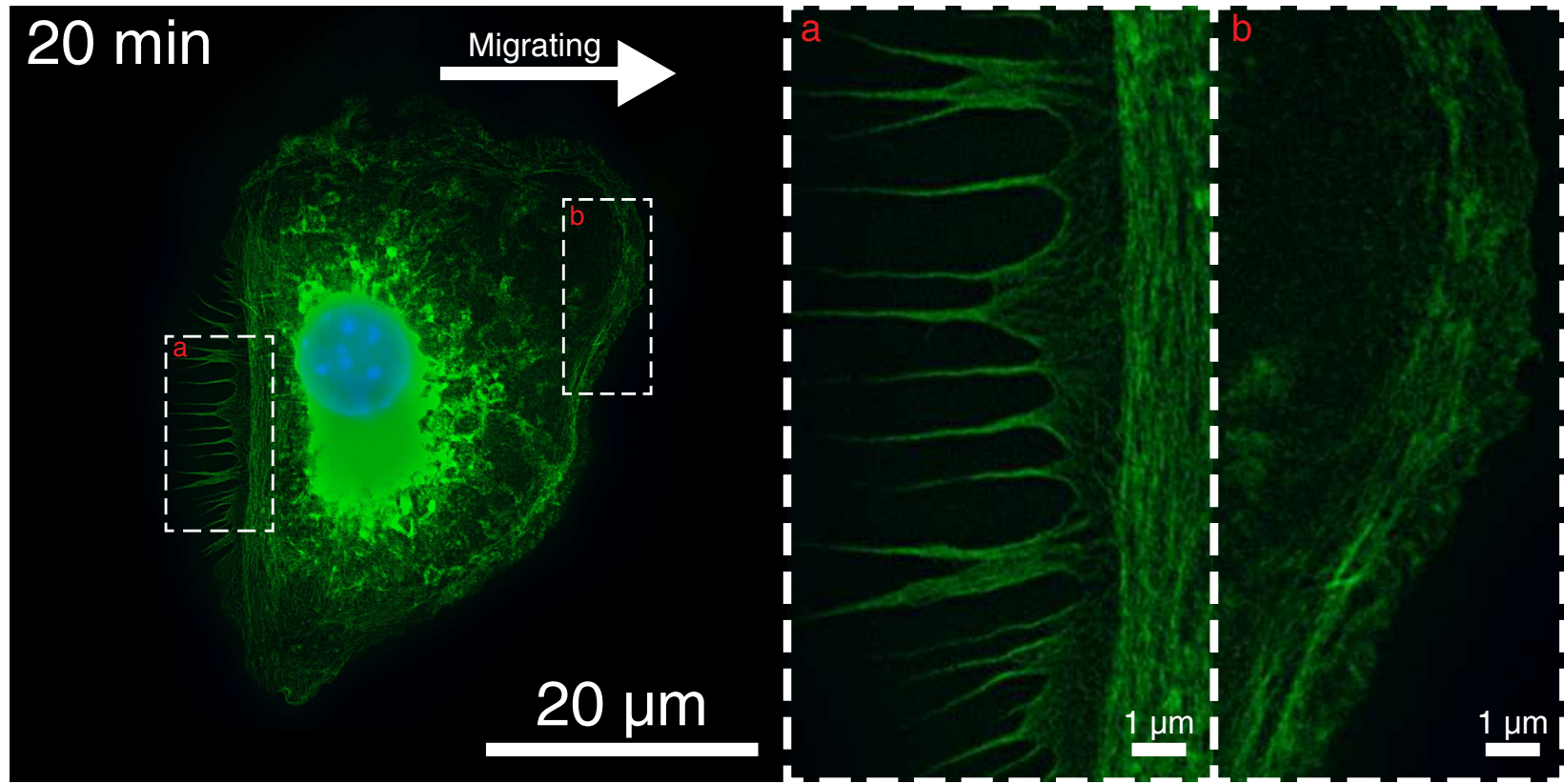


Figure 5.8: F-actin structure during macrophage migration. Cells were allowed to undergo FP for 20 min after which they were fixed and stained with Phalloidin (green) and DAPI (blue). Cells were imaged using SIM. Cell is polarized and migrating to the right. (a) F-actin is bundled in parallel fibers at the trailing edge. (b) Striations are absent directly adjacent to the leading edge, suggesting the F-actin network has a similar structure to leading edges of P1-stage cells. Behind this zone, actin is bundled similar to what is observed during contraction.

5.4 Discussion

5.4.1 Late-stage frustrated phagocytic contraction is an active process

The traction force measurements discussed in section 5.3.1 clearly show that late-stage FP contraction is an active process. Our measurements demonstrate that macrophages exert contractile stress in excess of 100 Pa. This is an order of magnitude greater than what one would expect for contraction only due to passive cortical tension relaxation (see calculation in eq 5.2). The stresses measured were consistent with those reported for migrating cells [136, 2, 25, 39]. This result indicates that molecular motor machinery within the cell plays a significant role during late-stage FP. This is in agreement with traditional phagocytosis assays which have shown that myosin motors inhibition blocks particle internalization [134].

5.4.2 F-actin architecture during P1-spreading is consistent lamellipodial extension

Given the significant overlap in the molecular machinery responsible for driving phagocytosis and cell migration one would expect F-actin architecture during FP to be similar to the architecture present within migrating cells. Our results indicate that there are many structural similarities between the two behaviors. The fluorescent F-actin images in Figure 5.5 indicate that F-actin is highly concentrated at the cell perimeter. Similar dense structures are present at the leading edge of migrating cells. Based on this similarity, it is probable that phagocytic cup formation (and P1-spreading) is driven by mechanisms similar to those which drive lamellipodia. In other words our results validate the lamellipodial model of phagocytic cup formation.

5.4.3 Last-stage contraction includes actin bundling

Our results show that F-actin bundles into distinctive bands which run parallel to the contracting edges during late-stage FP. This is significant because it confirms that F-actin is capable of forming long fibers which run azimuthally around the edge of the cell, as required by the “contractile belt model” [131]. Images taken during the transition between P1-spreading and P2-contraction (Figure 5.6) show that these bands form during contraction and are not present at earlier stages. In particular, Figure 5.6a indicates that prior to

contraction fibers are dispersed throughout the cell and are not aligned with the perimeter. During the transition from P1 to P2 the F-actin network must reorient from the radial direction stipulated in the lamellipodial model to the azimuthal direction, as shown in Figure 5.7.

5.4.4 Mechanisms for filament reorganization

Cells undergoing migration contain both structural motifs. As shown in Figure 5.8, F-actin bundles are aligned with the trailing edge. The leading edge, however, is characterized by a zone of unbundled F-actin, consistent with what was observed during P1-spreading. Similar F-actin architecture is present in migrating keratocytes [130].

In migrating keratocytes, F-actin polymerizes at the leading edge, forming a highly branched network which supports the traveling lamellipodium. The base of the lamellipodium contains bundled F-actin fibers which run the width of the cell (Figure 2.4). Both of these structures persist as the cell moves, even though the actin network is under constant reconstruction as dictated by the actin treadmill (see chapter 2.2.2). This means F-actin filaments rotate as they are shuttled towards the rear of the cell.

The mechanisms responsible for formation of this band remain an active area of research; however, it has been theorized that myosin contraction throughout the lamellipodium exerts torque on the forward-directed lamellipodial F-actin filaments causing them to rotate into parallel alignment [130, 3, 153, 114, 118]. This theory is termed the “dynamic contraction

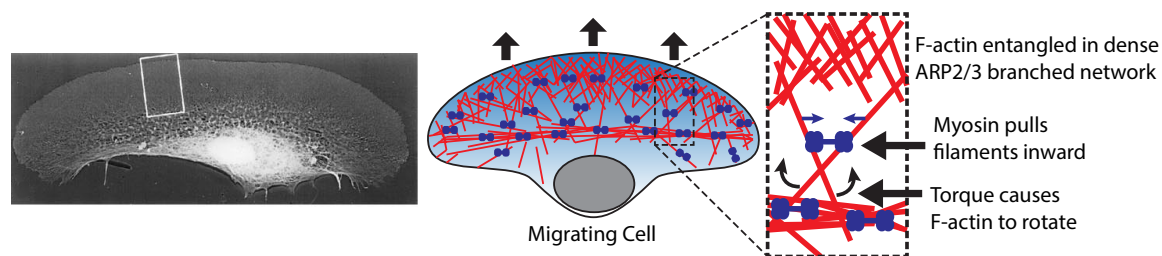


Figure 5.9: Dynamic contraction model. Counter-acting myosin II filaments bind intersecting F-actin bundles and exert a force directed toward the center of the motor filament. Long F-actin bundles extending into the densely packed lamellipodium experience a torque due to this force. This torque rotates the fibers into alignment perpendicular to the direction of migration.

model.” Central to this theory is the idea that F-actin fibers within the lamellipodium are mechanically jammed due to their close packing. At the base of the lamellipodium F-actin fibers depolymerize due to the molecular kinetics of the actin treadmill. As fibers depolymerize the local packing density decreases, allowing filaments to move.

Torque is exerted on F-actin fibers by myosin II motors³. Myosin II motors walk along F-actin exclusively from pointed end to barbed end, essentially from the center of the cell toward the leading edge. Counter-acting myosin II filaments bind intersecting F-actin bundles and exert a force directed toward the center of the motor filament (see Figure 5.9). Long F-actin bundles extending into the densely packed lamellipodium experience a torque due to this force. This torque rotates the fibers into alignment perpendicular to the direction of migration.

5.4.5 Dynamic contraction model of phagocytosis

Using the dynamic contraction model (DCM) of cell migration as a framework, we can construct a qualitative model which explains how actin is reorganized during frustrated phagocytosis (and traditional phagocytosis by extension). The stages of this model are illustrated in Figure 5.10. Under our model, spreading is driven by a symmetric lamellipodium-like zone of branched F-actin. We note, however, unlike the standard DCM myosin must be relatively inactive during this initial stage because F-actin remains unbundled throughout most of the cell, even at the base of the expanding lamellipodial zone. (Recall, F-actin bundling is not observed during early FP, see Figure 5.5.) As the cell approaches its maximum area F-actin begins to depolymerize throughout the lamellipodial-zone. This leads to a reduction in local network density, enabling F-actin fibers to move more freely.

At this point myosin motors engage with the disordered network. As in the DCM, myosin induced torque causes filaments to rotate, creating bands of F-actin which surround the cell. Under further myosin activity, this band constricts causing the cell to contract. As this process continues asymmetries in the band cause the cell to polarize, whereby one side expands while the other contracts.

³See chapter 2.1.5 for introduction to myosin II

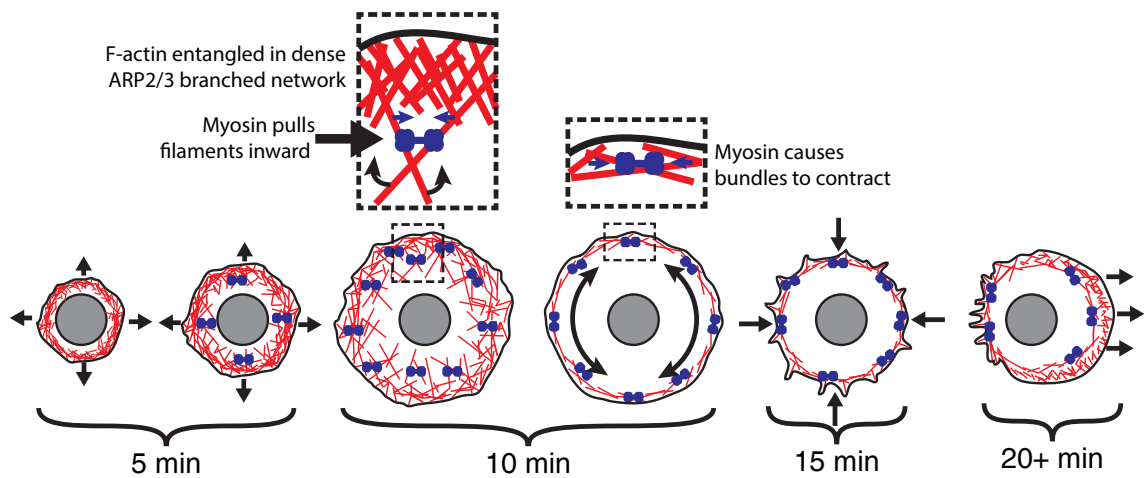


Figure 5.10: Dynamic contraction model for phagocytosis. 5 min: Spreading is driven by a symmetric lamellipodium-like zone of branched F-actin. 10 min: Cell approaches its maximum area, F-actin depolymerize throughout the lamellipodial-zone, leading to a reduction in local network density, enabling F-actin fibers to move more freely. 10a min: Myosin motors engage with the disordered network. 10b min: Myosin induced torque causes filaments to rotate, creating bands of F-actin which surround the cell. 15 min: Myosin activity creates tension along bands, causing cell to contract. 20+ min: Asymmetries in the band cause the cell to polarize, resulting in migration.

It remains to be determined what initiates these mechanisms. For instance, it is unknown why the F-actin network begins to depolymerize after 5-10 minutes. One explanation may be that actin depolymerization (or, alternatively, enhanced myosin activity) is a consequence of the late-stage phagocytosis signal cascade. Experiments have shown that interrupting late-stage signaling via PI3-kinase inhibition⁴ stops contractile belt formation and prevents phagosomal closure [133, 155, 12]. As an alternative, it has been proposed that tension sensitive membrane-bound proteins may be responsible for inducing biochemical changes which signal contractile activity [41, 95]. Experiments have shown that increasing membrane tension either through micro-pipette aspiration or hypotonic shock results in the collapse of expanding lamellipodia [69, 55]. The exact enzymes responsible for tension sensitivity have yet to be identified in phagocytes.

⁴See Chapter 2 for review of signal cascade and role of PI3-kinase.

CHAPTER VI

MYOSIN ACTIVITY REGULATES SPREADING SYMMETRY AND CYTOSKELETAL BUNDLING DURING LATE STAGE FRUSTRATED PHAGOCYTOSIS

6.1 *Introduction*

In the previous chapter Traction Force Microscopy (TFM) revealed that late-stage frustrated phagocytic contraction requires molecular motor activity. Fluorescent super-resolution imaging of the actin cytoskeleton revealed that the network undergoes structural reorientation prior to the onset of contraction. Snapshots of F-actin architecture over the course of phagocytosis demonstrate that changes in the network are consistent with the dynamic contraction model (DCM) [130, 3, 153, 114, 118]. Under the DCM, myosin motors are responsible for generating the forces necessary to reorient F-actin fibers and ultimately cause the cell to contract.

Given the theorized importance of myosin's role in shaping actin architecture and regulating cellular protrusions a number of studies have attempted to quantify its affect by monitoring changes in cell shape and behavior after its inhibition. Myosin role has been assessed in numerous cell types and in the context of many cell behaviors. The experiments presented in this chapter assess myosin's role in frustrated phagocytosis (FP). We present a series experiments which quantify the effect of myosin inhibition during the phases of FP. Under these assays myosin is inhibited using the drugs blebbistatin, ML-7, and wortmannin. Cell behavior is quantified using the methods developed in Chapter 4.

6.2 *Background*

6.2.1 *Review of biochemical regulation of myosin*

Before discussing experiments documenting myosin's role in cell migration, spreading, and phagocytosis it is instructive to first review of the biochemical signals known to regulate myosin activity. Myosin II is a hexamer composed of two heavy chains, two essential light

chains, and two regulatory light chains. The heavy chains form the motor head unit and contain actin binding domains and ATPase domains. When activated, myosin hydrolyses ATP into ADP. This energy liberation powers the ratchet mechanism which enables myosin to pull itself along F-actin. Myosin activity is predominantly regulated by conformation-altering phosphorylation sites located in the regulatory light chains, often called myosin light chains or MLCs.

Thus far, three classes of enzymes have been shown to be the primary activators of MLC: myosin light chain kinase (MLCK), Rho-associated kinase (ROCK), and p21-activated kinase (PAK) [17]. Myosin is also deactivated by MLC phosphatase, which counteracts MLCK by dephosphorylating the MLC [76]. In the contexts of cell migration, spreading and phagocytosis MLCK and ROCK have both been shown to affect cell behavior, presumably through their inhibition of myosin [5, 59, 143]. The involvement of each of these enzymes means there are two parallel pathways through which myosin can be stimulated.

The activity of MLCK is turned on when it binds with Ca^{2+} /calmodulin complexes, meaning myosin activity is strongly correlated with local Ca^{2+} concentrations [54]. In contrast, activation of myosin via ROCK is Ca^{2+} independent. Instead, ROCK is recruited to the cell perimeter via the phosphoinositol signaling system and activated by RhoA, which is also recruited by $\text{PI}(3,4,5)\text{P}_3$ [111, 16, 140].

6.2.2 Myosin Inhibitors

As discussed above, myosin is signaled by two pathways during phagocytosis, one which is dependent on MLCK and another which is depended on stimulation by ROCK via the Phosphatidylinositol signaling pathway. Both enzymes enable myosin by phosphorylating the MLC regulation region. Common methods of assessing myosin activity entail inhibiting the motor by disrupting activation of the regulatory light chain (MLC) or by disabling the ATP-powered heavy-chain.

Inhibition techniques which block MLC activation target either MLCK or ROCK. ML-7, Y-297632, wortmannin and LY294002 are drugs commonly used in these experiments. ML-7 specifically inhibits MLCK activity, providing a mechanism to assess the engagement

of the MLCK dependent pathway [117, 74]. Similarly, Y-297632 specifically targets ROCK, providing a mechanism to asses the ROCK dependent pathway. Wortmannin and Ly294002 are PI3-Kinase (PI3K) inhibitors. They disables PI3K, preventing the creation of PIP₃, effectively disabling ROCK and any other process dependent on phosphoinositol signaling.

Inhibition of the heavy-chain is often achieved through the use of the drugs blebbistatin or 2,3-Butanedione monoxime (BDM)¹. Both of those drugs bind to the ATPase region of the heavy chain, locking the motor in the ADP-Pi phase of its ATP-cycle, preventing myosin from engaging with F-actin fibers [78, 100].

6.2.3 Myosin activity during migration, spreading, and phagocytosis

6.2.3.1 Myosin activity during migration

The effects of various myosin inhibitors on cell migration have been documented by numerous studies. In migrating keratocytes, inhibition of myosin with blebbistatin causes those cells to form multiple lamellipodia. The activities of these lamellipodia are uncoordinated. Each lamellipodium propagates in its own direction, pulling the cell into fragments [118]. The inhibition of myosin via MLCK inhibition had a similar, although less severe, effect. Under MLCK inhibition migrating fibroblasts produce multiple protrusion fronts but did not divide into multiple fragments [137]. MLCK inhibition also increases the frequency migrating cells change direction, suggesting myosin helps maintain lamellipodial polarity [137].

6.2.3.2 Myosin activity during “universal” spreading

Myosin inhibition of spreading cells yields behaviors similar to those observed during myosin-inhibited migration. Blebbistatin inhibition of spreading fibroblasts results in a loss of cell coherence, formation of multiple spreading fronts, and cell fragmentation [27]. Blebbistatin also reduces traction forces exerted during late-stage (P2) spreading [27]. The effects of MLCK and ROCK inhibition are not as pronounced as the effects of blebbistatin [58, 146]. In mouse embryonic fibroblasts, ROCK inhibition leads to a loss of stress fibers, but does not otherwise affect spreading; MLCK inhibition prevents late-stage (P2) spreading but does

¹ Although, historically, BDM has been as live-cell myosin inhibitor it has been shown to have broad effects on many non-myosin proteins and is, therefore, no longer used in live-cell assays [100].

not affect early symmetric (P1) spreading [58].

6.2.3.3 Myosin activity during phagocytosis

It is well documented that myosin is associated with phagosomal closure [40, 133]. MLCK inhibition leads to a dose dependent decrease in particle uptake [98, 5]. Inhibition of PI3-kinase (an “up-stream” regulator of myosin), via the drugs wortmannin and Ly294004, prevents phagosomal closure but does not stop phagocytic cup formation [134, 155, 5]. This suggests cup formation is independent of late-stage myosin activity [134, 133].

6.3 Experimental Methods

6.3.1 Myosin inhibitor dosages and effects

We assessed the effect of myosin inhibition using Blebbistatin, ML-7 and wortmannin. Working concentrations were chosen based on published dosages. The IC₅₀ for ML-7 is reported to be 20 μM [74]. Experiments conducted on spreading fibroblasts and migrating keratocytes have shown changes in cell behavior at concentrations ranging from 1-10 μM [72, 58, 97, 5, 71]. Wortmannin is reported to have an IC₅₀ value of 3 nM [151]; phagocytosis assays have shown particle uptake drops by 80% at 10 nM and 95% at 100 nM [108]. The IC₅₀ concentration for (-)-blebbistatin has been measured to be 2 μM [127]. Treatment with 50 μM blebbistatin has been shown to cause cell fragmentation in spreading fibroblasts and 100 μM has been shown to cause lamellipodia separation in migrating keratocytes [27, 118].

6.3.2 Myosin inhibition protocols

All three drugs were obtained from Sigma Aldrich (Wortmannin: W1628, ML-7: I2764, (-)-Blebbistatin: B0560). Each was reconstituted in DMSO following the manufacturer’s instructions. Blebbistatin experiments were performed at 2 μM. ML-7 experiments were performed at concentrations ranging from 1-20 μM. Wortmannin experiments were performed at 10 and 100 nM. Prior to the start of an experiment, drug-DMSO solutions were diluted in 5mL of DMEM with HEPES to the final working concentration. Following the protocol reported in Chapter 3, cell culture media was exchanged with the drug-treated media; cells were then scraped and tumbled for 30 minutes. Frustrated phagocytosis assays

Table 6.1: Myosin inhibitors and dosages used during experiments.

| Compound | Target | Dosage | Reported Effect |
|------------------|------------------------|---------------------------|--|
| ML-7 | Disables MLCK | 1,3,5,10,20 μM | Stops activation of MLC by MLCK |
| Wortmannin | Disables PI3K | 10, 100 nM | Stops downstream signaling related to phagocytosis |
| (-)-Blebbistatin | Binds ADP-Pi on Myosin | 2 μM | Locks myosin in ADP-Pi phase, stops motor activity |

were performed following the previously discussed procedure. Drugs, targeted effects, and dosages are summarized in table 6.1.

6.4 Effects of myosin inhibition on frustrate phagocytosis

Macrophage behavior during FP was highly dependent on the drug and dosage used to inhibit myosin. Treatment with wortmannin, ML-7, and blebbistatin each yielded different behaviors.

6.4.1 Wortmannin resulted in little to no spreading

During traditional phagocytosis, inhibition of PI3-kinase via wortmannin disrupts late-stage signaling. This prevents blocks the recruitment of myosin and prevents phagosomal closure[4, 134]. Although PI3K inhibition prevents particle internalization, it does not affect formation of phagocytic cups. Fluorescent images macrophages during PI3K-inhibited phagocytosis reveal that F-actin accumulates in the forming phagosome [4, 5, 155, 90]. Based on these reports, it has been hypothesized that initial spreading is independent of PIP₃ [131]. Contrary to that hypothesis, frustrated phagocytosis was completely blocked by wortmannin. At the 10 nM dosage, cells attached to the opsonized substrate in sporadic rough patches, having edges consistent with thin filopodial extensions. Cells were observed for over an hour. During that time contact areas remained low (below 500 μm^2). Suppression of spreading was further enhanced at the 100 nM dose. Under the higher dosage cells remained spherical. Occasional filopodia were observed, but contact areas remained below 50 μm^2 , meaning the cells did not settle to form hemispherical caps, as observed for non-spreading untreated cell (see Chapter 4).

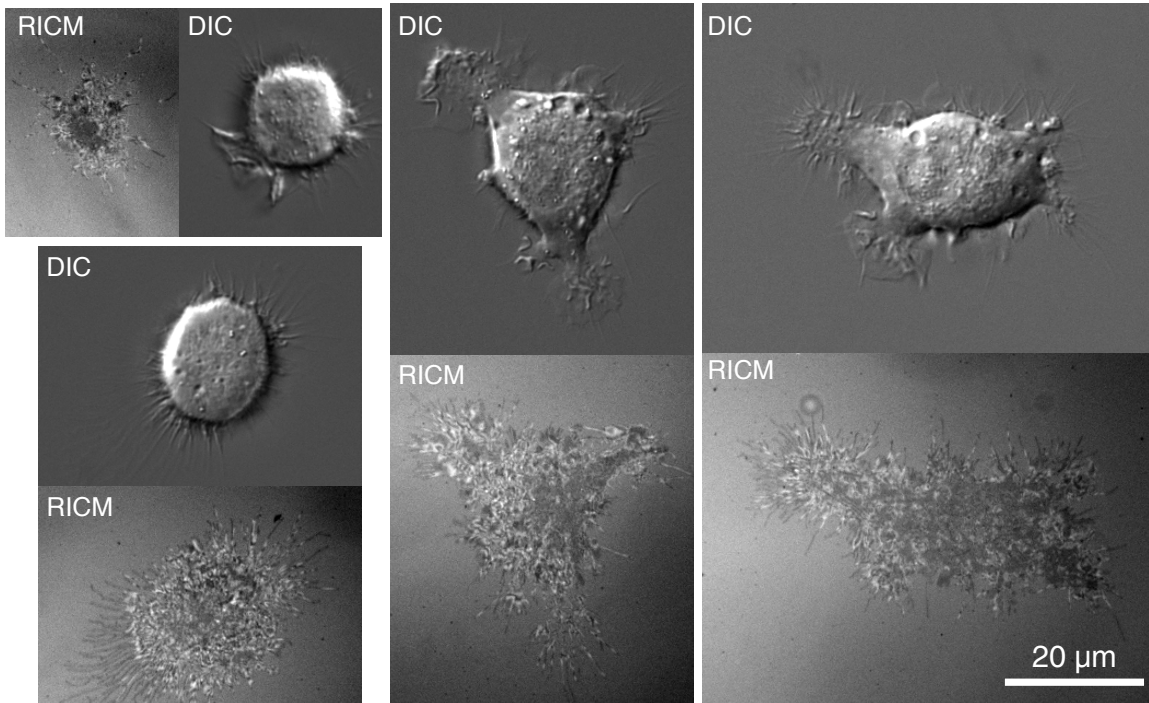


Figure 6.1: After treatment with 10 nM wortmannin for 30 min cells failed to engage IgG opsonized surface. Cells attached to surface in rough, sporadic manner. Sharp protrusions from the cell edge are consistent with filopodia. DIC and RICM pairs correspond to the same cell. All images are size to match the 20 μm scale bar.

These results suggest that the origin of signals which trigger large-scale cell spreading are down-stream of PI(3,4,5) P_3 formation. Given that the increased dosage prevented not only FP-related spreading but also the relaxation of cell bodies into hemispherical caps further suggests PI3K related signals may be involved in softening the cortex to allow the cell to undergo large deformations. Although the results presented here are distinct from behavior during traditional phagocytosis assays, they are not without precedent. PI3K inhibition through both wortmannin and Ly294002 prevents Fc γ -induced spreading in platelets and results in similar filopodial extensions [10]. Furthermore an number of studies have linked ARP2/3 function to PI(3,4,5) P_3 dependent signaling mechanisms [8, 73, 67]. Given that cell spreading and migration behaviors are dependent on ARP2/3 [18, 80], it is likely that wortmannin significantly impaired the formation of a lamellipodial spreading front during our experiments.

6.4.2 ML-7 treatment induces early cell polarization and migration but does not block late stage contraction

As discussed in Chapter 4, the majority of untreated macrophages undergoing FP spread symmetrically, contract, and then enter the migratory phase. Late-stage FP migration is characterized by complex lamellipodial motions, punctuated by pauses, turns, and reversals. Morphologically, migrating macrophages usually possess a wavy lamellipodium which extends from one side of the cell. This lamellipodium remains relatively narrow as the cell migrates.

Although early FP-spreading is typically symmetric, approximately 20% of the time cells spread asymmetrically. Asymmetrically spreading cells form a single lamellipodium, similar to those formed by keratocytes (see chapter 2). As with symmetrically spreading cells, the majority of asymmetric cells undergo a period of contraction after 10 minutes.

ML-7 treatment increased the fraction of cells which spread asymmetrically. This shift occurred in a dose-dependent manner. At the highest dosages measured (5, 10 μM) cells often became highly polarized, forming canoe-shaped lamellipodia reminiscent of keratocyte migration (figure 6.3b,e).

Formation of a polarized lamellipodium did not necessarily prevent late-stage contraction. Over the assayed concentration range (1-10 μM) late-stage contraction did not appear to be affected in a systematic way. Attempts to increase the dosage to 20 μM appeared to have a toxic effect on the cells. At that dosage cells in suspension were highly non-spherical and those which settled to the opsonized substrate failed to form stable attachments. Statistics are illustrated graphically in figure 6.3. Similarly, ML-7 did not significantly alter peak contact-area (see figure 6.2).

Persistence of late-stage contraction under ML-7 may be due to the fact that MLC-kinase (the target of ML-7) is not the only enzyme responsible for activating myosin. ROCK also activates myosin. As discussed in section 6.2, ROCK is PIP₃ dependent. Given the prominent role of PIP₃ in phagocytosis, it is likely that ROCK activity is significant.

6.4.3 Blebbistatin treatment blocks late-stage contraction, leads to larger contact areas, and induces cell fragmentation

In contrast to the ML-7 results, blebbistatin reliably blocked late-stage FP contraction. Under blebbistatin treatment, only 2 of 34 cells contracted within the 30 min period of our experiments. This is a significant change from the untreated behavior. It is important to point out that, unlike ML-7 which only blocks the MLCK pathway, blebbistatin interferes with myosin directly and is therefore independent of signaling pathway.

Blebbistatin not only prevented late stage contraction but also resulted in significant increases in peak contact area. Blebbistatin treatment yielded cells which spread to a mean area of $1773 \mu\text{m}^2$ with a standard deviation of $668 \mu\text{m}^2$, compared to untreated cells which had a mean area of $1095 \mu\text{m}^2$ and a standard deviation of $538 \mu\text{m}^2$. This difference is statistically distinct as verified by a two-sample t-test comparison performed using Welch's approximation for samples of differing variances: $t(57.8) = -5.0623, p = 4.51 \times 10^{-6}$. The results of this comparison as well as those for ML-7 treated cells are illustrated graphically in figure 6.3.

In agreement with reports concerning myosin inhibition during migrating and spreading, blebbistatin treatment of macrophages resulted in formation of multiple lamellipodia around the cell perimeter. These fronts appeared to act without coordination eventually pulling the cell into distinct fragments linked by narrow membrane tethers (figure 6.3c). Cells which did not fragment displayed a morphology similar to cells treated with high doses of ML-7. Non-fragmenting blebbistating treated cells became highly polarized and began migrating in a single direction.

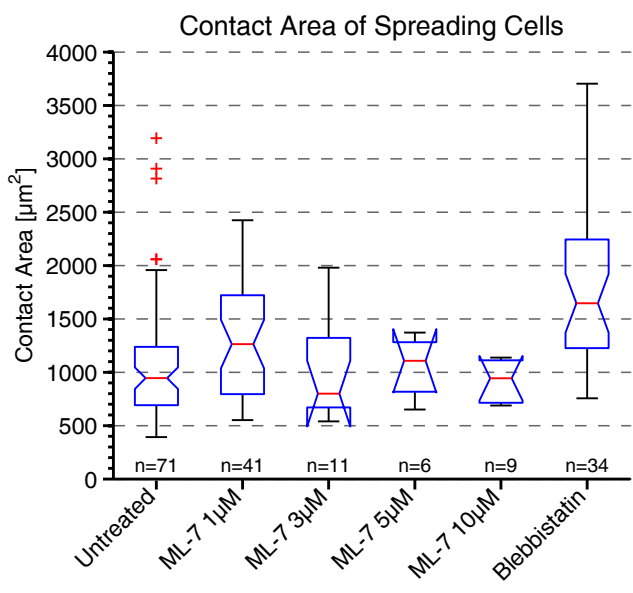


Figure 6.2: Red Line indicated median, notches indicate 95% CI, bounds of box indicate lower and upper quartile range, whiskers indicate $\pm 2.7\sigma$ for a normal fit or the limit of the data, whichever is closer to the median. red + indicate outlier which fall outside the $\pm 2.7\sigma$ range. Number of cells in each sample are indicated by n.

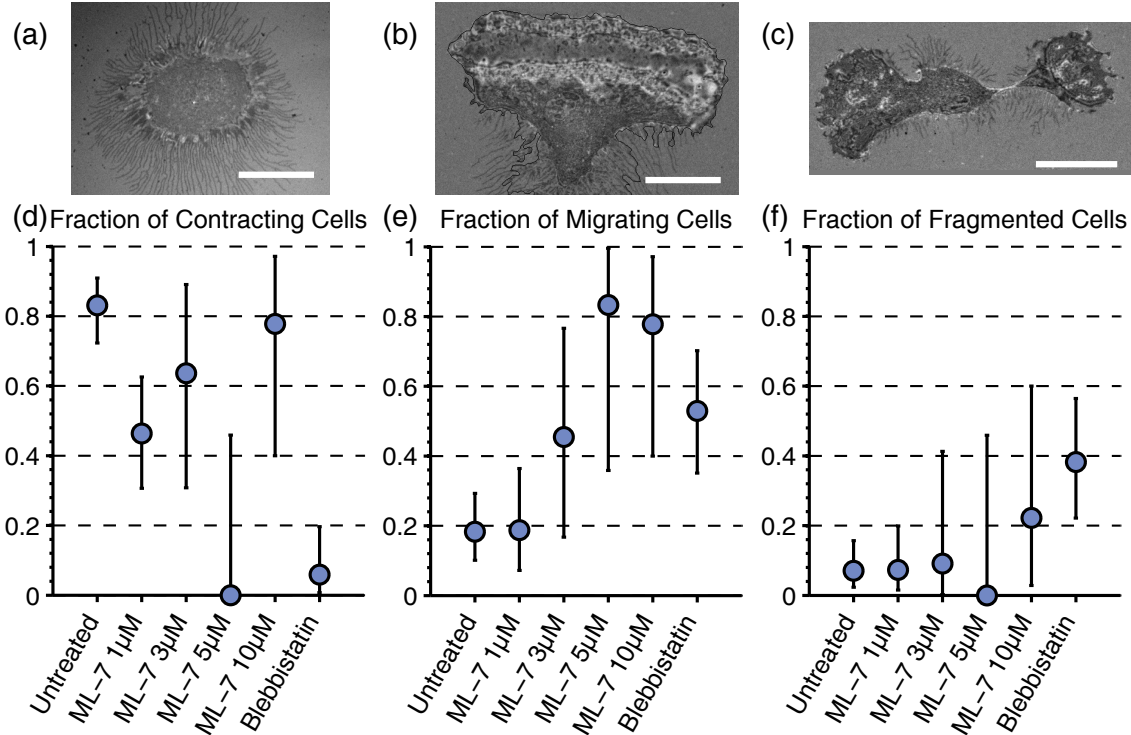


Figure 6.3: Behavior changes after myosin inhibition. (a) Contracting cell (b) Highly polarized migrating cell (c) Fragmented cell. All scale bars indicate 20 μm . (d) Fraction of cells which contract during 40 minute observation. (e) Fraction of cells which form a single polarized lamellipodium during observation period (f) Fraction of cells which have at least two oppositely directed spreading fronts which act to pull the cell apart. Note: three categories are not mutually exclusive. Error bars indicate 95% CI for binomial fit.

6.5 Cell spreading dynamics under myosin inhibition

6.5.1 Protrusion speed under myosin inhibition

Protrusion spreading rates for untreated and myosin inhibited cells by measuring the differences in leading-edge velocity between the two populations. In Chapter 4, I introduced the protrusion speed as being the rate ($\mu\text{m}/\text{s}$) at which a portion of the cell spreads in a direction normal to its leading edge. In the case of a circularly symmetric cell, this reduces simply to the rate of change of the cell radius. This simple radial definition of protrusion speed fails for non-circular cells, where the edge normal-line is not parallel to a radial vector. Although not always circular, cells undergoing frustrated phagocytosis typically spread in a smooth and uniform fashion. Spreading edges tend to propagate in smooth arcs away from the initial point of contact. In such cases, cell growth rates are well characterized by the time rate of change of the location of a cell edge where it intersects a vector in the center and approximately normal to an expanding protrusion (see Figure 4.3).

In most cases, myosin inhibited cells did not spread with smooth edges. Instead spreading occurred through brief localized bursts. During the initial spreading phase the spreading curves of untreated cells are typically smooth and monotonically increase with time. The location of the leading edge of those cells also expands roughly linearly during the initial spreading phase (see Chapter 4). In contrast, blebbistatin treated cells typically yielded jagged spreading curves correlating with rapid cycles of expansion and stagnation. While average growth rates typically ranged between $0.015 - 0.075 \mu\text{m}/\text{s}$, slightly slower than untreated cells, protrusion rates during bursts of growth ranged as high as $0.15 \mu\text{m}/\text{s}$.

6.5.1.1 Protrusion/retraction activity during cell migration and spreading

In Chapter 4, I introduced the concept of visualizing dynamic spreading and migration behavior using protrusion/retraction activity maps. Sheets *et al.* have shown that fibroblast spreading occurs in three phases of protrusion activity: initial contact (P0), isotropic growth (P1), and migration characterized by periodic waves of protrusion and contraction (P2). In Chapter 4.3.2.2 I discussed our use of level-set methods based cell-perimeter tracking algorithms to create protrusion/retraction maps of frustrated phagocytosis. Our results reveal

that the majority of macrophages undergoing FP have activity maps similar to fibroblasts except that P2 migration is typically replaced with largely uniform and temporally extended contraction period, consistent with the idea that frustrated phagocytosis ends with whole-cell contraction.

There are conflicting reports concerning the role of myosin in regulating the periodicity of protrusion waves. The results of Giannone *et al.* show that in fibroblasts ML-7 inhibition of myosin completely disrupts protrusion waves while inhibition of ROCK has no effect on protrusion activity [58]. Burnette *et al.* report that blebbistatin treatment of epithelial cells increases protrusion/retraction periodicity [23]. Conversely, Machacek *et al.* report that blebbistatin has no effect on epithelial activity [88]. Given these conflicting reports it is likely that many cell-type specific factors such as the availability of free G-actin, ARP2/3, Rac activity, and the relative activity of MLCK versus ROCK play a role in determining cell phenotype.

6.5.1.2 Macrophages treated with blebbistatin spread/migrate through localized bursts in late-stage frustrated phagocytosis

Inhibition of myosin had little observable effect on the protrusion activity of early-stage frustrated phagocytosis. As with untreated cells, early stage (P1) spreading is characterized by a 5-7 minute period of rapid protrusion, nearly uniform around the cell perimeter. In late-stage FP (P2), cells which demonstrated the migratory phenotype have protrusion/retraction activity maps consistent with cell polarization. In these cases, protrusion is confined to a portion of the cell perimeter while the rest of the perimeter either remains fixed or retracts. Protrusion at the lead edge occurs in localized bursts. Unlike fibroblasts and epithelial cells, protrusive bursts did not appear to be periodic. Time-space autocorrelation of activity maps during P2 migration occasionally reveal a slight skew, suggesting that protrusion burst propagate laterally. The lack of side-bands in these autocorrelations confirms that these bursts are likely aperiodic. An example of these results is included in figure 6.4.

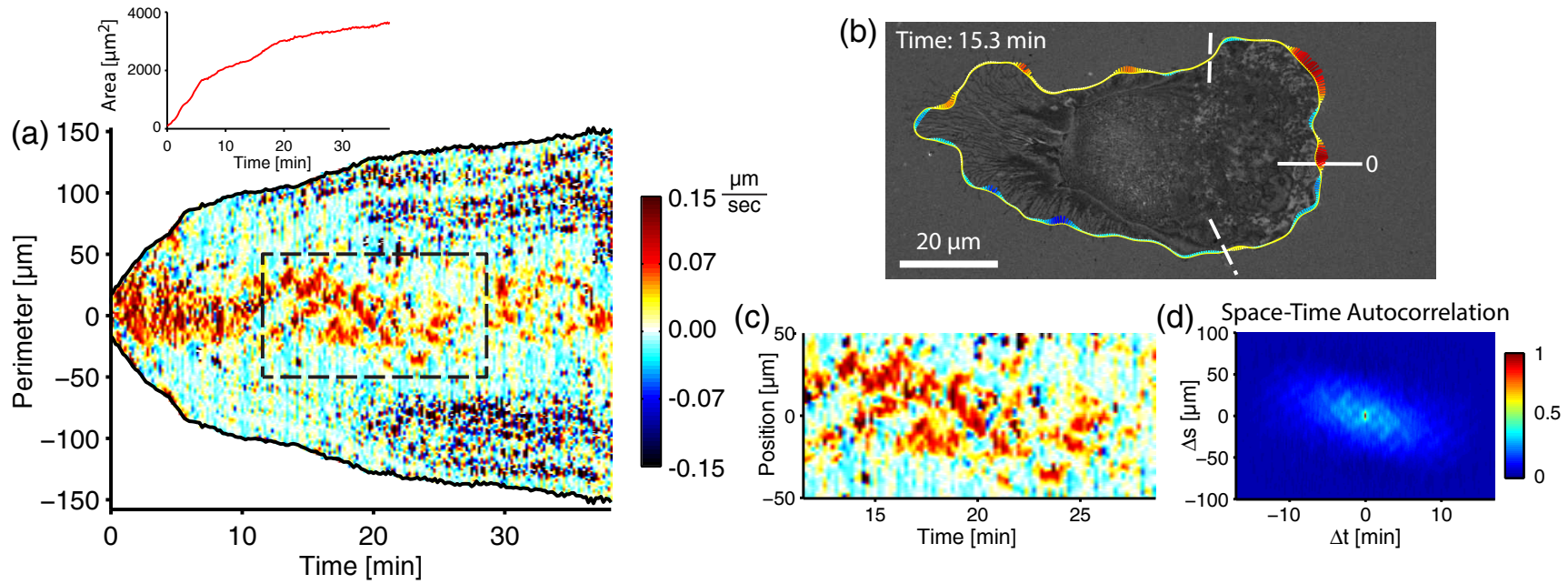


Figure 6.4: Migrating blebbistatin inhibited cell with activity map. (a) Protrusion/retraction activity map. Initial spreading (0-5min) is consistent with isotropic spreading observed in untreated cells. In late-stage (10+ min) cell enters migratory mode. Protrusion occurs through uncoordinated bursts. (b) Image of migrating cell with edge velocity vector matching the colorscale. (c) Activity map only including leading edge. (d) Space-Time autocorrelation of protrusion activity. Heat-map is normalized to the magnitude at $\langle 0,0 \rangle$. Downward skew correlates with propagation shifting toward lower portion of lamellipodia. Absence of clear banding suggests protrusions are aperiodic.

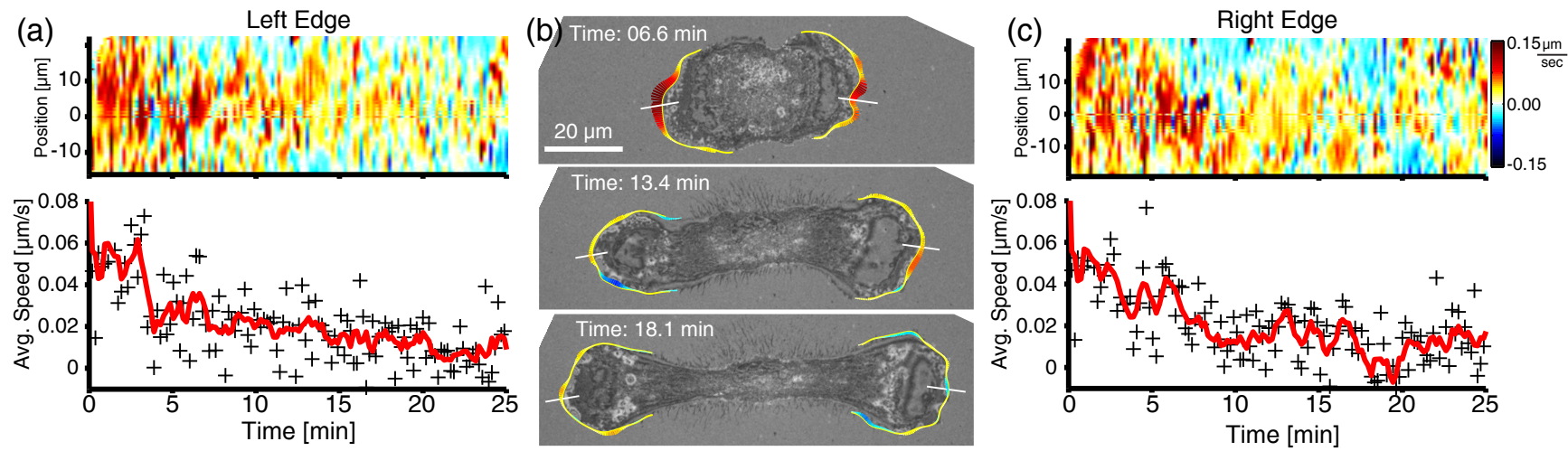


Figure 6.5: Blebbistatin induce cell fragmentation. (a,c) Activity maps of left and right spreading fronts. Scatter plots indicate the protrusion speed average along the arc-segment corresponding to each edge. + correspond to the computed average. Red lines are 5-point moving average of the data. (b) Micrograph of fragmenting cell. Protrusion magnitude decreases at cell is pulled further apart.

6.5.1.3 Protrusion bursts decrease in magnitude as fragmented cells spread

Cells which undergo fragmentation during P2 spreading show similar protrusive bursts (see figure 6.5). As opposing spreading fronts draw the cell into fragments the protrusive bursts decrease in magnitude. Burst duration does not appear to be affected by the existence of other fronts. A plausible explanation for this slow-down is that cell fragmentation causes a drastic increase in membrane tension. Increased tension establishes a force that opposes cell protrusion, reducing the speed of spreading. This hypothesis is supported by experiments which have shown that the keratocyte migration speed is attenuated when force is applied to the leading edge. These studies reveal a stall-point corresponding to tension on the order of 0.4 mN/m [107].

6.6 Conclusion

The dynamic contraction model (DCM) of cell migration stipulates that myosin motors are responsible for generating forces which reorganize F-actin over the course of migration. In the adaptation of DCM to phagocytosis presented in Chapter 5 myosin was not only responsible for F-actin reorientation but also powered late-stage contraction. The experiments presented here show myosin activity is required for late-stage contraction. Macrophages treated with blebbistatin spread to larger contact area and fail to contract. Myosin activity also appears to have a unifying effect on cell morphology. Blebbistatin treated cells often develop multiple spreading fronts which spread independently, eventually pulling the cell into fragments. Additionally, blebbistatin cells which do not fragment instead become highly polarized. This polarization results in highly motile behavior, reminiscent of keratocyte locomotion. Our experiments involving ML-7 show that inhibition of MLCK is not sufficient to stop late-stage contraction, suggesting that ROCK dependent signaling may play a significant role in frustrated phagocytosis. Although ML-7 does not stop late-stage contraction it does increase the likelihood a cell polarizes into a keratocyte-like geometry. Given that ML-7 inhibitory effect is likely less than that of blebbistatin, we hypothesize that a cell's average myosin activity determines whether it spreads symmetrically, polarizes, or (in the extreme) suffers a loss of cytoskeletal coherence (resulting in cell fragmentation).

Under this theory, spreading behavior lies on a continuum of myosin activity. In the situation where myosin has been completely disabled a cell forms multiple spreading fronts and eventually fragments. At the other end of the spectrum, myosin rapidly engages with the cytoskeleton causing the contractile behavior observed during late-stage frustrated phagocytosis. Polarized keratocyte-like behavior lies between these two extrema. Based on this notion, we suggest that different cell types may have myosin activity “tuned” to enable a specific behavior. Studies using various cell types have confirmed that major reductions in myosin activity result in fragmentation [118, 27] but the author is unaware of any study documenting the effect of myosin up-regulation. The results of such a study would certainly prove or disprove the theory presented here and would undoubtedly provide insight useful to both the migration and phagocytosis communities.

CHAPTER VII

HYDRODYNAMIC MODEL OF CELL SPREADING

7.1 Overview

In this chapter I present a generic model of cell spreading built around the principle of hydrodynamic wetting. This model integrates experimentally measured characteristics of the macrophages used here to predict cell spreading rates during P0 and P1 spreading. While this model does not directly address P2 contractility it suggests the way “macroscopic” mechanical properties such as cortical tension and effective cell viscosity affect spreading.

7.2 Motivation

In recent years, numerous models of cell migration and spreading have been proposed. While many of these models have advanced to the point of life-like simulation of cell behavior they often focus on reproducing a single cell characteristic (for instance: cell shape or actin architecture). Furthermore, these models typically rely on a large number of parameters which are cell-type specific and very sensitive to a cell’s biochemical activity. In many cases parameters used in these models are derived from *in vitro* experiments which may differ significantly from *in cellula*¹ levels. The growing complexity of these models also means they are often difficult to implement and computationally expensive.

Over the course of this chapter, I set out to develop a simplified model which is agnostic regarding the underlying mechanism particular to individual forms of spreading. The model does not rely on molecular scale processes like biochemical signaling or F-actin architecture; instead, it relies on macroscopic mechanical properties which can easily be measured for various cell types. My intention in developing this model is not to fully reproduce all variations observed throughout the course of our experiments but to capture approximate behavioral

¹I use the term *in cellula* to describe experiments conducted on whole live cells as opposed to *in vivo* which is typically reserved for experiments conducted in an animal. I use *in vitro* to denote experiments conducted at the sub-cellular or molecular level conducted outside of living cells.

trends and predict how cell-specific mechanical properties might affect that behavior.

7.3 Cell spreading as a hydrodynamic wetting process

Phenomenologically, frustrated phagocytosis and to a greater extent “universal” cell spreading are reminiscent of classic Sessile droplet wetting experiments commonly used in the field of surface science. Under these types of experiments small drops of a fluid of interest are deposited onto a substrate. Both the dynamic spreading rate and the equilibrium shape are used to characterize the fluid-substrate interactions. The most common metric obtained from these experiments is the adhesion energy. At equilibrium, a droplet on a surface forms a three-phase contact line, having a shape defined by Young’s equation,

$$\gamma_{SO} = \gamma_{SL} + \gamma_{LO} \cos \theta_e. \quad (7.1)$$

(γ_{SO} , γ_{SL} , γ_{LO} correspond to the surface tension at the solid/air, solid/liquid, and liquid/air interfaces, respectively. θ_e is the equilibrium contact angle formed at the droplet base. Alternatively, this equation can be recast in terms of adhesion energy, see equation 7.2.)

The comparison between cell spreading and fluid wetting is not without precedent. In some of the earliest quantitative analyses of phagocytosis, van Oss uses static contact angle wetting to estimate the adhesion energy between human neutrophils and various phagocytosis inducing substrates (including IgG)[141]. In later work, Brochard-Wyart and de Gennes use Young’s equation as a starting point in their analysis of vesicle and cell adhesion[20].

Dynamic wetting and hydrodynamics have also been used to model cell spreading processes. For example, Frisch et al. use hydrodynamic wetting theory to analyze the passive spreading of fibroblasts on fibronectin coated surfaces [51]. Similarly, Fardin et al. use a fluid mechanics model of viscous fingering to discuss the transition from symmetric P1 spreading into stochastic P2 spreading [48].

In the model presented here, we imagine early-stage (P0, P1) frustrated phagocytic spreading as a hydrodynamic wetting process. However, unlike traditional wetting fluids, the cell produces protrusive forces which drive the process. Furthermore, we incorporate the elastic effects of the membrane cortex through the inclusion of an effective surface tension which depends on the cell surface area. Following the formulation of hydrodynamic wetting

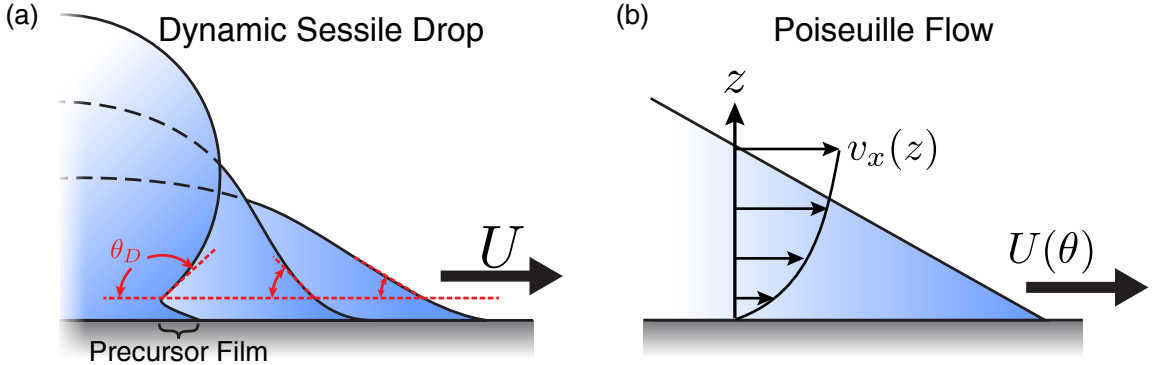


Figure 7.1: (a) Cartoon of dynamic Sessile drop profile. Small droplets approximate a spherical cap during spreading, except that the leading edge forms a precursor film. (b) Illustration of Poiseuille flow. Under the BWG wetting model, the liquid near the contact line is assumed to flow in a highly acute wedge with a flow corresponding to the “lubrication approximation”.

presented by Brochard-Wyart and de Gennes, we incorporate these two features into an area-time spreading curve analogous to those measured throughout this thesis.

7.3.1 Physics of wetting

Despite the fact that at their core wetting experiments are relatively simple, typically consisting of only three components (surface, fluid droplet, and surrounding gas), and involving very well-defined geometry, the physics of wetting remains an active area of research. Over the course of a dynamic Sesslie drop experiment, drops expand on the substrate with a macroscopic dynamic contact angle that scales with the contact line velocity. Microscopically, in the vicinity of the contact line the advancing fluid forms a precursor film characterized by a contact angle less than the dynamic angle.

Numerous models have been proposed to explain a critical feature of all wetting experiments, namely the dependence of the dynamic contact angle on the velocity of the liquid-solid contact line [15]. Our model builds upon the framework laid out by Brochar-Wyart and de Gennes (referred to as the BWG model) [19].

Formulation of the BWG model begins with the recognition that the work of adhesion between a liquid and an underlying surface manifests an equilibrium contact angle given by

the Young-Dupré equation,

$$W_a = \gamma (1 + \cos \theta_e). \quad (7.2)$$

During the spreading process, the effective contact angle of the drop is greater than the equilibrium value, yielding an effective surface tension given by

$$f_{adhesion} = W_a - \gamma (1 + \cos \theta). \quad (7.3)$$

This tension establishes an effective force directed away from the center of the droplet (towards direction of spreading). Underpinning the BWG model is the assumption that work done by this “non-compensated Young Force” is entirely dissipated by the viscous motion of the fluid inside the droplet. Furthermore they also assume that the majority of this dissipation occurs in the bulk of the drop and ignore the precursor film. Writing this in terms of the Gibb's equation differentiated with respect to time we have

$$T \frac{dS}{dt} = [W_a - \gamma (1 + \cos \theta)] \frac{dA}{dT}. \quad (7.4)$$

Over a fixed length contact line this reduces to

$$T \dot{S} = [W_a - \gamma (1 + \cos \theta)] \cdot U(t). \quad (7.5)$$

where $U(t)$ is the velocity of the contact line.

In the situation where the drop has already spread to small contact angles, the “lubrication approximation” warranted during Poiseuille flow can be used to estimate the fluid flow field inside the wedge representing the leading edge:

$$v_x(z) = \frac{3U}{2\zeta^2} (2\zeta z - z^2). \quad (7.6)$$

where ζ is the approximate height of the flowing wedge and U is the average velocity of the wedge. Integrating the velocity field over the length of the wedge, we can estimate the viscous force

$$f_v = \int_{x_{min}}^{x_{max}} \left. \frac{\eta \partial v_x}{\partial z} \right|_{z=0} dx = 3 \frac{\eta U}{\theta} \cdot \ln \frac{x_{max}}{x_{min}}. \quad (7.7)$$

Combining this result with eq 7.5 we achieve a final relationship which relates contact-line velocity with the contact angle

$$U(\theta) = \theta \cdot \frac{[W_a - \gamma (1 + \cos \theta)]}{3\eta \ln \frac{x_{max}}{x_{min}}}. \quad (7.8)$$

With this relationship in hand, we can set up geometric constraints to establish a differential equation which predicts the contact radius of the droplet as a function of time.

7.3.1.1 Wetting behavior is dependent upon the ratio of viscosities of internal and external fluids

Under this framework we represent our cell as a simple viscous fluid drop spreading on a surface for which it has a given affinity. In this representation we ignore the presence of water outside the droplet, instead focusing on the highly viscous behavior of the cell itself. Although it is true that the external fluid is partially responsible for the viscous dissipation of energy, rigorous models put forth by Cox have shown that for fluid-fluid-solid systems the characteristic spreading law is essentially dependent on the ratio of the viscosities between the two fluids[33]. As discussed later, macrophage cells have effective viscosities on the order of $4 \text{ kPa} \cdot \text{s}$, six orders of magnitude larger than the viscosity of water ($0.89 \text{ mPa} \cdot \text{s}$). Consequently, ignoring the viscous effects of the surrounding fluid should not significantly perturb the results of our model.

7.3.1.2 Small drops spread spherically

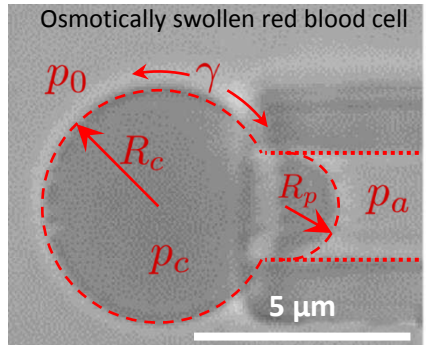
For small droplets, where capillary forces dominate over body forces (i.e., low Eötvös/Bond numbers), both experiments and solutions to the Navier-Stokes equation for the evolution of a free surface have shown that drop shape is approximated by a spherical cap [106, 52, 125]. Taking into account that volume is conserved, we can determine the exact relationship between the contact line radius and the contact angle

$$R(\theta) = \frac{2R_0}{\left((2 + \sec^2 \frac{\theta}{2}) \tan \frac{\theta}{2} \right)}. \quad (7.9)$$

Setting the contact line velocity found in eq 7.8 equal to the time derivative of the drop radius and applying the chain rule we find

$$\dot{\theta}(t) = \frac{\partial R(\theta)}{\partial t} \cdot \frac{1}{\frac{\partial R}{\partial \theta}} = U(\theta) \cdot \left(-\frac{R_0 \sec^4 \frac{\theta}{2}}{\left((2 + \sec^2 \frac{\theta}{2}) \tan \frac{\theta}{2} \right)^{\frac{4}{3}}} \right). \quad (7.10)$$

This time-ordered differential equation can be numerically integrated to yield the contact radius as a function of time.



$$p_0 - p_a = -2\gamma \left(\frac{1}{R_c} - \frac{1}{R_p} \right)$$

Figure 7.2: Osmotically swollen red blood cell under aspiration. Unlike other cells, red blood cells do not have membrane folds or micro-villi meaning they behave like simple vesicles. Application of the Young-Dupré equation yields the membrane tension. Image initially published by Hochmuth [68]. Adapted here with permission.

7.3.2 Incorporation of cellular mechanical properties

The above equation describes the expansion of a spherical fluid droplet. As discussed in 2.1, the cell is far more complex than a simple single component fluid. To account for this complexity we take the approach of modifying terms within equation 7.8 to account for two major characteristics of the cell: the presence of a hybrid membrane-cortex boundary and the ability of the cell to generate protrusive forces via actin polymerization.

7.3.2.1 Cortical tension

Macroscopically, the presence of a lipid membrane around a simple vesicle does not significantly alter its mechanical characteristics. Like the interface between a two immiscible fluids the membrane has a surface tension which drives the vesicle to form a sphere; however, unlike simple fluid-fluid systems, where tension is a consequence of the energy required to form the interface, tension in a membrane is a result of the energetics of stretching and bending the lipid bilayer. Similar to how one might measure surface tension between a droplet and a surrounding fluid, vesicle membrane surface tension can be measured by partially aspirating a vesicle into a pipette at a fixed pressure and applying the Young-Laplace equation [68].

For cells, in particular phagocytes, this simple behavior breaks down. The surface of

the cell is not a smooth, relatively flat, lipid bilayer. Rather, the plasma membrane is saturated with folds, ripples, and micro-villi. Additionally, just inside the cell, affixed to the plasma membrane, is an elastic protein cortex. A consequence of this complexity is that aspirated cells do not behave like simple vesicles. Instead, membrane tension assumes an experimentally observed dependence on apparent cell area [66, 81, 41]:

$$\gamma(A) \approx \gamma_0 + \kappa \frac{A - A_0}{A_0}. \quad (7.11)$$

In the above approximation, γ_0 and κ are experimentally measured constants which are cell-type specific; A corresponds the surface apparent area of the cell and A_0 is the initial area. To incorporate membrane-cortex behavior into our model we simply replace the constant γ of equation 7.8 with our experimentally observed area dependent version (eq 7.11).

7.3.2.2 Protrusive forces generated at the cell perimeter

Although adhesion energy between the cell surface and the underlying substrate is capable of causing the cell to spread, the results of the experiments presented in Chapter 4 clearly demonstrate that spreading dynamics are independent of ligand density. Phagocytic spreading is largely driven by active forces generated in the lamellipodium by actin polymerization. Confocal microscopic z-stacks reveal that the actin is concentrated almost exclusively at the base of the extending lamellipodium, suggesting protrusive forces are confined only to the base of the cell. In the context of our spreading model, this means that actin polymerization force, like the effective force of adhesion given in eq 7.5, only acts on the contact line. We can adapt our spreading law (eq 7.8) by supplementing the force of adhesion with an additional term representing the contribution of actin polymerization:

$$U(\theta) = \theta \cdot \frac{f_{protrusion} + [W_a - \gamma(1 + \cos \theta)]}{3\eta \ln \frac{x_{max}}{x_{min}}} \quad (7.12)$$

7.4 Estimating mechanical parameters

Combining eq 7.12 with eq 7.11, we see that we need a total of eight parameters to characterize a cell (x_{min} , x_{max} , η , A_0 , γ_0 , κ , W_a , and $f_{protrusion}$). Following the discussion put forth in BWG, the integration limits x_{min} , x_{max} are chosen to correspond to the approximate

molecular size (1 nm) and the approximate cell radius ($10\text{ }\mu\text{m}$). Excluding the integration limits, six parameters remain, each of which is experimentally measurable.

7.4.1 Initial cell surface area

The initial cell area is estimated by assuming the cell forms a sphere prior to the start of frustrated phagocytosis. Based on eq 7.11 the membrane tension scales inversely with the initial cell size. Intuitively this makes sense as larger cells should be able to spread to larger areas. In the experiments presented throughout this thesis, cell contact area was imaged using RICM. Unfortunately, RICM does not allow us to measure the initial size of the cell before spreading, meaning our data-sets do not include cell-by-cell measurements of the initial size. In the absence of cell-by-cell statistics we measured the population average by depositing our cultured macrophages onto polyethylene-glycol functionalized slides, which prevent cell adhesion, and imaged them using standard brightfield microscopy. The radii of 100 cells were measured: $\bar{R}_0 \pm 2\sigma = 8.4 \pm 1.4\text{ }\mu\text{m}$.

7.4.2 Membrane cortical tension

As discussed above, effective membrane cortical tension can be measured by micropipette aspiration. For the analysis presented here we use the resting tension γ_0 and area dependence κ measured for J774A.1 macrophages (the same cell type used throughout this thesis) reported by Lam *et al.* [81]. They report: $\gamma_0 = 0.14 \pm 0.2\text{ mN/m}$ and $\kappa = 0.15 \pm 0.4\text{ mN/m}$.

7.4.3 Cell body behaves as a viscous fluid

Even with the modification of the surface tension to depend on the cell surface area, the model we have developed inherently assumes that the body of the cell behaves purely as a fluid. Work performed by the adhesion force and protrusion force (eq 7.3 and numerator of 7.12) is entirely offset by viscous dissipation. Given the compositional complexity of the cell it is reasonable to think that the cytosol bears an inherent elasticity. Under such situations we can generically represent the cell as a Maxwell fluid coupled in parallel with an area-dependent tension. For small deformations, the surface area remains unchanged and we can represent the tension as a constant term. Figure 7.3 illustrates this model schematically. A

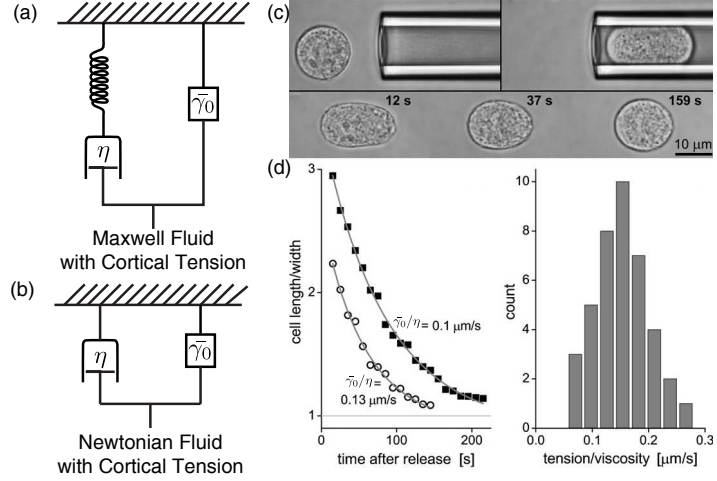


Figure 7.3: Viscoelastic behavior of macrophages. (a) Schematic of Maxwell fluid in parallel with tension from cortex. (b) Schematic of Newtonian fluid in parallel with tension. (c) Aspiration of J774A.1 macrophage results in elongation. Release of external pressure allow cell to recover. (d) Analysis of recovery time using model developed in Tran-Son-Tay *et al.* reveal cell behavior is predominately viscous at times longer than 5s. $\bar{\gamma}_0/\eta = 0.15 \pm 0.09 \mu\text{m}/\text{s}$. Result and (c,d) originally published by Lam *et al.*[81] Reprinted here with permission.

critical feature of the Maxwell model is that material responses over long enough time-scales are dominated by the viscous behavior. In that case the cell model reduces to a Newtonian fluid couple to the cortex, exactly as we have modeled our system.

To test whether cell behavior is dominated by viscous or elastic behavior, Tray-Son-Tay *et al.* developed a variational model of spherical shape recovery after mild elongation. Using their model they measured the viscoelastic response of neutrophils to mild deformation caused by aspirating individual cells into a pipette slightly smaller than the diameter of the cell. (See Figure 7.3c for an example.) They found that at aspiration times longer than 5 seconds, cell behavior was predominantly viscous [138]. Lam *et al.* repeated their analysis on J774A.1 macrophages and measured the ratio of cortical tension to viscosity to be $\frac{\gamma_0}{\eta} = 0.15 \pm 0.09 \mu\text{m}/\text{s}$ [81]. Using their measurement for the resting cortical tension, we can compute the average viscosity to be $\bar{\eta} = 0.91 \text{ kPa} \cdot \text{s}$ with lower and upper limits of $\eta_{-2\sigma} = 0.57 \text{ kPa} \cdot \text{s}$, $\eta_{+2\sigma} = 2.31 \text{ kPa} \cdot \text{s}$. In light of the findings of Tray-Son-Tay *et al.* and given that cell spreading occurs in minutes (not seconds), it reasonable to think that cell spreading is dominated by viscous behavior.

7.4.4 Estimate protrusion force using migration stall force

In building up to eq 7.12, we characterized the protrusion force simply as a constant outward-tension acting on the cell perimeter. In reality the strength of the polymerization force likely depends on a number of factors. For instance, many have suggested that the actin treadmill coupled with the membrane acts like a Brownian ratchet, whereby membrane tension regulates polymerization rates [94].² Furthermore, as demonstrated in the previous chapters, biochemical signaling plays a significant role in dictating cell activity. Consequently, protrusion force is the single parameter most likely to change from cell to cell and even during the course of spreading.

Despite this variability, we can estimate the approximate order of magnitude of such forces. Experiments conducted by Prass *et al.* showed that actin polymerization at the leading edge of migrating keratocytes is stalled when it is opposed by forces in the nano-Newton range. In their experiments they drove migrating keratocytes into vertically mounted AFM-cantilevers [107]. Using video microscopy to track cell motion and the AFM-cantilever to measure the normal force, they found that migration was halted at an average force $F_{stall} = 1.18 \text{ nN}$. Dividing that result by the width of their cantilever ($3 \mu\text{m}$) we find that the protrusive line-force (analogous to tension) is on the order $f_{protrusion} \approx 0.4 \text{ mN/m}$.

7.4.5 Adhesion energy small compared to work done by protrusion force

As discussed above, one method people have used to characterize the adhesion energy between cells and substrates is using the Young-Dupré equation. Under such experiments, cells are metabolically inhibited (to prevent active spreading) and placed in contact with a surface. Cell shape is imaged in-profile and eq 7.1 is used to estimate the adhesion energy based on the equilibrium contact angle. Reports for other cell-types have indicated that cell-substrate adhesion typically ranges between $0.05 - 0.8 \text{ mJ/m}^2$ [51]. These values are of the same order as the protrusion force calculated above.

²Under this scenario, thermal vibration causes the membrane at the cell perimeter to move away from the underlying F-actin network. During this period g-actin monomers polymerize at the leading barbed end, filling in the gap between the filament and the membrane. This acts as a backstop preventing the membrane from recoiling back to its initial position.

Table 7.1: Average and estimated mechanical parameters for J774A.1 macrophages.

| Parameter | Value |
|------------------|---|
| R_0 | $8.4 \pm 1.4 \mu\text{m}$ |
| γ_0 | $0.14 \pm 0.2 \text{ mN/m}$ [81] |
| κ | $0.15 \pm 0.4 \text{ mN/m}$ [81] |
| η | $0.91 \quad [\eta_{-2\sigma} = 0.57, \eta_{+2\sigma} = 2.31] \text{ kPa} \cdot \text{s}$ [81] |
| $f_{protrusion}$ | 0.4 mN/m [107] |
| W_a | $0.005 - 0.8 \text{ mJ/m}^2$ [51] |

The technical difficulty of performing accurate equilibrium contact angle measurement on cells prevented us from verifying these numbers for macrophages on our opsonized substrates. It is important to point out that our model places $f_{protrusion}$ and W_a on exactly the same footing (eq 7.12). Under this formulation, variations in spreading behavior are equally affected by variation in adhesion and protrusion force. Given that cell contact area is roughly independent of IgG opsonization density (see Chapter 4) it is likely that surface adhesion only plays a small role in determining the final contact area of the cell.

7.5 Characteristics of the model

7.5.1 Model exhibits tanh-like spreading, similar to experiments

Using the parameters estimated above, we can integrate eq 7.10 combined with eq 7.12 to find the time-dependent contact area. To realize this solution, we numerically integrate the differential equation using a classical Runge-Kutta method (RK4), starting at an initial contact radius $R = 0$ and initial angle $\theta = \pi$. The results of this integration using the average parameters are plotted in Figure 7.4. Qualitatively, the model bears a strong resemblance to the area-time curves for “universally” spreading (non-contracting) cells.

7.5.2 Model captures range of observed behavior

One of the obvious features of the frustrated phagocytic spreading is the apparent variability in behavior. Although prior to late-stage contraction, spreading curves tend to be sigmoidal, neither the maximum area nor the spreading time appear to be fixed at a universal value. The range in measured mechanical parameters suggests that much of the variability in behavior may be attributed to variability in mechanical properties. In fact, allowing radius,

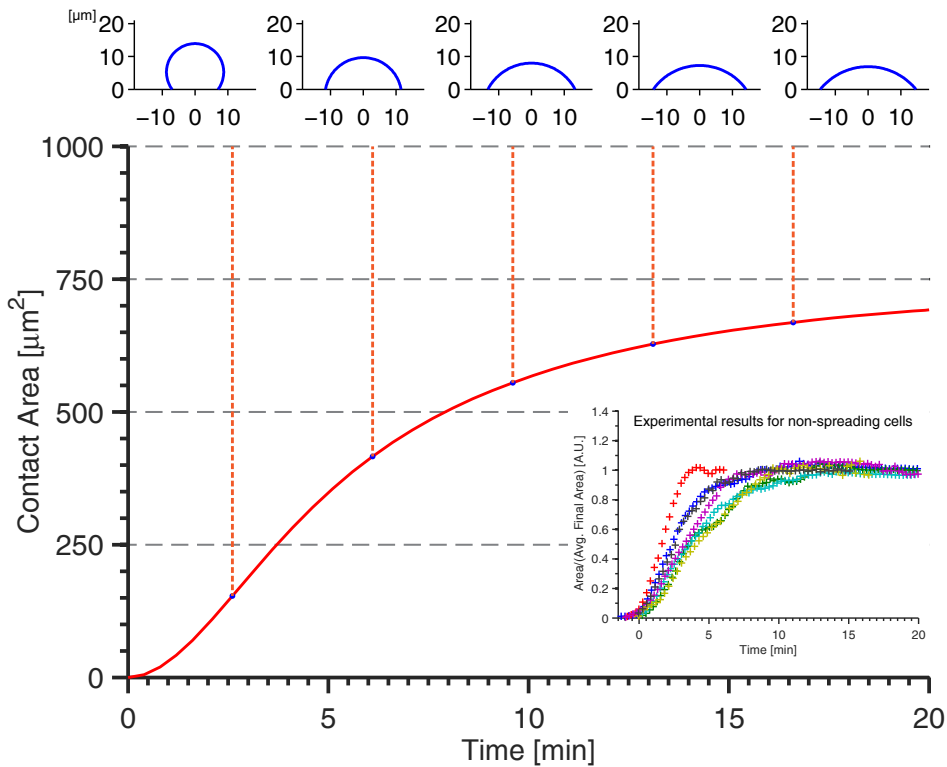


Figure 7.4: Model results for average parameters. Hydrodynamic models was numerically integrated using RK4 with $R_0 = 8.4 \mu\text{m}$, $\gamma_0 = 0.14 \text{ mN/m}$, $\kappa = 0.15 \text{ mN/m}$, $\eta = 0.91 \text{ kPa} \cdot \text{s}$, $W_a = 0.05 \text{ mJ/m}^2$, $f_{\text{protrusion}} = 0.4 \text{ mN/m}$. Computed cell profile is depicted in plots, which correspond to vertical dashed lines. Inset shows normalized spreading curves for 7 cell which did not contract during late-stage FP.

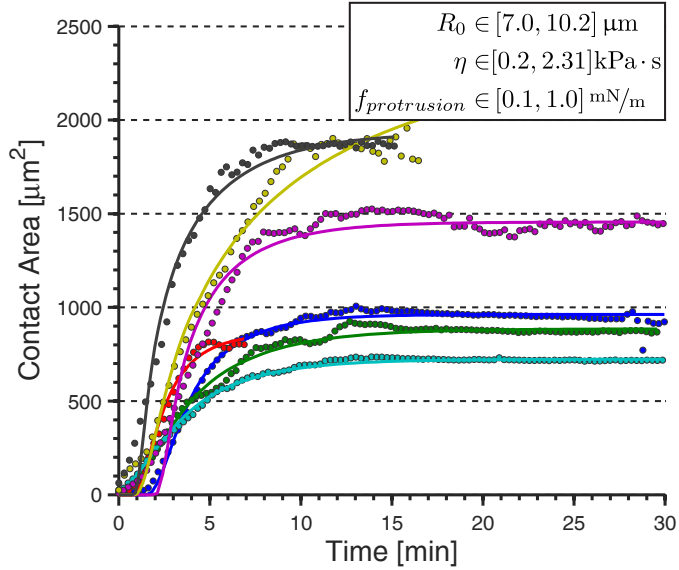


Figure 7.5: Model fit to non-contracting spreading curves. R_0 , η , $f_{protrusion}$ were allowed to range over the values listed. W_a , γ_0 , κ , were pinned at the average values (see table 7.1). Fits were evaluated using MATLAB’s fitting routine.

viscosity, and protrusion force to range between the experimentally measured error limits we can fit a number of our spreading curves remarkably well. The fit of seven such curves are illustrated in Figure 7.5.

7.5.3 Non-spreading cells suggest approximate value of adhesion energy

In addition to offering explanation of the variability observed for spreading cells, the model also predicts significant variability for non-spreading cells. Setting $f_{protrusion} = 0$, we can emulate the behavior of cells which spread passively. Although non-spreading cells do not adhere in completely smooth ways their final contact areas tend to lie in a range between $200-400 \mu\text{m}^2$. Matching the upper and lower bounds associated with the measured range for radius and viscosity, we find that the adhesion energy is approximately $W_a = 0.16 \text{ mJ/m}^2$. By comparison, static contact angle measurements performed by van Oss on primary neutrophils with IgG substrates yielded adhesion energies on the order of 0.2 mJ/m^2 [141].

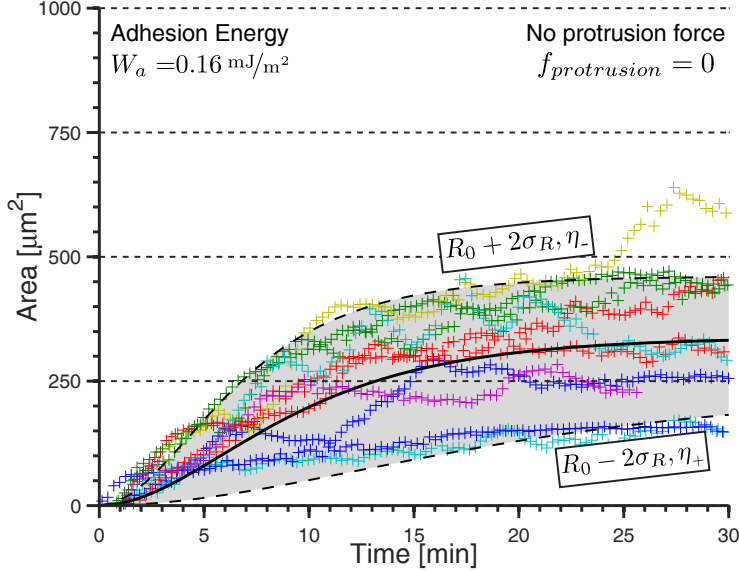


Figure 7.6: Passive spreading. Model results with $f_{protrusion} = 0$. Limits correspond to measured range of R_0 and η . Adhesion energy was chosen to center “non-spreading” results (symbols) in middle of predicted limits. Each color corresponds to a different cell.

7.6 Discussion

7.6.1 Model predicts relationship between cell spreading and mechanical parameters

As stated at the onset of this chapter, one of the main goals in developing this model was to help us build intuition about how a cell’s mechanical properties affect its spreading behavior. To that end, the model makes qualitative predictions about the effect of each of the critical parameters. For instance, the initial radius and protrusion force affect the scale of spreading. Viscosity determines the time-scale of spreading, but not the final contact area. The two components of cortical tension each play separate roles. The resting tension, γ_0 , scales the spreading behavior similar to the cell size. The area dependent tension, κ , sets the roll-off. At low values of κ , the model reflects standard wetting behavior. As κ increases, the plateau becomes more pronounced. These results are summarized in Figure 7.7.

7.6.2 Proposed experimental validation of model predictions

Because the model is based upon measurable cell characteristics some of the numerical predictions illustrated in Figure 7.7 are experimentally verifiable. For instance, exposing cells

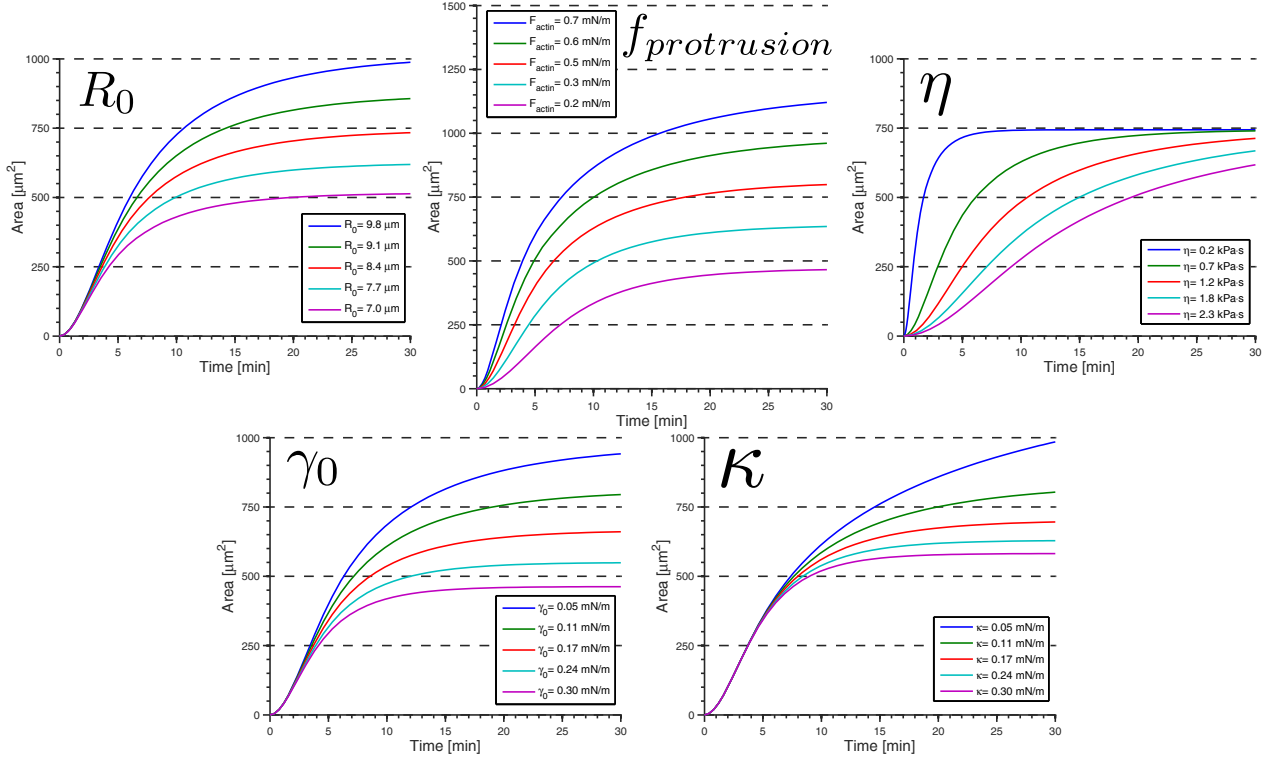


Figure 7.7: Parameter Variation. Each plot corresponds to varying the listed parameter over the range indicated for each color while holding the other parameters fixed at the average values listed in table 7.1. W_a was held at 0.05 mJ/m² for all plots.

to osmotic pressure shocks via hypo and hyper-tonic buffers has been shown to affect late-stage spreading behavior [69, 55, 110]. Using the aspiration technique discussed in Section 7.3.2.1 it is feasible to quantitatively assess the effect of osmotic shock on both resting and elastic tension (γ_0 and κ). Incorporation of extra lipid into the plasma membrane has also been used to study the effect of membrane tension [7]. As a supplement to osmotic pressure experiments, vesicle fusion could also be used to quantitatively assess the role of cortical tension.

A similar approach can be used to determine the role of viscosity. The technique discussed in Section 7.4.3 provides a direct method for measuring effective viscosity of individual cells. Given that hypo and hyper-tonic environments cause cells to swell and shrink (respectively), it is likely that osmotic pressure can also be used to adjust cell viscosity while simultaneously perturbing cortical tension. Additionally, cytoskeletal stabilization drugs such as jasplakinolide (which stabilizes F-actin) and cytochalasin D (which causes F-actin

depolymerization) might also provide a mechanism for quantitatively perturbing cell viscosity. Although, it should be noted that these methods are also likely to affect the protrusion forces generated by the cell [21, 105, 70].

7.6.3 Limitations and possible modifications

Admittedly, the model presented in this chapter is not without limitations. In formulating the model, the cell was assumed to form a spherical cap as it spread. This is a simplification. In reality, symmetrically spreading cells typically resemble fried-eggs, where the bulge in the center corresponds with the nucleus and the edges correspond with the symmetric lamellipodial protrusions. Incorporation of a more realistic geometry would likely require the inclusion of two significant features. First, the cell edge would need to be defined as a free surface (parametrized only by the base radius, volume constraint, and dynamic contact angle). Second, given that similar formulations of wetting droplets show that free-surface solutions approximate spherical caps [125], it is likely that the presence of the nucleus is primarily responsible for the cell's aspherical geometry. Micropipette aspiration experiments have shown that the cell nucleus is significantly stiffer than the surrounding cell body [81]. Consequently, inclusion of the cell nucleus would likely require a hybrid two-phase fluid-fluid or fluid-solid approach.

In formulating the spreading model, the cytoskeletal protrusion force ($f_{protrusion}$) was simply defined as a constant, outward-facing line-force. Realistically, the magnitude of F-actin drive protrusion forces likely depend on a number of factors, including biochemical signals and possibly membrane tension [115, 148, 11, 41]. Additionally, as shown in Chapter 5 and Chapter 6, late-stage contraction is the result of F-actin reorganization and myosin activity. These features are not represented in the model; however, the protrusion force ($f_{protrusion}$) need not be defined simply as a constant. Instead, $f_{protrusion}$ could be redefined to have a functional dependence on other parameters such as the cortical tension, $\gamma(A)$, or additional time-ordered differential equations representing the cell's internal chemical state. Furthermore, given compatible measurements of the contractile force generated during late-stage FP, it would be feasible to adapt the model to predict retraction rates.

CHAPTER VIII

CONCLUSION

8.1 Summary of results

Extensive research has revealed that phagocytosis is regulated by scores of signaling molecules [1]; yet, how these molecular signaling events are coupled to the mechanics of the cell has remained largely unexplained [131]. The biomolecular machinery involved in phagocytosis has been shown to be closely related to the machinery that drives lamellipodial cell migration [132].

Both lamellipodial migration and phagocytic cup formation are known to be dependent on ARP2/3-mediated F-actin polymerization at the leading edge of protrusion [90]. Numerous experimental characterizations and detailed cryo-em imaging have revealed that lamellipodial protrusions are driven by the flow of the F-actin treadmill (see Chapter 2.2.2) operating in a highly-branched, closely-packed, F-actin network (see Figure 2.4). The similarities between phagocytosis and lamellipodial migration have led many to suggest that physical frameworks used to describe migration might also be useful for characterizing phagocytosis [91]. In particular, it has been posited that phagocytic cup formation is driven by the polymerization of F-actin fibers oriented (on average) along the direction of protrusion (see Figure 2.5c). That model (called the lamellipodial spreading model, and reviewed in Chapter 2.3.1) posits a protrusion mechanism functionally identical to the mechanism known to drive lamellipodial protrusion.

The experiments presented in Chapter 4 demonstrate that dynamics of frustrated phagocytic spreading (the planar analog of phagocytic cup formation) are quantitatively similar to dynamics observed for non-phagocytic forms of cell spreading. The model developed in Chapter 7 shows that the dynamics of symmetric cell spreading can be explained by a cell's macroscopic fluid and mechanical properties coupled to a constant, outward directed, protrusion force. Furthermore the model shows that measurements of protrusion forces

generated during lamellipodial extension yield dynamic spreading behaviors consistent with those observed during experiments.

While symmetric FP spreading corresponds to a universal spreading behavior, FP is distinguished from non-phagocytic spreading by a late-stage contraction period. This contraction is consistent with contractile activity observed during the phagosomal closure phase of traditional phagocytosis [134, 57]. Because the lamellipodial model dictates that F-actin filaments be oriented along the surface of a target antigen particle, it does not provide a mechanism by which contractile forces can be generated. This inconsistency has led to the supposition of an alternate model of F-actin termed the contractile belt model [134]. Under the contractile belt model, F-actin is bundled into fibers which run around the perimeter of a closing phagocytic cup (see Figure 2.5b).

Despite its plausibility, the contractile belt has not been verified for traditional phagocytosis; however, the experiments presented in Chapter 5 show that late-stage FP contraction is characterized by the formation of F-actin bundles which run parallel to a cell's retracting perimeter. Furthermore, the presence of F-actin bundles is distinct from the cytoskeletal structure present during early-stage symmetric spreading. During early-stage spreading, F-actin forms a dense network near the perimeter of the cell, consistent with ARP2/3 branched networks known to drive lamellipodia. These results suggest that both the lamellipodial and contractile belt models are involved in driving phagocytic behavior.

In Chapter 6, the myosin inhibitors blebbistatin and ML-7 were used to investigate the role of myosin II in regulating frustrated phagocytic behavior. The experiments demonstrate that not only is late-stage contraction dependent on myosin, but myosin activity appears to be involved in determining cell morphology. Extensive inhibition (via blebbistatin) results in a loss of cell coherence. Under blebbistatin inhibition, macrophages form multiple fronts which spread, unchecked, eventually pulling the cell into multiple fragments. Acknowledging the role of myosin II in driving late-stage contraction and regulating cell shape, I posit a model of phagocytosis which connects the lamellipodial spreading behavior that dominates phagocytic cup formation with the formation of a contractile F-actin belt during late-stage closure. The model is based on the dynamic contraction model (DCM) of cell migration

[130, 3, 153, 114, 118].

Under my proposed dynamic contraction model of phagocytosis, F-actin dissociation enables myosin II motors to engage with initially outward directed F-actin fibers. Myosin filaments, bound to initially crossed F-actin fibers, exert a centered-directed force on the fibers (see Figure 8.1). Due to jamming at the barbed-end of F-actin fibers (near the cell edge), this force results in a torque which causes the fibers to rotate into anti-parallel alignment, forming the contractile belt structure which drives late-stage contraction.

Additionally, the results of the experiments presented in Chapter 6 suggest that the biochemical signal cascade involved in phagocytosis may predispose phagocytes to have higher levels of myosin activity than other cell types. Blocking calcium dependent myosin activity, using ML-7, does not prevent late-stage contraction; however it does appear to bias macrophages to form asymmetric, polarized, lamellipodia (similar to migrating cells). This suggests relative myosin activity levels between cell types may be responsible for dictating whether a cell exhibits a migratory or phagocytosis-like contractile response after it adheres to a ligand coated surface.

8.2 Future work

The protocols presented throughout this thesis facilitate quantitative characterization of phagocytic behavior with a precision unmatched by traditional phagocytosis techniques. These methods also enable high-resolution imaging of biomolecular and structural activity within cells. The techniques developed through this research constitute the groundwork necessary to quantitatively interrogate the mechanisms driving phagocytosis.

This research has shown that phagosomal formation and internalization is driven both by lamellipodia-like F-actin protrusions and construction of a contractile belt. Furthermore, I propose a possible mechanism by which phagocytes reorient lamellipodial F-actin structures into contractile belts. While these findings are significant in their own right, development of a comprehensive model of phagocytosis is far from complete. Rigorous physics-based simulations of the DMC are needed to validate its predictions. A number of published cytoskeletal simulations have focused on replicating lamellipodial migration, but in most

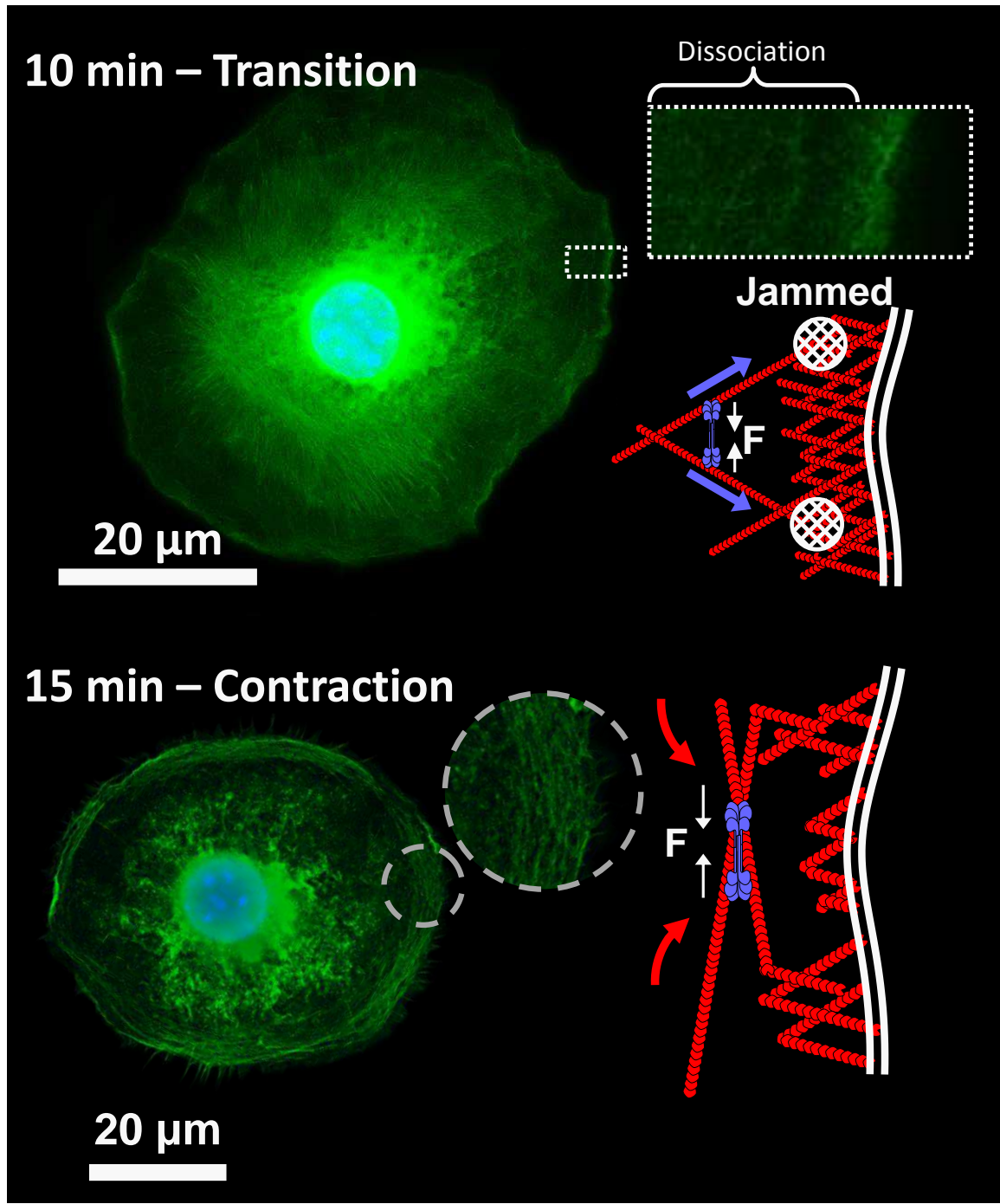


Figure 8.1: Dynamic contraction model of phagocytosis. F-actin dissociation during the transition phase enables myosin II motors to engage with initially outward directed F-actin fibers. Myosin filaments, bound to crossed F-actin fibers, exert force on the fibers. Due to jamming at the barbed-end of F-actin fibers (near the cell edge), force act as a torque, causing fibers to rotate into anti-parallel alignment. Anti-parallel fiber form the contractile belt structure which drives late-stage contraction.

cases downplay or neglect the role of myosin (instead focusing on F-actin polymerization and ARP2/3 induced branching) [94]. In light of the results presented in Chapter 6, DCM simulations parametrized by myosin activity would be immensely useful for determining the mechanisms responsible for cell morphology.

In addition to quantitative modeling, new experiments are also needed to further develop a comprehensive model of phagocytosis. For instance, super-resolution imaging of myosin, and ARP2/3 during phagocytosis are tremendously important for validating the dynamic contraction model of phagocytosis. Additionally, dynamic imaging of F-actin using live-cell SIM or perhaps light scattering techniques [53] could be used to confirm the dynamic branched to bundled transition prescribed by DCM.

Final, the frustrated phagocytosis assays developed over the course of this research are uniquely tailored to answer long-standing questions regarding the spatial organization and localization of biochemical signaling molecules during phagocytosis. Fc-receptor mediated phagocytosis is thought to be a processive process (termed the zipper model), whereby continual stimulation is needed to drive phagocytic cup formation [132]. However, recent experiments have shown that frustrated phagocytic spreading is not necessarily confined to regions of lithographically patterned antibody, suggesting the zipper model may be inaccurate [89]. Experiments capturing the spatial localization of phagocytosis-associated signals such as Syk, PIP₂, PIP₃, Rac, and ROCK, during frustrated phagocytosis on lithographically patterned substrates would provide valuable insight as to how phagocytes integrate Fc-receptor signals.

APPENDIX A

TRACTION FORCE MICROSCOPY TECHNIQUES AND ANALYSIS

A.1 *Polyacrylamide substrate preparation*

The TFM experiments presented in Chapter 5 were conducted using hydrogel elastic substrates. The hydrogel is made of polyacrylamide made by photo-crosslinking solutions of acrylamide and bis-acrylamide. As depicted the schematic in Figure 3.8, the gel is cast in two layers. The base layer consists only of polymerized polyacrylamide while the top layer contains fluorescent tracker particles and if functionalized to stimulate cell adhesion (or in the case of the experiments presented in Chapter 5, induce a phagocytic response).

A.1.1 **Coverslip activation**

The hydrogel surface is cast on top of a glass coverslip which has been treated with 3-(Trimethoxysilyl)propyl methacrylate (MaPTES) to ensure adhesion between the gel and the glass surface. In order to maximize gel thickness while preserving the ability to image TFM substrate using high numerical apertures objectives it is recommended that surfaces be made using either No. 0 or No. 1 coverslips (i.e. less than 0.16 mm thick). The glass surface is treated using the following process.

Clean coverslip

1. Sonicate coverslip in ethanol for 15 minutes
2. Sonicate in DI-H₂O for 15 minutes
3. Sonicate in 1 N NaOH solution for 30 minutes
4. Rinse with DI-H₂O, and dry with N₂

Activate with MaPTES

1. Place cleaned coverslips into glass desiccator with 100 µL of 3-(Trimethoxysilyl)propyl

methacrylate (Sigma: 440159) and 10 μ L of Triethylamine (Sigma: 471283) which acts as a catalyst.

2. Seal desiccator and pump down to approximately -25 inHg
3. Heat desiccator to 90 °C for 40 minutes, then allow to cool for 20 minutes

Coverslips may be stored under vacuum for up to 2 weeks.

A.1.2 Hydrophobic surfaces

Hydrogel substrates are formed using a liquid droplet-sandwich technique as illustrated in Figure A.2. The hydrogels are cast between the MaPTES activated coverslips and a hydrophobic glass surface. The hydrophobic glass surface is made using the following protocol.

1. Clean 35 × 35 mm No. 1.5 coverglass using ethanol and DI-H₂O, then dry with N₂
2. Place slides in desiccator along with 100 μ L Trichloro(1H, 1H, 2H, 2H-perfluorooctyl)silane (Sigma: 448931-10G)
3. Evacuate to -25 inHg
4. Heat to 100 °C for 40 minutes, then let cool for 20 minutes

Hydrophobic slides may be stored in a sealed box at room temperature and pressure indefinitely. Prior to use, rinse and dry to remove dust.

A.1.3 Acrylamide hydrogel preparation

In principle elastic substrates can be made from any transparent elastic rubber. For instance, collagen, gelatin, and PDMS (Polydimethylsiloxane) have all been used in various traction force studies [142, 87, 128]. For single-cell traction force studies polyacrylamide is an ideal substrate because it can be prepared to have a stiffness ranging from 10 – 10⁴ Pa, values compatible with measuring pico-Newton forces generated during cell activities [152, 13]. Polyacrylamide stiffness depends on the relative fraction of acrylamide monomer to bis-acrylamide crosslinker. The dependence of the Young's modulus on monomer:cross-linker ratio has been well characterized [152, 79] (see Figure A.1). A table of polyacrylamide stiffness can also be found in Plotnikov *et al.* [103].

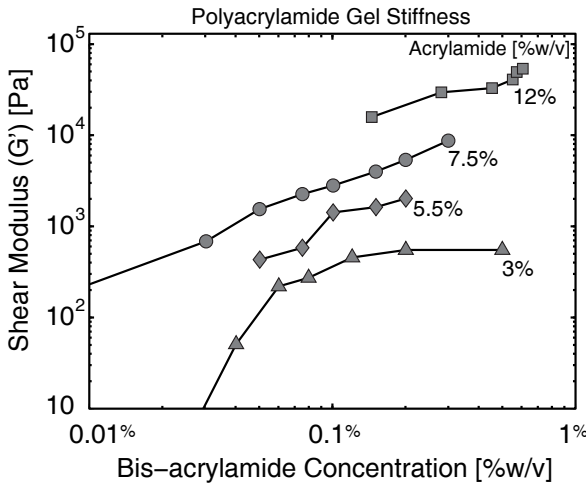


Figure A.1: Polyacrylamide stiffness versus acrylamide:bis-acrylamide ratio. Data originally presented in Yeung *et al.* [152]. Concentrations of acrylamide and bis-acrylamide are in terms of grams/mL of DI-H₂O.

The experiments presented in Chapter 5 were conducted on acrylamide surfaces with an estimated stiffness of 3000 Pa and an estimated Poisson's ratio of 0.3 (as reported in [13]). The gel hydrogel was formulated using the recipe listed in Table A.1. Prior to the hydrogel preparation, stock solutions of acrylamide (Sigma: A3553) and N,N'-Methylenebisacrylamide (Sigma: 66667) were dissolved to concentrations of 30% and 1% (in DI-H₂O), respectively. As depicted in Figure 3.8, elastic substrates consisted of two layers. The top layer included fluorescent tracker particles while the base layer was made-up of only hydrogel. Unlike many published polyacrylamide recipes ([103, 13], polymerization was not initiated using the chemical catalyst TEMED¹. Instead, polymerization was initiated using UV-light and the photo-initiator 2-hydroxy-2-methyl-propiophenone. Elastic substrates were prepared using a two-layer process (see Figure A.2).

Solution preparation

1. Before mixing sample solutions, prepare stock solutions of Acrylamide 30% w/v in H₂O and 1% w/v N,N'-methyl-bis-acrylamide in H₂O.
2. Mix two batches of polymer solution (with and without beads) following recipes

¹Typical polyacrylamide recipes use tetramethylethylenediamine (TEMED) combined with ammonium persulfate.

in Table A.1

3. Vortex gel solution to thoroughly mix
4. Desiccate gel solutions for 20 minutes to remove air bubbles

Base-layer Polymerization

1. Place hydrophobic glass on top of smooth, level, support
2. Gently pipette 30 μL of (bead-free) gel solution onto hydrophobic slide, avoid bubbles
3. Lower MaPTES treated coverslip onto gel solution
4. Expose to 365 nm UV light for 10 minutes
5. Gently submerge sample into water and use tweezer to gently remove coverslip.
Gel should release from hydrophobic surface without tearing
6. Using straight-edge razor trim gel layer to a square approximately 1 cm \times 1 cm
7. Rinse with water
8. Gently dry surface with N_2

Top-layer Polymerization

1. Pipette 10 μL droplette of gel solution with beads onto hydrophobic coverslip
2. Slowly lower droplette onto center of dry polyacrylamide base-layer, droplet should spread symmetrically upon contact

Table A.1: Acrylamide gel recipe. Solution is polymerized using UV photo-polymerization. Final stiffness is approximately 3 kPa and has an approximate Poisson's ratio of 0.3. Values in parenthesis indicate volumes use for solution containing fluorescent tracker particles.

| | % by Volume | Actual Volume |
|--|-------------|---------------------|
| 30% w/v Acrylamide | 5% | 167 μL |
| 1% w/v N,N'-methyl-bis-acrylamide | 0.2% | 200 μL |
| (Top Layer) 200 nm Fluorescent Beads 10% w/v washed 2 \times | (2%) | (20 μL) |
| 2-Hydroxy-2-methyl-propiophenone | 0.2% | 2 μL |

3. Expose to 365 nm UV light for 10 minutes
4. Gently submerge sample into water and use tweezer to gently remove coverslip.
Gel should release from hydrophobic surface without tearing
5. Using straight-edge razor trim excess gel
6. Rinse and store in water until ready to functionalize with protein

A.1.4 Polyacrylamide biofunctionalization

Polyacrylamide hydrogels are functionalized using the UV-activated cross-linking reagent Sulfo-SANPAH. For frustrated phagocytosis experiments, hydrogels are functionalized with bovine serum albumin (BSA) which acts as an antigen layer against which anti-BSA antibodies are reacted to create an immune-stimulating substrate.

BSA functionalization

1. Reconstitute Sulfo-SANPAH (Life Technologies: 22589) at 50 mg/mL in DMSO, aliquot to 40 µL and store at -80 °C until use
2. Rinse polyacrylamide gel surface with water, then shake dry
3. Dilute Sulfo-SANPAH to 2 mg/mL in DI-H₂O
4. Cover gel with Sulfo-SANPAH solution and expose to 365 nm UV light for 3 minutes
5. Wash gel several times in PBS
6. Cover slide in protein solution (1 mg/mL BSA in PBS for FP experiments), incubate 1 hour at room temperature
7. Wash gel several times in PBS

IgG Opsonization After covalently linking BSA to gel surface, substrates can be opsonized with anti-BSA IgG or serum protein

1. Place BSA functionalized coverslip face-down on 100 µL drop of 1 mg/mL anti-BSA serum protein in PBS

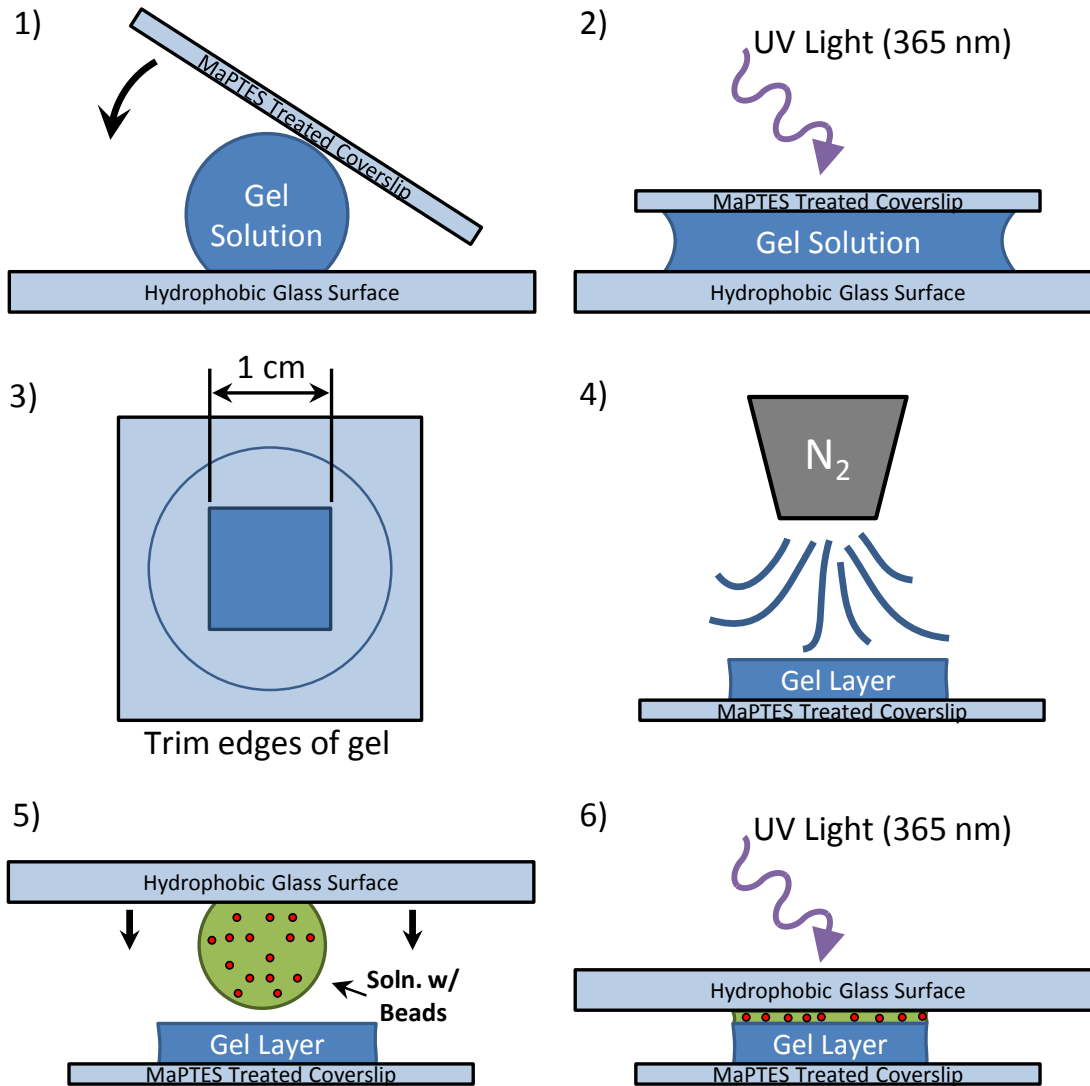


Figure A.2: TFM substrate preparation. 1) Pipette gel solution onto hydrophobic slide, cover with MaPTES activated slide. 2) Expose to UV for 10 minutes. 3) Trim gel to 1 cm square. 4) Gently dry with N_2 stream. 5) Pipette bead-containing gel solution onto hydrophobic slide, lower onto trimmed gel layer. 6) Expose to UV light for 10 minutes.

2. Incubate for 1 hour at room temperature
3. Rinse with PBS
4. Prior to use, incubate with culture media for 30 minutes at 4 °C

A.2 Measurement of stress-induced surface displacement

Live-cell frustrated phagocytosis TFM experiments are performed using a protocol similar to the standard FP protocol described in Chapter 3.1. Interaction between macrophages and the substrate were imaged using a Nikon TE-2000 microscope equipped for both DIC and fluorescent microscopy. Cells were imaged using a Nikon Plan Apo VC 60× 1.20 NA water immersion lens with a working distance of 0.27. The lens included a correction collar which was set to its maximum distance (0.19 mm) in order to maximize the working distance. For long-term imaging at physiological temperatures (37 °C), water is a poor immersion fluid because it evaporates. Instead a calibrated refractive index oil ($n_d = 1.335$) was purchased from Cargille Labs (Cargille Series: AAA). Samples were mounted on the motorized stage using a custom-built sample holder (see Figures A.4, A.3). During the course of experiments, focus was maintained using the Nikon perfect-focus system. Fluorescence microscopy was used to image motion of the tracker beads as cells engaged with the substrate.

Particle displacements were calculated using a customized particle-tracking algorithm based on code developed by Weeks and Crocker [35]. Displacement tracks were interpolated

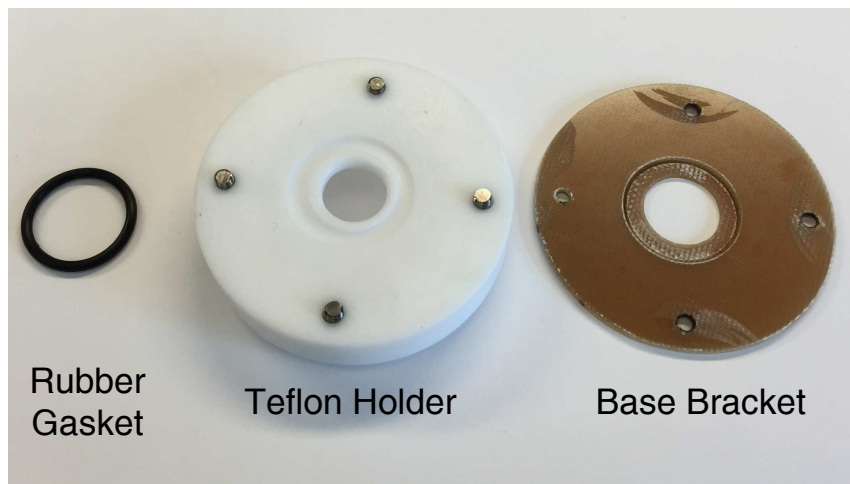


Figure A.3: TFM Sample Holder.

into a regularized grid corresponding to the approximate local- substrate displacement using the standard “scatteredInterpolant” algorithm included with MATLAB. Particle tracking errors were eliminated using filtering algorithm based on the methods presented in Westerweel and Scarano [149].

A.2.1 Calculation of traction stress

The most mathematically intensive challenge of implementing traction force microscopy is inverting the force-displacement relation for the elastic substrate. Calculations are based on the equations of equilibrium is given by the Boussinesq potential as presented in Landau-Lifshitz Theory of Elasticity [83].

The displacement within the elastic substrate caused by a point-force is given by the response-function

$$u_i = G_{ik}(x, y, z)F_k, \quad (\text{A.1})$$

with

$$G = \frac{1+\nu}{2\pi E} \begin{bmatrix} \frac{2(1-\nu)r+z}{r(r+z)} + \frac{[2r(\nu r+z)+z^2]x^2}{r^3(r+z)^2} & \frac{[2r(\nu r+z)+z^2]xy}{r^3(r+z)^2} & \frac{xz}{r^3} - \frac{(1-2\nu)x}{r(r+z)} \\ \frac{[2r(\nu r+z)+z^2]xy}{r^3(r+z)^2} & \frac{2(1-\nu)r+z}{r(r+z)} + \frac{[2r(\nu r+z)+z^2]y^2}{r^3(r+z)^2} & \frac{yz}{r^3} - \frac{(1-2\nu)y}{r(r+z)} \\ \left[\frac{1-2\nu}{r(r+z)} + \frac{z}{r^3} \right] x & \left[\frac{1-2\nu}{r(r+z)} + \frac{z}{r^3} \right] y & \frac{2(1-\nu)}{r} + \frac{z^2}{r^3} \end{bmatrix}. \quad (\text{A.2})$$

On the surface $z = 0$,

$$G = \frac{1+\nu}{\pi E} \cdot \frac{1}{r^3} \begin{bmatrix} (1-\nu)r^2 + \nu x^2 & \nu xy & -(1-2\nu)rx \\ \nu xy & (1-\nu)r^2 + \nu y^2 & -(1-2\nu)rx \\ \frac{1-2\nu}{2}xr & \frac{1-2\nu}{2}yr & (1-\nu)r^2 \end{bmatrix}. \quad (\text{A.3})$$

Assuming no normal forces and ignoring normal displacements

$$G(x, y) = \frac{1+\nu}{\pi E} \cdot \frac{1}{r^3} \begin{bmatrix} (1-\nu(r^2 + \nu x^2) & vxy \\ vxy & (1-\nu(r^2 + \nu y^2) \end{bmatrix}. \quad (\text{A.4})$$

For a distribution of stress applied to the surface

$$u_i(x, y) = \int \int G_{ij}(x - x', y, y') T_j(x', y') dx' dy' = G_{ij} * I_j. \quad (\text{A.5})$$

Taking the Fourier-transform

$$\tilde{u}_i(k_x, k_y) = \mathcal{F}[G_{ij} * T_j] = \tilde{G}_{ij}(k_x, k_y) \cdot \tilde{T}_j(k_x, k_y). \quad (\text{A.6})$$

Consequently the traction force can be solved by inverting the linear equation in Fourier-space and then taking the inverse Fourier transform. The Fourier-space response tensor is

$$\tilde{G} = \frac{2(1+\nu)}{E} \cdot \frac{1}{k^3} \begin{bmatrix} k^2 - \nu k_x^2 & -\nu k_x k_y \\ -\nu k_x k_y & k^2 - \nu k_y^2 \end{bmatrix}. \quad (\text{A.7})$$

If you assume that the displacement field is without noise we can solve for \mathbf{T} by simple inversion

$$\tilde{\mathbf{T}} = \tilde{G}^{-1} \cdot \tilde{\mathbf{u}} \quad (\text{A.8})$$

$$\tilde{G}^{-1} = \frac{E}{2(1+\nu)} \cdot \frac{1}{k(1-\nu^2)} \cdot \begin{bmatrix} k^2 - \nu k_y^2 & \nu k_x k_y \\ \nu k_x k_y & k^2 - \nu k_x^2 \end{bmatrix}. \quad (\text{A.9})$$

A.2.2 Fourier Transform Traction Force Cytometry (FTTC)

Using the relationship defined in eq A.8, the stress-field generated by a cell can be calculated using a Fourier-method termed Fourier Transform Traction Force Cytometry (FTTC) [25]. First, the frame-by-frame 2-D Fourier-transform of the regularized displacement field is calculated. Next, this Fourier-space displacement field is multiplied by the inverse Boussinesq potential calculated in eq A.9, yielding the Fourier-transform of the traction stress. Finally, the real-space traction stress is calculated by taking the inverse Fourier-transforms. The result is a stress-field defined at regular intervals. An example can be seen in Figure 5.2.

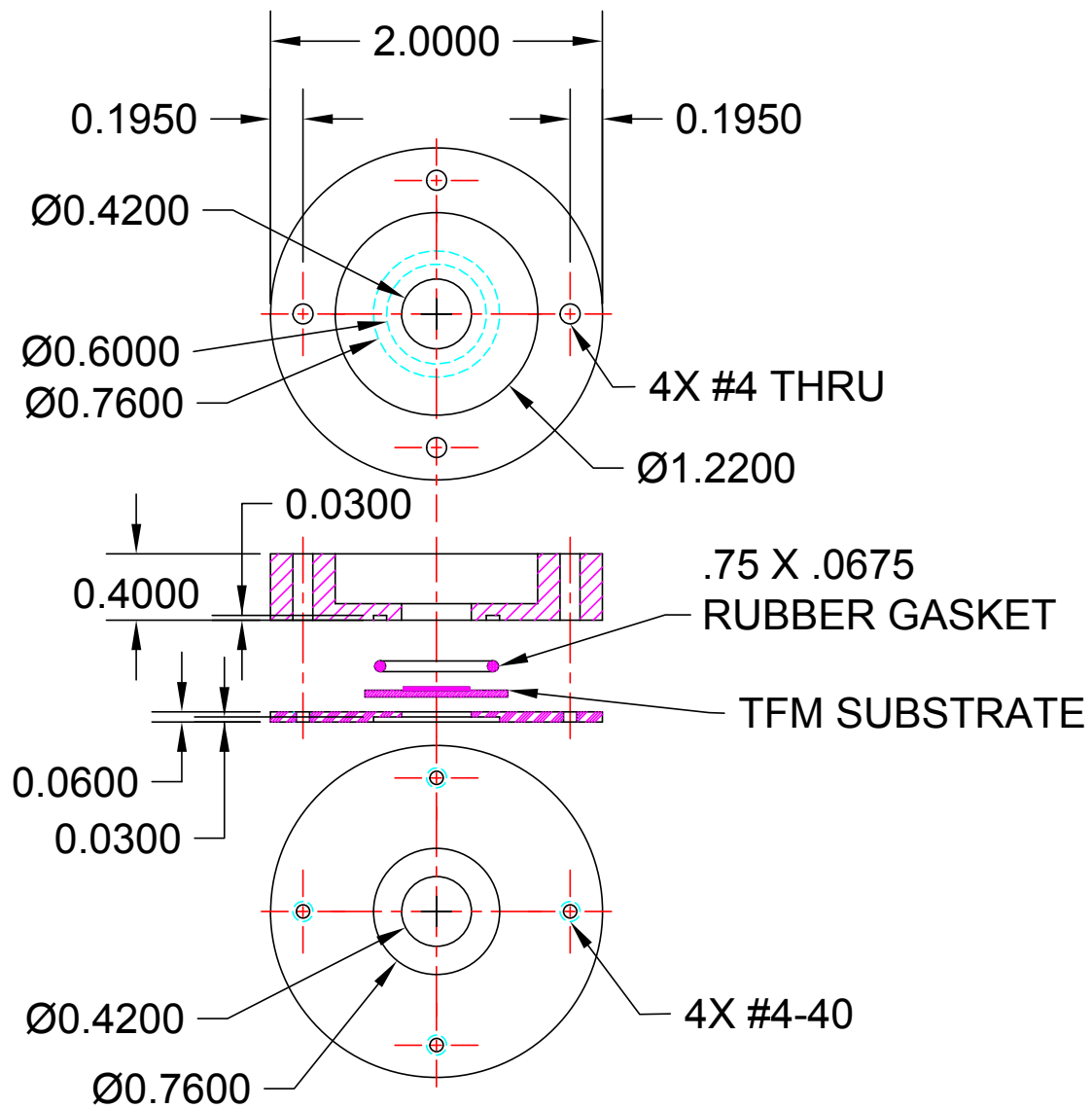


Figure A.4: TFM Sample Holder Schematic. All dimensions are in inches.

APPENDIX B

MEMBRANE TETHER FORCE

The analysis presented here investigates the approximate force required to pull a membrane tether from a simple lipid vesicle. The discussion presented here is largely derived from explanations presented in Phillips *et al.*[101]

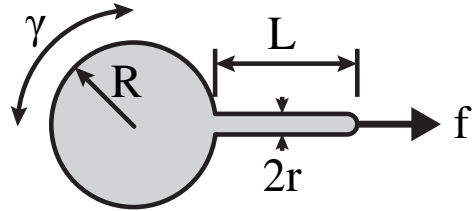


Figure B.1: Membrane tether. Tether force is calculated for a simple spherical vesicle with a tether pulled from its surface at constant force f .

We begin our analysis of membrane tether force by calculating the free energy of a spherical vesicle with a single tether

$$G = G_{bend} + G_{stretch} + G_{pV} + G_{load}. \quad (\text{B.1})$$

The free energy is a combination of four terms: G_{bend} , the energy associated with the lipid bilayer being forced to bend, $G_{stretch}$, energy from stretching the membrane, G_{pV} , the work done by fluid pressure on the membrane, and G_{load} , the work done to pull a tether at constant force. The bending energy for any lipid surface is given by

$$G_{bend} = \frac{K_b}{2} \int da \cdot (\kappa_1(x, y) + \kappa_2(x, y))^2, \quad (\text{B.2})$$

where K_b is a characteristic bending modulus and $\kappa_{1,2}$ are local curvature along the principle axes of bending. For the geometry shown in figure B.1, this integrates to

$$G_{bend} = 12\pi K_b + \pi K_b \frac{L}{r}. \quad (\text{B.3})$$

Energy due to membrane stretching is

$$G_{stretch} = \frac{K_a}{2} \frac{(a - a_0)^2}{a_0}, \quad (\text{B.4})$$

where a is the area, a_0 is a predetermined resting area, and K_a is defined in terms of the membrane tension

$$\gamma = K_a \frac{\Delta a}{a_0}. \quad (\text{B.5})$$

The work done by fluid pressure is

$$G_{pV} = -\Delta p \left(\frac{4}{3} \pi R^3 + r^2 \pi L \right), \quad (\text{B.6})$$

where the variables R , r , L are defined in figure B.1.

The work done by the pulling force is simply

$$G_{load} = -fL. \quad (\text{B.7})$$

Minimizing the free energy with respect to R , r , and L yields

$$\frac{\partial G}{\partial R} = 8\pi\gamma R - 4\pi\Delta p R^2 = 0 \quad (\text{B.8})$$

$$\frac{\partial G}{\partial r} = -\pi K_b \frac{L}{r^2} + 2\pi\gamma L - 2\pi\delta pr L = 0 \quad (\text{B.9})$$

$$\frac{\partial G}{\partial L} = \pi K_b \frac{1}{r} + 2\pi\gamma r - \pi\delta pr^2 - f = 0 \quad (\text{B.10})$$

Eq B.8 reduces to the Young-Laplace equation

$$\delta p = \frac{2\gamma}{R}. \quad (\text{B.11})$$

Combining this with the assumption that $R \gg r$ we use eq B.9 to find

$$r = \sqrt{\frac{K_b}{2\gamma}}. \quad (\text{B.12})$$

Similarly equations B.11, B.12, B.10 combine to yield

$$f = 2\pi\sqrt{2K_b\gamma}. \quad (\text{B.13})$$

APPENDIX C

TABLE OF SIGNALLING PROTEINS

| Name | Abbreviation | Role |
|-------------------------------------|--------------------|--|
| Actin Relate Protein 2 & 3 | ARP2/3 | Binds side of F-actin and creates a nucleation site at 70° angle. Inactive without WASP or WAVE. |
| Cell Division control protein 42 | Cdc42 | Member of rho family, associated with filopodia [34]. activates WASP allowing ARP2/3 to function. |
| Dbl Homology domain | DH | Catalytic component of GEF. This domain binds Rho proteins and enables them to accept fresh GTP. These regions often interact with neighboring PH domain to regulate GEF function [22] |
| Fc γ -Receptor | Fc γ R, FcR | Receptors on the surface of cell which bind IgG and stimulate phagocytosis |
| Formin | Formin | Acts as a nucleation site for actin, also protect actin from capping by CapZ, CapG [156]. |
| Actin (globular or filamentous) | G-actin, F-actin | Globular and filamentous forms of actin. Form the actin cytoskeleton. |
| Guanine nucleotide exchange factors | GEFs | Bind with Rho proteins and promote release of GDP and binding of fresh GTP. This enables Rho to be active [22]. Many Rac-enabling GEFs are triggered by PIP3 (RacGEV Vav, SOS, RacGEF P-Rex1 |
| Immunoglobulin G | IgG | Antibodies which attach to pathogens, stimulate phagocytosis when bound to FcReceptors |
| Lim kinase | LIM | Phosphorylates (deactivates) MLC-phosphatase |
| Myosin Light Chain | MLC | Regulatory control domain of myosin, myosin is active when MLC is phosphorylated |
| Myosin Light Chain Phosphatase | MLC phosphatase | Dephosphorylates (deactivates) MLC, disabling myosin motor |
| Myosin Light Chain Kinase | MLCK | Phosphorylates MLC, activates myosin. Must be bound to Ca ²⁺ /calmodulin to be active [54] |
| Myosin* | Myo* | Motor proteins which exert forces on actin |

| Name | Abbreviation | Role |
|--------------------------------------|----------------------|---|
| P21-activated kinase | PAK | A type of Rho GTPase. Involved in cytoskeleton reorganization. Activates MLC |
| Pleckstrin homology domain | PH | A protein domain that occurs in many phagocytosis related enzymes, PH domains can bind to various forms of PIP |
| Phosphoinositide-(3,4,5)triphosphate | PI(3,4,5)P3, PIP3 | A product of PIP2, signals late-stage phagocytosis. Activates Rho proteins via GEFs |
| Phosphoinositide-(4,5)bispophosphate | PI(4,5)P2, PIP2 | A product of PIP. Signals enzymes which regulate actin polymerization, including ARP2/3 |
| PI 3-kinase | PI3K | Adds a phosphate group to the 3' location of PI(4,5)P2 |
| Phosphoinositide-phosphate | PIP | Signalling lipid located on cytosolic side of plasma membrane, signals various, Phosphorylated into PIP2 |
| Rac | Rac | Member of Rho family, associated with lamellipodia [34]. Activates Arp2/3 using WAVE (instead of WASP) |
| RacGEF vav | RacGEF vav | Contains a PH domain and DH domain. When PH domain binds with PIP2 it blocks the DH from attaching to Rac. When PH domain binds to PIP3 it allows DH to bind Rac [22] |
| Myosin* | Myo* | Motor proteins which exert forces on actin |

| Name | Abbreviation | Role |
|--|--------------|--|
| Rho family GTPase | Rho | <p>Includes Cdc42, Rac1, RhoA.</p> <p>Act as molecular switches.</p> <p>In active (GTP-bound state) these proteins bind to many autoinhibited proteins and activate them.</p> <p>Conformational change of Rho is powered by hydrolysis of GTP to GDP. GAP proteins help Rho hydrolyze GTP (i.e. become deactivated) while GEF proteins help Rho drop GDP and bind fresh GTP (i.e. become active)[24]</p> |
| Rho member A | RhoA | Member of Rho family, associated with stress fibers [34]. Activates Formins which act as F-actin nucleation sites |
| Rho-associated kinase | ROCK | Phosphorylates MLC and LIM, becomes active when it binds with RhoA. Has a PH domain. |
| Src Homology 2 domain | SH2 | Protein domain common in many kinases involved in phagocytosis. SH2 binds preferentially to phosphorylated tyrosine (like in ITAM domain of active FcR) |
| Wiskott-Aldrich syndrome protein | WASP | Upon binding with PIP2, it is able to activate ARP2/3. |
| WASP-family verprolin-homologous protein | WAVE | Similar to WASP, activates Arp2/3. |

REFERENCES

- [1] ADEREM, A. and UNDERHILL, D. M., "Mechanisms of phagocytosis in macrophages.", *Annu. Rev. Immunol.*, vol. 17, pp. 593–623, 1999.
- [2] ALONSO-LATORRE, B., DEL ÁLAMO, J. C., MEILI, R., FIRTEL, R. A., and LASHERAS, J. C., "An Oscillatory Contractile Pole-Force Component Dominates the Traction Forces Exerted by Migrating Amoeboid Cells.", *Cell. Mol. Bioeng.*, vol. 4, no. 4, pp. 603–615, 2011.
- [3] ANDERSON, K. I. and CROSS, R., "Contact dynamics during keratocyte motility," *Curr. Biol.*, vol. 10, pp. 253–260, 2000.
- [4] ARAKI, N., JOHNSON, M. T., and SWANSON, J. A., "A role for phosphoinositide 3-kinase in the completion of macropinocytosis and phagocytosis by macrophages.", *J. Cell Biol.*, vol. 135, no. 5, pp. 1249–60, 1996.
- [5] ARAKI, N., HATAE, T., FURUKAWA, A., and SWANSON, J. A., "Phosphoinositide-3-kinase-independent contractile activities associated with Fc gamma-receptor-mediated phagocytosis and macropinocytosis in macrophages," *J. Cell Sci.*, vol. 116, no. 2, pp. 247–257, 2002.
- [6] ARATYN-SCHAUS, Y., OAKES, P. W., STRICKER, J., WINTER, S. P., and GARDEL, M. L., "Preparation of compliant matrices for quantifying cellular contraction.", *J. Vis. Exp.*, pp. 3–9, 2010.
- [7] AROUSH, D. R.-B., YEHUDAI-RESHEFF, S., and KEREN, K., *Electrofusion of giant unilamellar vesicles to cells*, vol. 125. Elsevier Ltd, 2015.
- [8] ASLAN, J. E. and McCARTY, O. J. T., "Rho GTPases in platelet function.", *J. Thromb. Haemost.*, vol. 11, pp. 35–46, 2013.
- [9] BAMBURG, J. R., McGOUGH, A., and ONO, S., "Putting a new twist on actin: ADF/cofilins modulate actin dynamics," *Trends Cell Biol.*, vol. 9, no. September, pp. 364–370, 1999.
- [10] BARKALOW, K. L., FALET, H., ITALIANO, J. E., VAN VUGT, A., CARPENTER, C. L., SCHREIBER, A. D., and HARTWIG, J. H., "Role for phosphoinositide 3-kinase in Fc gamma RIIA-induced platelet shape change.", *Am. J. Physiol. Cell Physiol.*, vol. 285, no. 4, pp. C797–805, 2003.
- [11] BATCHELDER, E. L., HOLLOPETER, G., CAMPILLO, C., MEZANGES, X., JORGENSEN, E. M., NASSOY, P., SENS, P., and PLASTINO, J., "Membrane tension regulates motility by controlling lamellipodium organization.", *Proc. Natl. Acad. Sci. U. S. A.*, vol. 108, pp. 11429–34, July 2011.
- [12] BEEMILLER, P., ZHANG, Y., MOHAN, S., LEVINSOHN, E., GAETA, I., HOPPE, A. D., and SWANSON, J. A., "A Cdc42 activation cycle coordinated by PI 3-kinase during Fc receptor-mediated phagocytosis," *Mol. Biol. Cell*, vol. 21, pp. 470–480, 2010.

- [13] BENINGO, K. A., LO, C.-M., and WANG, Y.-L., “Flexible polyacrylamide substrata for the analysis of mechanical interactions at cell-substratum adhesions,” *Methods Cell Biol.*, vol. 69, pp. 325–39, 2002.
- [14] BILLINGTON, N., WANG, A., MAO, J., ADELSTEIN, R. S., and SELLERS, J. R., “Characterization of three full-length human nonmuscle myosin II paralogs,” *J. Biol. Chem.*, vol. 288, no. 46, pp. 33398–33410, 2013.
- [15] BLAKE, T. D., “The physics of moving wetting lines.,” *J. Colloid Interface Sci.*, vol. 299, pp. 1–13, July 2006.
- [16] BOTELHO, R., SCOTT, C., and GRINSTEIN, S., “Phosphoinositide Involvement in Phagocytosis and Phagosome Maturation,” in *Phosphoinositides Subcell. Target. Enzym. Act.*, pp. 1–30, Springer-Verlag Berlin Heidelberg, 2004.
- [17] BRESNICK, A. R., “Molecular mechanisms of nonmuscle myosin-II regulation,” *Curr. Opin. Cell Biol.*, vol. 11, pp. 26–33, 1999.
- [18] BRETSCHNEIDER, T., DIEZ, S., ANDERSON, K., HEUSER, J., CLARKE, M., MÜLLER-TAUBENBERGER, A., KÖHLER, J., and GERISCH, G., “Dynamic Actin Patterns and Arp2/3 Assembly at the Substrate-Attached Surface of Motile Cells,” *Curr. Biol.*, vol. 14, pp. 1–10, Jan. 2004.
- [19] BROCHARD-WYART, F. and DE GENNES, P., “Dynamics of partial wetting,” *Adv. Colloid Interface Sci.*, vol. 39, pp. 1–11, Apr. 1992.
- [20] BROCHARD-WYART, F. and DE GENNES, P.-G., “Unbinding of adhesive vesicles,” *Comptes Rendus Phys.*, vol. 4, pp. 281–287, Mar. 2003.
- [21] BUBB, M. R., SPECTOR, I., BEYER, B. B., and FOSEN, K. M., “Effects of Jasplakinolide on the Kinetics of Actin Polymerization. An Explanation for Certain In Vivo Observations.” *J. Biol. Chem.*, vol. 275, pp. 5163–5170, Feb. 2000.
- [22] BUCHSBAUM, R. J., “Rho activation at a glance.,” *J. Cell Sci.*, vol. 120, pp. 1149–1152, 2007.
- [23] BURNETTE, D. T., MANLEY, S., SENGUPTA, P., SOUGRAT, R., DAVIDSON, M. W., KACHAR, B., and LIPPINCOTT-SCHWARTZ, J., “A role for actin arcs in the leading-edge advance of migrating cells.,” *Nat. Cell Biol.*, vol. 13, no. 4, pp. 371–381, 2011.
- [24] BUSTELO, X. R., SAUZEAU, V., and BERENJENO, I. M., “GTP-binding proteins of the Rho/Rac family: Regulation, effectors and functions in vivo,” 2007.
- [25] BUTLER, J. P., TOLIĆ-NØ RRELYKKE, I. M., FABRY, B., and FREDBERG, J. J., “Traction fields, moments, and strain energy that cells exert on their surroundings.,” *Am. J. Physiol. Cell Physiol.*, vol. 282, pp. C595–605, Mar. 2002.
- [26] CAI, Y., BIAIS, N., GIANNONE, G., TANASE, M., JIANG, G., HOFMAN, J. M., WIGGINS, C. H., SILBERZAN, P., BUGUIN, A., LADOUX, B., and SHEETZ, M. P., “Nonmuscle myosin IIA-dependent force inhibits cell spreading and drives F-actin flow.,” *Biophys. J.*, vol. 91, pp. 3907–20, Nov. 2006.

- [27] CAI, Y., ROSSIER, O., GAUTHIER, N. C., BIAIS, N., FARDIN, M.-A., ZHANG, X., MILLER, L. W., LADOUX, B., CORNISH, V. W., and SHEETZ, M. P., “Cytoskeletal coherence requires myosin-IIA contractility,” *J. Cell Sci.*, vol. 123, pp. 413–423, 2010.
- [28] CARLIER, M. F., PANTALONI, D., and KORN, E. D., “Evidence for an ATP cap at the ends of actin filaments and its regulation of the F-actin steady state,” *J. Biol. Chem.*, vol. 259, pp. 9983–6, Aug. 1984.
- [29] CHAMARAUX, F., ALI, O., KELLER, S., BRUCKERT, F., and FOURCADE, B., “Physical model for membrane protrusions during spreading,” *Phys. Biol.*, vol. 5, p. 036009, Jan. 2008.
- [30] CHAMARAUX, F., FACHE, S., BRUCKERT, F., and FOURCADE, B., “Kinetics of Cell Spreading,” *Phys. Rev. Lett.*, vol. 94, p. 158102, Apr. 2005.
- [31] CHAMPION, J. A. and MITRAGOTRI, S., “Role of target geometry in phagocytosis,” *Proc. Natl. Acad. Sci. U. S. A.*, vol. 103, pp. 4930–4, Mar. 2006.
- [32] CLARKE, M., ENGEL, U., GIORGIONE, J., MÜLLER-TAUBENBERGER, A., PRASSLER, J., VELTMAN, D., and GERISCH, G., “Curvature recognition and force generation in phagocytosis,” *BMC Biol.*, vol. 8, no. 1, p. 154, 2010.
- [33] COX, R. G., “The dynamics of the spreading of liquids on a solid surface. Part 1. Viscous flow,” *J. Fluid Mech.*, vol. 168, pp. 169–194, Apr. 1986.
- [34] COZIER, G. E., CARLTON, J., BOUYOCEF, D., and CULLEN, P. J., “Membrane Targeting by Pleckstrin Homology Domains,” in *Phosphoinositides Subcell. Target. Enzym. Act.*, ch. 3, pp. 49–88, Springer-Verlag Berlin Heidelberg, 2004.
- [35] CROCKER, J. C. and GRIER, D. G., “Methods of Digital Video Microscopy for Colloidal Studies,” *J. Colloid Interface Sci.*, vol. 179, pp. 298–310, Apr. 1996.
- [36] CUVELIER, D., THÉRY, M., CHU, Y.-S., DUFOUR, S., THIÉRY, J.-P., BORNENS, M., NASSOY, P., and MAHADEVAN, L., “The universal dynamics of cell spreading,” *Curr. Biol.*, vol. 17, pp. 694–9, Apr. 2007.
- [37] DANUSER, G. and WATERMAN-STORER, C. M., “Quantitative fluorescent speckle microscopy of cytoskeleton dynamics,” *Annu. Rev. Biophys. Biomol. Struct.*, vol. 35, pp. 361–87, Jan. 2006.
- [38] DEL ALAMO, J. C., MEILI, R., ALONSO-LATORRE, B., RODRÍGUEZ-RODRÍGUEZ, J., ALISEDA, A., FIRTEL, R. A., and LASHERAS, J. C., “Spatio-temporal analysis of eukaryotic cell motility by improved force cytometry,” *Proc. Natl. Acad. Sci. U. S. A.*, vol. 104, pp. 13343–8, Aug. 2007.
- [39] DEL ALAMO, J. C., MEILI, R., ALONSO-LATORRE, B., RODRÍGUEZ-RODRÍGUEZ, J., ALISEDA, A., FIRTEL, R. A., and LASHERAS, J. C., “Spatio-temporal analysis of eukaryotic cell motility by improved force cytometry,” *Proc. Natl. Acad. Sci. U. S. A.*, vol. 104, pp. 13343–8, Aug. 2007.
- [40] DIAKONOVA, M., BOKOCH, G., and SWANSON, J. A., “Dynamics of cytoskeletal proteins during Fcgamma receptor-mediated phagocytosis in macrophages,” *Mol. Biol. Cell*, vol. 13, pp. 402–11, Feb. 2002.

- [41] DIZ-MUÑOZ, A., FLETCHER, D. A., and WEINER, O. D., “Use the force: membrane tension as an organizer of cell shape and motility,” *Trends Cell Biol.*, vol. 23, pp. 47–53, Feb. 2013.
- [42] DÖBEREINER, H.-G., DUBIN-THALER, B., GIANNONE, G., XENIAS, H., and SHEETZ, M. P., “Dynamic Phase Transitions in Cell Spreading,” *Phys. Rev. Lett.*, vol. 93, p. 108105, Sept. 2004.
- [43] DÖBEREINER, H. G., DUBIN-THALER, B. J., HOFMAN, J. M., XENIAS, H. S., SIMS, T. N., GIANNONE, G., DUSTIN, M. L., WIGGINS, C. H., and SHEETZ, M. P., “Lateral membrane waves constitute a universal dynamic pattern of motile cells,” *Phys. Rev. Lett.*, vol. 97, pp. 10–13, 2006.
- [44] DUBIN-THALER, B. J., GIANNONE, G., DÖBEREINER, H.-G., and SHEETZ, M. P., “Nanometer analysis of cell spreading on matrix-coated surfaces reveals two distinct cell states and STEPs,” *Biophys. J.*, vol. 86, pp. 1794–806, Mar. 2004.
- [45] DUBIN-THALER, B. J., HOFMAN, J. M., CAI, Y., XENIAS, H., SPIELMAN, I., SHNEIDMAN, A. V., DAVID, L. A., DÖBEREINER, H.-G., WIGGINS, C. H., and SHEETZ, M. P., “Quantification of cell edge velocities and traction forces reveals distinct motility modules during cell spreading,” *PLoS One*, vol. 3, no. 11, p. e3735, 2008.
- [46] ERNST, J. D., “Bacterial inhibition of phagocytosis,” *Cell. Microbiol.*, vol. 2, pp. 379–386, Oct. 2000.
- [47] FÄLLMAN, M., ANDERSSON, K., HÅ KANSSON, S., MAGNUSSON, K. E., STENDAHL, O., and WOLF-WATZ, H., “Yersinia pseudotuberculosis inhibits Fc receptor-mediated phagocytosis in J774 cells,” *Infect. Immun.*, vol. 63, pp. 3117–24, Aug. 1995.
- [48] FARDIN, M. A., ROSSIER, O. M., RANGAMANI, P., AVIGAN, P. D., GAUTHIER, N. C., VONNEGUT, W., MATHUR, A., HONE, J., IYENGAR, R., and SHEETZ, M. P., “Cell spreading as a hydrodynamic process,” *Soft Matter*, vol. 6, no. 19, p. 4788, 2010.
- [49] FLEISCHER, C. and PAYNE, C. K., “Secondary Structure of Corona Proteins Determines the Cell Surface Receptors Used by Nanoparticles,” *J. Phys. Chem. B*, 2014.
- [50] FRESHNEY, R. I., *Culture of Animal Cells: A Manual of Basic Techniques*. Hoboken, New Jersey: John Wiley and Sons, Inc., 5th ed., 2005.
- [51] FRISCH, T. and THOUFINE, O., “Predicting the kinetics of cell spreading,” *J. Biomech.*, vol. 35, pp. 1137–41, Aug. 2002.
- [52] FUKAI, J., ZHAO, Z., POULIKAKOS, D., MEGARIDIS, C. M., and MIYATAKE, O., “Modeling of the deformation of a liquid droplet impinging upon a flat surface,” *Phys. Fluids A Fluid Dyn.*, vol. 5, no. 11, p. 2588, 1993.
- [53] FURUKAWA, R. and FECHHEIMER, M., “Characterization of Cross-Linked Actin Filament Gels and Bundles Using Birefringence and Polarized Light Scattering,” in *Dicystostelium discoideum Protoc.*, ch. 24, pp. 407–421, Humana Press Inc., 1st ed., 2006.
- [54] GALLAGHER, P. J., HERRING, B. P., and STULL, J. T., “Myosin light chain kinases,” *J. Muscle Res. Cell Motil.*, vol. 18, pp. 1–16, 1997.

- [55] GAUTHIER, N. C., FARDIN, M. A., ROCA-CUSACHS, P., and SHEETZ, M. P., "Temporary increase in plasma membrane tension coordinates the activation of exocytosis and contraction during cell spreading.," *Proc. Natl. Acad. Sci. U. S. A.*, vol. 108, pp. 14467–72, Aug. 2011.
- [56] GAUTHIER, N. C., MASTERS, T. A., and SHEETZ, M. P., "Mechanical feedback between membrane tension and dynamics," *Trends Cell Biol.*, vol. 22, no. 10, pp. 527–535, 2012.
- [57] GERISCH, G., ECKE, M., SCHROTH-DIEZ, B., GERWIG, S., ENGEL, U., MADDERA, L., and CLARKE, M., "Self-organizing actin waves as planar phagocytic cup structures.," *Cell Adh. Migr.*, vol. 3, no. 4, pp. 373–82, 2009.
- [58] GIANNONE, G., DUBIN-THALER, B. J., DÖBEREINER, H.-G., KIEFFER, N., BRESNICK, A. R., and SHEETZ, M. P., "Periodic lamellipodial contractions correlate with rearward actin waves.," *Cell*, vol. 116, pp. 431–43, Feb. 2004.
- [59] GITIK, M., REICHERT, F., and ROTSHENKER, S., "Cytoskeleton plays a dual role of activation and inhibition in myelin and zymosan phagocytosis by microglia.," *FASEB J.*, vol. 24, pp. 2211–2221, 2010.
- [60] GITTES, F., "Flexural rigidity of microtubules and actin filaments measured from thermal fluctuations in shape," *J. Cell Biol.*, vol. 120, pp. 923–934, Feb. 1993.
- [61] GREENBERG, S., EL KHOURY, J., DI VIRGILIO, F., KAPLAN, E. M., and SILVERSTEIN, S. C., "Ca(2+)-independent F-actin assembly and disassembly during Fc receptor-mediated phagocytosis in mouse macrophages.," *J. Cell Biol.*, vol. 113, pp. 757–67, May 1991.
- [62] GREENBERG, S., "Modular components of phagocytosis.," *J. Leukoc. Biol.*, vol. 66, pp. 712–7, Nov. 1999.
- [63] GUSTAFSSON, M. G. L., "Surpassing the lateral resolution limit by a factor of two using structured illumination microscopy. SHORT COMMUNICATION," *J. Microsc.*, vol. 198, pp. 82–87, May 2000.
- [64] HAMID, N., GUSTAVSSON, A., ANDERSSON, K., McGEE, K., PERSSON, C., RUDD, C. E., and FÄLLMAN, M., "YopH dephosphorylates Cas and Fyn-binding protein in macrophages.," *Microb. Pathog.*, vol. 27, pp. 231–42, Oct. 1999.
- [65] HEINTZMANN, R. and CREMER, C., "Laterally Modulated Excitation Microscopy: Improvement of resolution by using a diffraction grating," *Proc. SPIE*, vol. 3568, pp. 185–196, 1999.
- [66] HERANT, M., HEINRICH, V., and DEMBO, M., "Mechanics of neutrophil phagocytosis: behavior of the cortical tension.," *J. Cell Sci.*, vol. 118, pp. 1789–97, May 2005.
- [67] HILPELA, P., VARTIAINEN, M., and LAPPALAINEN, P., "Regulation of the Actin Cytoskeleton by PI(4,5)P₂ and PI(3,4,5)P₃," in *Phosphoinositides Subcell. Target. Enzym. Act.*, pp. 117–164, Springer-Verlag Berlin Heidelberg, 2004.
- [68] HOCHMUTH, R. M., "Micropipette aspiration of living cells.," *J. Biomech.*, vol. 33, pp. 15–22, Jan. 2000.

- [69] HOUK, A. R., JILKINE, A., MEJEAN, C. O., BOLTYANSKIY, R., DUFRESNE, E. R., ANGENENT, S. B., ALTSCHULER, S. J., WU, L. F., and WEINER, O. D., "Membrane tension maintains cell polarity by confining signals to the leading edge during neutrophil migration," *Cell*, vol. 148, pp. 175–88, Jan. 2012.
- [70] JAUMOUILLÉ, V. and GRINSTEIN, S., "Receptor mobility, the cytoskeleton, and particle binding during phagocytosis," *Curr. Opin. Cell Biol.*, vol. 23, pp. 22–9, Feb. 2011.
- [71] JURADO, C., HASERICK, J. R., and LEE, J., "Slipping or gripping? Fluorescent speckle microscopy in fish keratocytes reveals two different mechanisms for generating a retrograde flow of actin," *Mol. Biol. Cell*, vol. 16, pp. 507–18, Mar. 2005.
- [72] KATSUMI, A., MILANINI, J., KIOSSES, W. B., DEL POZO, M. A., KAUNAS, R., CHIEN, S., HAHN, K. M., and SCHWARTZ, M. A., "Effects of cell tension on the small GTPase Rac," *J. Cell Biol.*, vol. 158, pp. 153–64, July 2002.
- [73] KEELY, P. J., WESTWICK, J. K., WHITEHEAD, I. P., DER, C. J., and PARISE, L. V., "Cdc42 and Rac1 induce integrin-mediated cell motility and invasiveness through PI(3)K," *Nature*, vol. 390, no. December, pp. 632–636, 1997.
- [74] KELLEY, S. J., THOMAS, R., and DUNHAM, P. B., "Candidate inhibitor of the volume-sensitive kinase regulating K-Cl cotransport: The myosin light chain kinase inhibitor ML-7," *J. Membr. Biol.*, vol. 178, pp. 31–41, 2000.
- [75] KEREN, K., PINCUS, Z., ALLEN, G. M., BARNHART, E. L., MARRIOTT, G., MOGILNER, A., and THERIOT, J. A., "Mechanism of shape determination in motile cells," *Nature*, vol. 453, pp. 475–80, May 2008.
- [76] KIMURA, K., ITO, M., AMANO, M., CHIHARA, K., FUKATA, Y., NAKAFUKU, M., YAMAMORI, B., FENG, J., NAKANO, T., OKAWA, K., IWAMATSU, A., and KAIBUCHI, K., "Regulation of myosin phosphatase by Rho and Rho-associated kinase (Rho-kinase)," *Science*, vol. 273, no. 5272, pp. 245–248, 1996.
- [77] KORN, E., CARLIER, M., and PANTALONI, D., "Actin polymerization and ATP hydrolysis," *Science (80-.)*, vol. 238, pp. 638–644, Oct. 1987.
- [78] KOVÁCS, M., TÓTH, J., HETÉNYI, C., MÁLNÁSI-CSIZMADIA, A., and SELLER, J. R., "Mechanism of blebbistatin inhibition of myosin II," *J. Biol. Chem.*, vol. 279, no. 34, pp. 35557–35563, 2004.
- [79] KULICKE, W., KNIEWSKE, R., and KLEIN, J., "Preparation, characterization, solution properties and rheological behaviour of polyacrylamide," *Prog. Polym. Sci.*, vol. 8, pp. 373–468, Jan. 1982.
- [80] LAI, F. P. L., SZCZODRAK, M., BLOCK, J., FAIX, J., BREITSPRECHER, D., MANNHERZ, H. G., STRADAL, T. E. B., DUNN, G. A., SMALL, J. V., and ROTTER, K., "Arp2/3 complex interactions and actin network turnover in lamellipodia," *EMBO J.*, vol. 27, pp. 982–92, Apr. 2008.
- [81] LAM, J., HERANT, M., DEMBO, M., and HEINRICH, V., "Baseline mechanical characterization of J774 macrophages," *Biophys. J.*, vol. 96, pp. 248–54, Jan. 2009.

- [82] LAM HUI, K., WANG, C., GROOMAN, B., WAYT, J., and UPADHYAYA, A., “Membrane dynamics correlate with formation of signaling clusters during cell spreading.,” *Biophys. J.*, vol. 102, pp. 1524–33, Apr. 2012.
- [83] LANDAU, L. D. and LIFSHITZ, E. M., “Equilibrium of an elastic medium bounded by a plane,” in *Theory Elast.*, ch. 8, pp. 26–30, New York, NY: Addison-Wesley Publishing Company, Inc., 2nd ed., 1959.
- [84] LE CLAINCHE, C. and CARLIER, M.-F., “Regulation of actin assembly associated with protrusion and adhesion in cell migration.,” *Physiol. Rev.*, vol. 88, pp. 489–513, 2008.
- [85] LIMOZIN, L. and SENGUPTA, K., “Quantitative reflection interference contrast microscopy (RICM) in soft matter and cell adhesion.,” *Chemphyschem*, vol. 10, pp. 2752–68, Nov. 2009.
- [86] LOCK, J. G., WEHRLE-HALLER, B., and STRÖMBBLAD, S., “Cell-matrix adhesion complexes: master control machinery of cell migration.,” *Semin. Cancer Biol.*, vol. 18, pp. 65–76, Feb. 2008.
- [87] LOMBARDI, M. L., KNECHT, D. A., DEMBO, M., and LEE, J., “Traction force microscopy in Dictyostelium reveals distinct roles for myosin II motor and actin-crosslinking activity in polarized cell movement.,” *J. Cell Sci.*, vol. 120, pp. 1624–1634, 2007.
- [88] MACHACEK, M. and DANUSER, G., “Morphodynamic profiling of protrusion phenotypes.,” *Biophys. J.*, vol. 90, pp. 1439–52, Feb. 2006.
- [89] MASTERS, T. A., PONTES, B., VIASNOFF, V., LI, Y., and GAUTHIER, N. C., “Plasma membrane tension orchestrates membrane trafficking, cytoskeletal remodeling, and biochemical signaling during phagocytosis.,” *Proc. Natl. Acad. Sci. U. S. A.*, vol. 110, pp. 11875–80, July 2013.
- [90] MAY, R. C., CARON, E., HALL, A., and MACHESKY, L. M., “Involvement of the Arp2/3 complex in phagocytosis mediated by FcgammaR or CR3.,” *Nat. Cell Biol.*, vol. 2, pp. 246–8, Apr. 2000.
- [91] MAY, R. C. and MACHESKY, L. M., “Phagocytosis and the actin cytoskeleton.,” *J. Cell Sci.*, vol. 114, pp. 1061–77, Mar. 2001.
- [92] MICHL, J., PIECZONKA, M. M., UNKELESS, J. C., BELL, G. I., and SILVERSTEIN, S. C., “Fc receptor modulation in mononuclear phagocytes maintained on immobilized immune complexes occurs by diffusion of the receptor molecule,” *J. Exp. Med.*, vol. 157, pp. 2121–2139, June 1983.
- [93] MITCHELL, I. M., “The flexible, extensible and efficient toolbox of level set methods,” *J. Sci. Comput.*, vol. 35, pp. 300–329, 2008.
- [94] MOGILNER, A., “Mathematics of cell motility: have we got its number?,” *J. Math. Biol.*, vol. 58, pp. 105–34, Jan. 2009.
- [95] MOGILNER, A. and ZHU, J., “Cell polarity: tension quenches the rear.,” *Curr. Biol.*, vol. 22, pp. R48–51, Jan. 2012.

- [96] MURRELL, M. and GARDEL, M. L., “Actomyosin sliding is attenuated in contractile biomimetic cortices,” *Mol. Biol. Cell*, vol. 25, pp. 1845–53, June 2014.
- [97] NGUYEN, D. H. D., CATLING, A. D., WEBB, D. J., SANKOVIC, M., WALKER, L. A., SOMLYO, A. V., WEBER, M. J., and GONIAS, S. L., “Myosin light chain kinase functions downstream of Ras/ERK to promote migration of urokinase-type plasminogen activator-stimulated cells in an integrin-selective manner,” *J. Cell Biol.*, vol. 146, no. 1, pp. 149–164, 1999.
- [98] OLAZABAL, I. M., CARON, E., MAY, R. C., SCHILLING, K., KNECHT, D. A., and MACHESKY, L. M., “Rho-kinase and myosin-II control phagocytic cup formation during CR, but not FcgammaR, phagocytosis,” *Curr. Biol.*, vol. 12, no. 02, pp. 1413–1418, 2002.
- [99] OSHER, S. and FEDKIW, R., *Level Set Methods and Dynamic Implicit Surfaces*. New York, NY: Springer New York, 2003.
- [100] OSTAP, E. M., “2,3-Butanedione monoxime (BDM) as a myosin inhibitor.,” *J. Muscle Res. Cell Motil.*, vol. 23, pp. 305–8, Jan. 2002.
- [101] PHILLIPS, R., KONDEV, J., and THERIOT, J., “Biological Membranes: Life in Two Dimensions,” in *Phys. Biol. Cell* (MORALES, M., ed.), ch. 11, pp. 428–431, New York, NY: Garland Science, Taylor and Francis Group, LLC, 2009.
- [102] PIERRES, A., EYMERIC, P., BALOCHE, E., TOUCHARD, D., BENOLIEL, A.-M., and BONGRAND, P., “Cell membrane alignment along adhesive surfaces: contribution of active and passive cell processes.,” *Biophys. J.*, vol. 84, pp. 2058–70, Mar. 2003.
- [103] PLOTNIKOV, S. V., SABASS, B., SCHWARZ, U. S., and WATERMAN, C. M., *High-resolution traction force microscopy.*, vol. 123. Elsevier Inc., 1 ed., Jan. 2014.
- [104] POGLITSCH, C. L. and THOMPSON, N. L., “Interaction of antibodies with Fc receptors in substrate-supported planar membranes measured by total internal reflection fluorescence microscopy.,” *Biochemistry*, vol. 29, pp. 248–54, Jan. 1990.
- [105] PONTI, A., MACHACEK, M., GUPTON, S. L., WATERMAN-STORER, C. M., and DANUSER, G., “Two distinct actin networks drive the protrusion of migrating cells.,” *Science*, vol. 305, pp. 1782–1786, Sept. 2004.
- [106] POPESCU, M. N., OSHANIN, G., DIETRICH, S., and A M CAZABAT, “Precursor films in wetting phenomena,” *J. Phys. Condens. Matter*, vol. 24, p. 243102, 2012.
- [107] PRASS, M., JACOBSON, K., MOGILNER, A., and RADMACHER, M., “Direct measurement of the lamellipodial protrusive force in a migrating cell.,” *J. Cell Biol.*, vol. 174, pp. 767–72, Sept. 2006.
- [108] RAEDER, E. M., MANSFIELD, P. J., HINKOVSKA-GALCHEVA, V., SHAYMAN, J. A., and BOXER, L. A., “Syk activation initiates downstream signaling events during human polymorphonuclear leukocyte phagocytosis.,” *J. Immunol.*, vol. 163, pp. 6785–93, Dec. 1999.
- [109] RALPH, P. and NAKOINZ, I., “Phagocytosis and cytosis by a macrophage tumour and its cloned cell line.,” *Nature*, vol. 257, pp. 393–394, 1975.

- [110] RAUCHER, D. and SHEETZ, M. P., “Cell spreading and lamellipodial extension rate is regulated by membrane tension.,” *J. Cell Biol.*, vol. 148, pp. 127–36, Jan. 2000.
- [111] RIENTO, K. and RIDLEY, A. J., “Rocks: multifunctional kinases in cell behaviour.,” *Nat. Rev. Mol. Cell Biol.*, vol. 4, no. June, pp. 446–456, 2003.
- [112] ROSALES, C., “Fc receptor and integrin signaling in phagocytes,” *Signal Transduct.*, vol. 7, pp. 386–401, Dec. 2007.
- [113] ROUGERIE, P., MISKOLCI, V., and COX, D., “Generation of membrane structures during phagocytosis and chemotaxis of macrophages: Role and regulation of the actin cytoskeleton,” *Immunol. Rev.*, vol. 256, pp. 222–239, 2013.
- [114] RUBINSTEIN, B., JACOBSON, K., and MOGILNER, A., “Multiscale Two-Dimensional Modeling of a Motile Simple-Shaped Cell,” *Multiscale Model. Simul.*, vol. 3, no. 2, pp. 413–439, 2005.
- [115] RYAN, G. L., PETROCCIA, H. M., WATANABE, N., and VAVYLONIS, D., “Excitable actin dynamics in lamellipodial protrusion and retraction,” *Biophys. J.*, vol. 102, no. 7, pp. 1493–1502, 2012.
- [116] SABASS, B., GARDEL, M. L., WATERMAN, C. M., and SCHWARZ, U. S., “High resolution traction force microscopy based on experimental and computational advances.,” *Biophys. J.*, vol. 94, pp. 207–20, Jan. 2008.
- [117] SAITO, M., ISHIKAWA, T., MATSUSHIMA, S., NAKA, M., and HIDAKA, H., “Selective inhibition of catalytic activity of smooth muscle myosin light chain kinase.,” *J. Biol. Chem.*, vol. 262, no. 16, pp. 7796–7801, 1987.
- [118] SCHAUB, S., BOHNET, S., LAURENT, V. M., MEISTER, J.-J., and VERKHOVSKY, A. B., “Comparative maps of motion and assembly of filamentous actin and myosin II in migrating cells.,” *Mol. Biol. Cell*, vol. 18, no. October, pp. 3723–3732, 2007.
- [119] SCHMID, F., “Biological Macromolecules: UV-visible Spectrophotometry,” 2001.
- [120] SCHNECKENBURGER, H., SAILER, R., HENDINGER, A., GSCHWEND, M. H., BAUER, M., and STRAUSS, W. S. L., “Phagocytosis: studies by optical tweezers and time-resolved microspectrofluorometry,” in *Proc. SPIE 3568, Opt. Biopsies Microsc. Tech. III*, vol. 3568, pp. 148–153, Jan. 1999.
- [121] SCHWARZ, U. S. and SAFRAN, S. A., “Elastic interactions of cells.,” *Phys. Rev. Lett.*, vol. 88, p. 048102, 2002.
- [122] SELLERS, J., “Myosins,” in *Encycl. life Sci.*, John Wiley & Sons, Ltd., 2006.
- [123] SENGUPTA, K., ARANDA-ESPINOZA, H., SMITH, L., JANMEY, P., and HAMMER, D., “Spreading of neutrophils: from activation to migration.,” *Biophys. J.*, vol. 91, pp. 4638–48, Dec. 2006.
- [124] SETHIAN, J. A., *Level Set Methods and Fast Marching Methods*. New York, NY: Cambridge University Press, 2nd ed., 1999.
- [125] SHIKHMURZAEV, Y. D., “Spreading of drops on solid surfaces in a quasi-static regime,” *Phys. Fluids*, vol. 9, no. 2, p. 266, 1997.

- [126] SHROFF, S. A., FIENUP, J. R., and WILLIAMS, D. R., “OTF compensation in structured illumination superresolution images,” *Unconv. Imaging IV, Ed. by Jean J. Dolne, Thomas J. Karr, Victor L. Gamiz, Proc. SPIE Vol. 7094*, vol. 7094, pp. 709402–709402–11, 2008.
- [127] STRAIGHT, A. F., CHEUNG, A., LIMOUZE, J., CHEN, I., WESTWOOD, N. J., SELLERS, J. R., and MITCHISON, T. J., “Dissecting temporal and spatial control of cytokinesis with a myosin II Inhibitor.,” *Science*, vol. 299, pp. 1743–7, Mar. 2003.
- [128] STYLE, R. W., HYLAND, C., BOLTYANSKIY, R., WETTLAUFER, J. S., and DUFRESNE, E. R., “Surface tension and contact with soft elastic solids.,” *Nat. Commun.*, vol. 4, p. 2728, Jan. 2013.
- [129] SUND, S. E., SWANSON, J. A., and AXELROD, D., “Cell membrane orientation visualized by polarized total internal reflection fluorescence.,” *Biophys. J.*, vol. 77, pp. 2266–83, Oct. 1999.
- [130] SVITKINA, T. M., VERKHOVSKY, A. B., MCQUADE, K. M., and BORISY, G. G., “Analysis of the Actin-Myosin II System in Fish Epidermal Keratocytes: Mechanism of Cell Body Translocation,” *J. Cell Biol.*, vol. 139, pp. 397–415, Oct. 1997.
- [131] SWANSON, J. A., “Shaping cups into phagosomes and macropinosomes.,” *Nat. Rev. Mol. Cell Biol.*, vol. 9, pp. 639–49, Aug. 2008.
- [132] SWANSON, J. A. and BAER, S. C., “Phagocytosis by zippers and triggers,” *Trends Cell Biol.*, vol. 5, pp. 89–93, Mar. 1995.
- [133] SWANSON, J. A. and HOPPE, A. D., “The coordination of signaling during Fc receptor-mediated phagocytosis.,” *J. Leukoc. Biol.*, vol. 76, pp. 1093–103, Dec. 2004.
- [134] SWANSON, J. A., JOHNSON, M. T., BENINGO, K., POST, P., MOOSEKER, M., and ARAKI, N., “A contractile activity that closes phagosomes in macrophages.,” *J. Cell Sci.*, vol. 112, pp. 307–16, Feb. 1999.
- [135] TAKEMURA, R., STENBERG, P. E., BAITON, D. F., and WERB, Z., “Rapid redistribution of clathrin onto macrophage plasma membranes in response to Fc receptor-ligand interaction during frustrated phagocytosis.,” *J. Cell Biol.*, vol. 102, pp. 55–69, Jan. 1986.
- [136] TANIMOTO, H. and SANO, M., “A simple force-motion relation for migrating cells revealed by multipole analysis of traction stress,” *Biophys. J.*, vol. 106, no. 1, pp. 16–25, 2014.
- [137] TOTSUKAWA, G., WU, Y., SASAKI, Y., HARTSHORNE, D. J., YAMAKITA, Y., YAMASHIRO, S., and MATSUMURA, F., “Distinct roles of MLCK and ROCK in the regulation of membrane protrusions and focal adhesion dynamics during cell migration of fibroblasts,” *J. Cell Biol.*, vol. 164, pp. 427–439, 2004.
- [138] TRAN-SON-TAY, R., NEEDHAM, D., YEUNG, A., and HOCHMUTH, R. M., “Time-dependent recovery of passive neutrophils after large deformation.,” *Biophys. J.*, vol. 60, pp. 856–66, Oct. 1991.

- [139] USUI, S. and AMIDROR, I., "Digital low-pass differentiation for biological signal processing.," *IEEE Trans. Biomed. Eng.*, vol. 29, no. 10, pp. 686–693, 1982.
- [140] VAN KEYMEULEN, A., WONG, K., KNIGHT, Z. A., GOVAERTS, C., HAHN, K. M., SHOKAT, K. M., and BOURNE, H. R., "To stabilize neutrophil polarity, PIP3 and Cdc42 augment RhoA activity at the back as well as signals at the front," *J. Cell Biol.*, vol. 174, no. 3, pp. 437–445, 2006.
- [141] VAN OSS, C. J., "Phagocytosis as a Surface Phenomenon," *Annu. Rev. Microbiol.*, vol. 32, pp. 19–39, 1978.
- [142] VELEGOL, D. and LANNI, F., "Cell traction forces on soft biomaterials. I. Microrheology of type I collagen gels.," *Biophys. J.*, vol. 81, pp. 1786–92, Sept. 2001.
- [143] VICENTE-MANZANARES, M., MA, X., ADELSTEIN, R. S., and HORWITZ, A. R., "Non-muscle myosin II takes centre stage in cell adhesion and migration.," *Nat. Rev. Mol. Cell Biol.*, vol. 10, pp. 778–790, 2009.
- [144] VIELKIND, U. and SWIERENGA, S. H., "A simple fixation procedure for immunofluorescent detection of different cytoskeletal components within the same cell.," *Histochemistry*, vol. 91, pp. 81–8, Jan. 1989.
- [145] VITTE, J., BENOLIEL, A. M., PIERRES, A., and BONGRAND, P., "Is there a predictable relationship between surface physical-chemical properties and cell behaviour at the interface?," *Eur. Cell Mater.*, vol. 7, pp. 52–63; discussion 63, June 2004.
- [146] WAKATSUKI, T., WYSOLMERSKI, R. B., and ELSON, E. L., "Mechanics of cell spreading: role of myosin II.," *J. Cell Sci.*, vol. 116, pp. 1617–1625, 2003.
- [147] WELCH, M. D. and MULLINS, R. D., "Cellular control of actin nucleation.," *Annu. Rev. Cell Dev. Biol.*, vol. 18, pp. 247–88, Jan. 2002.
- [148] WELF, E. S., AHMED, S., JOHNSON, H. E., MELVIN, A. T., and HAUGH, J. M., "Migrating fibroblasts reorient directionality: By a metastable, PI3K-dependent mechanism," *J. Cell Biol.*, vol. 197, no. 1, pp. 105–114, 2012.
- [149] WESTERWEEL, J. and SCARANO, F., "Universal outlier detection for PIV data," *Exp. Fluids*, vol. 39, pp. 1096–1100, Aug. 2005.
- [150] WRIGHT, S. D. and SILVERSTEIN, S. C., "Phagocytosing macrophages exclude proteins from the zones of contact with opsonized targets," *Nature*, vol. 309, pp. 359–361, May 1984.
- [151] YANO, H., NAKANISHI, S., KIMURA, K., HANAI, N., SAITO, Y., FUKUI, Y., NOMONURA, Y., and MATSUDA, Y., "Inhibition of histamine secretion by wortmannin through the blockade of phosphatidylinositol 3-kinase in RBL-2H3 cells," *J. Biol. Chem.*, vol. 268, pp. 25846–25856, 1993.
- [152] YEUNG, T., GEORGES, P. C., FLANAGAN, L. A., MARG, B., ORTIZ, M., FUNAKI, M., ZAHIR, N., MING, W., WEAVER, V., and JANMEY, P. A., "Effects of substrate stiffness on cell morphology, cytoskeletal structure, and adhesion.," *Cell Motil. Cytoskeleton*, vol. 60, pp. 24–34, Jan. 2005.

- [153] ZAMIR, E. and GEIGER, B., “Molecular complexity and dynamics of cell-matrix adhesions.” *J. Cell Sci.*, vol. 114, pp. 3583–3590, 2001.
- [154] ZAR, J. H., “Simple Linear Correlation,” in *Biostat. Anal.* (RYU, T., ed.), ch. 19, p. 378, Upper Saddle River, NJ: Prentice-Hall, Inc., 4th ed., 1999.
- [155] ZHANGA, Y., HOPPE, A. D., and SWANSON, J. A., “Coordination of Fc receptor signaling regulates cellular commitment to phagocytosis,” *Proc. Natl. Acad. Sci. U. S. A.*, vol. 107, no. 45, pp. 19332–19337, 2010.
- [156] ZIGMOND, S. H., “Formin-induced nucleation of actin filaments,” *Curr. Opin. Cell Biol.*, vol. 16, pp. 99–105, 2004.

VITA

Daniel Tibor Kovari was born in Chicago, IL. He grew-up in Elgin, IL and graduated from Bartlett High School in 2004. He received his Bachelor of Science in Engineering Physics from the University of Illinois, Urbana-Champaign in May 2008. In the fall of 2008 he move to Atlanta, GA where he began working on his Ph.D. in Physics under the advisement of Dr. Jennifer Curtis. He defended his dissertation in March 2015.